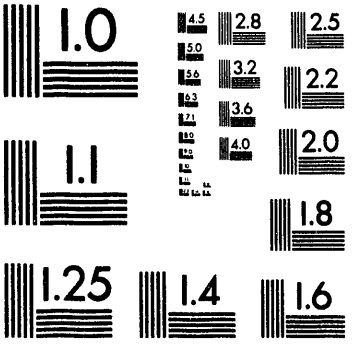
1.0
1.1
1.25
1.4
1.6
1.8
2.0
2.2
2.5
2.8
3.2
3.6
4.0
4.5
5.0
5.6
6.3
7.1
8.0
9.0

1 of 3

LBL-34251
UC-401

Unimolecular Photodissociation Dynamics of Ketene (CH_2CO): the Singlet/Triplet Branching Ratio and Experimental Observation of the Vibrational Level Thresholds of the Transition-State

Sang Kyu Kim
Ph.D. Thesis

Department of Chemistry
University of California

and

Chemical Sciences Division
Lawrence Berkeley Laboratory
University of California
Berkeley, CA 94720

May 1993

This work was supported by the Director, Office of Energy Research, Office of Basic Energy Sciences, Chemical Sciences Division of the U. S. Department of Energy under Contract No. DE-AC03-76SF00098.

TABLE OF CONTENTS

LIST OF TABLES

LIST OF FIGURES

ACKNOWLEDGEMENTS

The first thanks are owed to my research adviser, Professor C. Bradley Moore, for his guidance, support, and patience during my graduate work at Berkeley. Without Brad's guidance, support (both in science and life), and patience (specially when I had a difficult time), this work would not have been possible. His attitude for science and life has always inspired me.

Thanks go to my research coworkers in the laboratory. Dr. Ned Lovejoy was my principal coworker. He is a really good scientist, and I appreciate his significant contribution to this work. Charles Pibel, Q.-K. Zheng, and Young Choi helped me to get started the "real" experiment. They devoted their time to get me started and get the data for the qualifying examination.

I also would like to thank all of past and present group members. Ramón gave his valuable sample whenever I asked. Jeff often pointed out my mistakes or misbehavior (?) in the lab. Hak-Hyun, Young, Horst, Akio, and Han have been good lunch partners. I thank Andy Kung, Horst, and Dean Guyer for helping me test the infrared machine, OPO. Jackie and Heather helped me to solve many complicated personal problems. I appreciate their kindness and support during my graduate student life. I also wish the best luck for Harry, Elizabeth, Jason, Michael, Rich, Ashfaq, and Sean.

Biggest thanks go to my wife, Seungsun. I deeply appreciate love and support of Seungsun during my graduate work at Berkeley. She has endured many financial and emotional difficulties, and allowed me to focus my attention to research. Without her self-sacrificing love and support for past five years, any single piece of this work would not have been possible. I also would like to share this small accomplishment with our wonderful baby, Daniel Daehyun Kim.

Finally, I would like to thank my mother for her self-sacrificing love and support. She has dedicated her whole life to raise and educate children. I appreciate her unfailing love and support. I would like to dedicate my thesis to my father who passed away 14 years ago. Great thanks are owed to my parents-in-law. I appreciate their ever present love and support. I am also grateful to my grandmother, brother, sister, brothers-in-law, and sisters-in-law for their continual encouragement, love, and support.

Abstract

Unimolecular Photodissociation Dynamics of Ketene (CH_2CO): the Singlet/Triplet Branching Ratio and Experimental Observation of the Vibrational Level Thresholds of the Transition-State

by

Sang Kyu Kim

Doctor of Philosophy in Chemistry

University of California at Berkeley

Professor C. Bradley Moore, Chair

The rotational distributions of CO products from the dissociation of ketene at photolysis energies 10 cm^{-1} below, 56, 110, 200, 325, 425, 1107, 1435, 1720, and 2500 cm^{-1} above the singlet threshold (30 116.2 cm^{-1}), are measured in a supersonic free jet of ketene. The CO(v"=0) rotational distributions at 56, 110, 200, 325, and 425 cm^{-1} are bimodal. The peaks at low J's, which are due to CO from the singlet channel, show that the product rotational distribution of CO product from ketene dissociation on the singlet surface is well described by phase space theory (PST). For CO(v"=0) rotational distributions at higher excess energies (1107, 1435, 1720, and 2500 cm^{-1}), the singlet and triplet contributions are not clearly resolved, and the

singlet/triplet branching ratios are estimated by assuming that PST accurately predicts the CO rotational distribution from the singlet channel and that the distribution from the triplet channel changes little from that at 10 cm^{-1} below the singlet threshold. The singlet yield shows a rapid increase in the low excess energy region (0 - 300 cm^{-1}), and a slower increase above. The singlet and triplet rate constants are derived from the directly measured total rate constants using the singlet yields. The triplet rate constant increases monotonically with increasing photolysis energy through the singlet threshold region. The singlet rate constant is accurately established in the threshold region and found to increase much less rapidly than predicted by phase space theory. At 2500 cm^{-1} excess energy, the CO(v"=1) rotational distribution is obtained, and the ratio of CO(v"=1) to CO(v"=0) products for the singlet channel is measured to be 0.045 ± 0.017. This ratio is close to the variational RRKM calculation, 0.038, and the separate statistical ensembles (SSE) prediction, 0.041, but much greater than the PST prediction, 0.016.

Rate constants for the dissociation of ketene (CH_2CO) and deuterated ketene (CD_2CO) have been measured at the threshold for the production of the $CH(D)_2$ ($^3B_1$) and CO ($^1\Sigma^+$). The rate constant increases in a stepwise manner with increasing energy, consistent with the long-standing premise that the

rate of a unimolecular reaction is controlled by flux through quantized transition-state thresholds. Sharp steps in rate constants observed in the reaction threshold region give accurate values for reaction barriers relative to products, 1281 ± 15 cm^{-1} for CH_2CO and 1071 ± 40 cm^{-1} for CD_2CO dissociation. The CO rotational distributions from the dissociation of ketene are determined by the impulsive energy and the vibrational structure of the molecule at its transition state. Sharp peaks observed in photofragment excitation (PHOFEX) spectra probing CO (v=0,J=2) product are identified with the C-C-O bending mode of the transition state. RRKM calculations are carried out for two limiting cases for the dynamics of K-mixing in highly vibrationally excited reactant states. The steplike structures in rate constants are quantitatively well reproduced by the RRKM calculations, while the detailed fine structures in measured rate constants could not be explained by the conventional RRKM theory. The RRKM fits to experimental results give the low vibrational frequencies of ketene at transition state. Densities of vibrational states of the reactant are found to be 1.4-1.7 or 1.8-2.1 times higher than predicted by Whitten-Rabinovitch approximation in the 28,200-28,700 cm^{-1} energy range for CH_2CO or CD_2CO, respectively.

Part I

Determination of the Singlet/Triplet Branching Ratio in the Photodissociation of Ketene

I. INTRODUCTION

Unimolecular dissociations have long been of great interest because of their fundamental significance for understanding chemical bond-breaking dynamics and reaction rates, as well as for their practical importance in many chemical processes. Theoretical models for describing these reactions for ground electronic states have been subjects of controversy for many years. This is especially so for reactions without barriers to recombination of product fragments. Several models have been proposed including the Prior[1], phase space theory (PST)[2,3], statistical adiabatic channel model (SACM)[4], SACM-PST[5], and separate statistical ensembles (SSE)[6], the classic Rice-Ramsberger-Kassel-Marcus (RRKM) theory[7,8], as well as recent modifications thereof.[9]

The combined application of laser and molecular beam methods makes it possible to study unimolecular reactions with the initial state of the reactant fully defined and the final quantum states of the products fully resolved. Such experiments can provide significant qualitative understanding of the dynamics of unimolecular processes as well as discriminating quantitative tests of alternative dynamical theories.

The photodissociation of ketene has been studied for decades because of the importance of methylene as a model for singlet-triplet interactions and because of the recently

resolved controversy over the size of the singlet-triplet energy gap.[10] Ketene also provides a good test case for unimolecular reaction models. Ketene is exited in the UV using a transition whose oscillator strength is derived from electronic excitation to S_1. Internal conversion to S_0 and intersystem crossing to T_1 provide coupling to those two potential energy surfaces from which dissociation occurs. The T_1 triplet state correlates to $^3CH_2(^3B_1)$ + CO products 3147 ± 5 cm^{-1} below the $^1CH_2(^1A_1)$ + CO products which correlate with the ground singlet state. The ketene triplet state has a barrier to dissociation which is less than 1330 cm^{-1} above the products.[11,12] The singlet state has no energy barrier above its asymptote.[13,14]

The PST model, which is based on the assumption that every product quantum state allowed by the conservation laws is equally likely to be populated, has been successful in predicting the product rotational state distribution for a system which dissociates without a barrier, but unsuccessful in predicting the vibrational state distributions and the rate constants.[13-16] Recently, the variational RRKM theory for unimolecular dissociation processes involving a highly flexible transition state has been developed and applied to the dissociation of ketene by Klippenstein and Marcus, and the energy and angular momentum resolved rate constants for ketene dissociation on the singlet surface have been calculated.[17] In variational RRKM theory, the transition

state moves in along the reaction coordinate and tightens as energy increases. Direct rate constant measurements for ketene dissociation have been made by Potter and coworkers using picosecond laser spectroscopy.[18] Theory and experiment are in good agreement. However, this comparison has been made assuming that the singlet yield increases very rapidly with increasing excess energy above the singlet threshold. In order to test the theoretical calculation more quantitatively, measurement of the singlet/triplet branching ratio as a function of the photolysis energy is necessary.

There has been an indirect measurement of the singlet/triplet branching ratio through the photofragment excitation(PHOFEX) studies in the singlet threshold region.[13,14] In the PHOFEX spectrum, the yield of one particular product quantum state is measured as the photolysis energy is scanned. All of the PHOFEX spectra probing $^1CH_2$ quantum states show a rise from threshold as the probed channels open, and then a decline at high photolysis energies as many additional singlet methylene states become energetically accessible and can compete with the specific rotational state being probed. PHOFEX spectra are reproduced very well by phase space theory(PST) for the singlet state by using the triplet rate constant as a parameter in the fitting. The triplet rate was assumed to be constant over the scan range of one PHOFEX curve and the singlet/triplet branching ratio obtained as a function of the photolysis

energy in the singlet threshold region.[13,14,19] However, the uncertainties of these indirectly measured branching ratios are quite large, the assumptions open to question and the data restricted to low excess energy above the singlet threshold. In this work, the singlet/triplet branching ratio is measured from CO rotational distributions at several photolysis energies above the singlet threshold.

On the singlet surface, which has no energy barrier, the product state distribution is expected to be in some sense "statistical", since there are no strong forces favoring any particular motions of the products. On the other hand, for the triplet surface, which has an energy barrier, the position of the transition state is well-defined at the top of the barrier. The product state distribution is expected to be determined primarily by the repulsive forces between the fragments as they separate from the transition state. There is experimental evidence for both cases. The CO rotational distribution from room temperature ketene photolyzed at 308 nm, where dissociation occurs mostly to singlet product, agrees well with phase space theory.[20] The CO rotational distributions from rotationally cooled ketene at photolysis energies below the singlet threshold have also been measured, they show Gaussian-shaped distributions, and have been explained using a simple impulsive model.[12] The CO rotational distribution at photolysis energies where both channels are open should be the sum of the rotational

distribution from the singlet and triplet channels. When these distributions are sufficiently different, the singlet/triplet branching ratio can be determined. When combined with the rate measured for the sum of the singlet and triplet channels, the absolute rates for each channel may be determined.

II. EXPERIMENTAL

Ketene is prepared by passing acetic anhydride through a red-hot quartz tube, is trapped at 77 K and distilled twice from 196 to 77 K. Prior to use, the ketene is transferred to a bubbler maintained at 179 K, hexanes (A. C. S. Regent Grade) slush, where its vapor pressure is 50 torr. Two atmospheres of He carrier gas are flowed into the pulsed nozzle after bubbling through the ketene sample. The ketene is cooled in a supersonic free jet and the rotational temperature of ketene in the jet is estimated to be 4.0 ± 0.5 K.[11]

The output of a Lambda-Physik FL2002 dye laser (0.2 cm^{-1} bandwidth) pumped by a Quanta Ray DCR-1A Nd:YAG laser is frequency doubled with a KDP crystal to produce the photolysis pulses. Mixtures of DCM and LD 698, DCM, and Sulforhodamin 6G dyes in methanol are used to produce the resultant UV pulses from 306 to 332 nm with 5-8 mJ/pulse. The wavelength of the photolysis laser is calibrated in the red to $\pm$ 0.6 cm^{-1} by sharp Ne transitions using a Tl/Ne optogalvanic lamp (Hamamatsu).

Another dye laser (Spectra Physics PDL-3) pumped by a second Nd:YAG laser (Spectra Physics DCR-4) is used to generate the pulses around 435 nm (40 mJ/7 ns pulse) using Coumarin 440 in methanol. The beam is focused by a 7.5 cm f.l. quartz lens into a 10 cm long tripling cell filled with

Xe at 20 - 40 torr. The conversion efficiency of the frequency tripling process is about 10^{-6}. The output CaF_2 collimating lens (8 cm f.l.) is about 5 cm from the center of the molecular beam.

The vertically polarized photolysis beam and the horizontally polarized probe beam are counter-propagating and perpendicular to the jet. The time delay between the photolysis laser beam and the probe laser beam is fixed at around 50 ns. The laser induced fluorescence (LIF) of CO product from the dissociation of ketene is detected by a VUV PMT (EMR 542G-09-19, MgF_2 window) mounted at right angles to the laser beams and the jet about 5 cm from the interaction region. A 2.2 cm diameter CaF_2 f/1 lens and a 2.5 mm thick, cultured quartz window (Acton, CQ-1D 50% transmission at 150 nm) are placed before the VUV PMT to increase the collection efficiency and filter out the scattered light. A portion of VUV, which is not absorbed by CO, is detected by using another VUV PMT (EMR 542G-08-19 LiF window) to normalize for VUV intensity fluctuations.

The amplified signals from the PMTs are sent into gated integrators (SRS 250), digitized by an A/D interface board, and stored in a Fountain XT microcomputer. This computer is also used to trigger the lasers, scan the dye laser wavelength, and normalize the signal shot-to-shot.

The transitions from $X^1\Sigma^+(v''=0, J'')$ to $A^1\Pi$ $(v'=3, J')$ and those from $X^1\Sigma^+(v''=1, J'')$ to $A^1\Pi$ $(v'=5, J')$ are used to

determine the rotational distributions of CO(v"=0) and CO(v"=1) product from ketene, respectively. The CO LIF spectra show a linewidth of approximately 0.5 cm^{-1}, which is the result of a convolution of the VUV line width (0.35 cm^{-1}) and the spread of the ketene velocity vectors for the free jet.

The relative population of CO rotational states are calculated from the LIF intensity by using the following formula given by Greene and Zare.[21]

$$I(J", J') \propto C(J") \; S(J", J') \; A_o^{(0)} \; B(J", J')$$

Here the J", J' dependence of the oscillator strength, S, is given by the Hönl-London factors, and $A_o^{(0)}$ is the monopole moment which is equal to unity for photofragmentation. B(J", J') is the excitation-detection configuration factor given by Greene and Zare for the mutually orthogonal geometry.[21] Any alignment factor from the photofragmentation is neglected in the population calculation. The populations from P, Q, and R branches for the same J" state of CO show good agreement among themselves within ± 15 - 20%, and those are randomly distributed, which means that the neglect of any alignment factor is a good approximation. Each data point is averaged for P, Q, and R branches over three scans.

III. RESULTS

The rotational state distribution of fragment CO(v"=0) from ketene dissociation 10 cm^{-1} below the singlet threshold energy of 30 116.2 ± 0.4 cm^{-1}, is shown in Fig. 1 (a). The error bars are the standard deviation for a single scan and give an upper limit on all sources of random and systematic error. Since the ketene is cooled in a supersonic free jet (4K), ketene dissociation may occur only on the triplet surface at this photolysis energy. The solid curve is a best fit to the sum of two Gaussian functions. In earlier work, the CO rotational distributions at photolysis energies below the singlet threshold were measured and the nearly Gaussian observed distributions matched a simple impulsive model including zero-point vibrational motion at the transition state.[12] However, the fit was not good for the CO rotational distribution at 29 412 cm^{-1}. This is high enough to excite the 4-th vibrationally excited level of the C-C-O bending mode at the ab initio transition state, which contributes most of the width to the CO rotation.[12] At this level it is probably necessary to introduce anharmonicity in the C-C-O bend and it is thus not unreasonable to add a second Gaussian to the fit. Some contribution from $^3CH_2$ bending excited states must also be expected.

The CO(v"=0) rotational distribution 56 cm^{-1} above the singlet threshold is bimodal, Figs. 1 (b) and 2. Since both

the singlet and triplet channels are open at this photolysis energy, the CO rotational distribution is considered as the sum of the distributions from the singlet and triplet channels. Only low rotational quantum numbers are energetically accessible for CO product in the singlet channel at this low excess energy. Therefore, the peak at low J's in Fig. 2 is clearly assigned to CO product from ketene dissociation in the singlet channel and the broad peak at high J's corresponds to CO from dissociation in the triplet channel. The ratio of these two peak areas gives the singlet/triplet branching ratio at this photolysis energy. The singlet peak is fit to the phase space theory (PST) CO rotational distribution calculated as in Ref. 20 without any adjustable parameters. The curve which fits the experimental result at 30 106 cm^{-1} is used for the CO rotational distribution from the triplet channel. The solid curves in Figs. 1 (b) and 2 are the sum of these two distributions for a singlet yield of 0.15 and a triplet yield of 0.85. The singlet yield at this energy is thus estimated to be 0.15 ± 0.02.

The CO(v"=0) rotational distributions at 30 226 cm^{-1}, 30 441 cm^{-1}, and 30 541 cm^{-1}, excess energies above the singlet threshold of 110 cm^{-1}, 325 cm^{-1}, and 425 cm^{-1}, respectively, are shown in Figs. 1 (c), (d), and (e). The solid curves are fits as in Fig. 2 and give singlet yields of 0.34 ± 0.02, 0.60 ± 0.06, and 0.62 ± 0.06, respectively.

Fig. 1 (f) shows the CO(v"=0) rotational distribution at 1107 cm^{-1} above the singlet threshold. At this excess energy, the high J states of CO from the singlet channel overlap the triplet channel distribution. The PST calculation for the CO rotational distribution from the singlet channel is presumed to be good even at this high excess energy and the CO rotational distribution from the triplet channel is assumed to be the same as that for 10 cm^{-1} below the singlet threshold. With these assumptions, the solid curve in Fig. 1 (f) fits the experimental data well for a singlet yield of 0.65 ± 0.07. Under the same assumptions, the singlet yields at 1435 cm^{-1}, 1720 cm^{-1}, and 2500 cm^{-1} above the singlet threshold are estimated to be 0.70 ± 0.07, 0.80 ± 0.08, and 0.70 ± 0.15, respectively (Figs. 1 (g)-(i)). Especially, at 2500 cm^{-1} the overlap of the singlet and triplet distributions makes it impossible to determine an accurate triplet yield.

The branching ratios are derived from the data by assuming that PST accurately gives the CO rotational distribution from the singlet channel and that the CO rotational distribution from the triplet channel changes little with increasing photolysis energy. At low excess energies (56 - 425 cm^{-1}), CO rotational distributions show easily resolved bimodal distributions (Figs. 1 (b)-(e)). PST calculations for CO rotational distributions from the singlet channel at these low excess energies show excellent agreement with the experimental results and CO rotational

distributions from the triplet channel appear to be little changed from that at 10 cm^{-1} below the singlet threshold. At low excess energies this simple treatment works well.

But at higher excess energies, CO rotational distributions from singlet and triplet overlap, and the data do not provide enough information to simultaneously test the model assumptions and extract a singlet/triplet yield ratio. At high enough excess energy for the vibrationally excited product to be populated, the yield of the vibrationally excited product has been found to be larger than predicted by PST calculation and close to the variational RRKM prediction.[16,17,20] Klippenstein and Marcus have calculated CO rotational distributions for the singlet channel at several photolysis energies using both PST and their version of variational RRKM theory.[17] The only difference between the distributions is that the variational RRKM calculation moves population from high J's of v"=0 to the v"=1 channel. This difference is small and no attempt has been made to fit the experimental results with models other than PST for the singlet channel.

On the other hand, CO rotational distributions for the triplet channel are certainly expected to shift to higher J and to broaden as total energy increases. This has been observed[12], but there is no reliable theory to predict the CO(J) distribution from the triplet channel above the singlet threshold. The ratio of the average CO rotational energy to

the total available energy (the photolysis energy minus D(CH_2-CO)) is 22.4% for photolysis energies below 29 412 cm^{-1}.[12] But, at 30 106 cm^{-1}, 10 cm^{-1} below the singlet threshold, the ratio decreases to 21.0%. From a straight-line extrapolation to higher energies, the ratio of CO rotational energy to the total available energy for the triplet channel can be estimated to be 20%, 18%, and 16% at 425, 1435, and 2500 cm^{-1} excess energies above the singlet threshold, respectively. The corresponding Gaussian-shaped CO rotational distributions which peak at 18, 19, and 20 with ΔJ (the full widths in J)= 18, 19, and 20, respectively, can be predicted for the triplet CO rotational distributions. These Gaussian-shaped CO rotational distributions give yields which are within the error limits of the branching ratios in Table I. For data at 2500 cm^{-1}, Gaussian shaped distributions peaked at J = 19, 20, and 21 with ΔJ = 19, 20, and 21, respectively, give singlet yields of 0.75, 0.80, and 0.85. The best overall fit to the data is obtained with a singlet yield of 0.80 as shown in Fig. 3.

For all photolysis energies in this work, vibrationally excited CO(v"=1) from the dissociation of ketene on the triplet channel is energetically possible.[11] No significant laser induced fluorescence (LIF) signal < 0.5% of v"=0, from CO(v"=1) up to 1720 cm^{-1} above the singlet threshold was detected, which means that CO(v"=1) from the triplet channel introduces a correction of less than 0.5% to the branching

ratios measured from the CO(v"=0) rotational distributions. At 2500 cm^{-1} above the singlet threshold, where the singlet yield is not much different from that at 1720 cm^{-1} (Table I), vibrationally excited CO(v"=1) products from both channels are energetically accessible and CO(v"=1), which is mainly from the singlet channel, is readily detected.

The rotational distribution for the vibrationally excited CO at 2500 cm^{-1} excess energy is shown in Fig. 4 with the PST calculation for the singlet channel. The overall shape of the distribution shows qualitatively good agreement with that of the PST calculation, though there is an excess population observed at relatively high J's. This extra population might be due to CO from dissociation of vibrationally hot ketene in the supersonic jet. The ratio of the CO(v"=1) population to the CO(v"=0) population is estimated to be 0.034 ± 0.009 after correcting for the difference in Franck-Condon factors of 0.18 for (3-0) and 0.13 for (5-1) bands[22] and summing all rotational populations of each vibrational state. The rotational dependence of Franck-Condon factors is small and neglected. The detection sensitivity of the PMT for LIF signals from the two bands is assumed to be the same for the distribution of fluorescence from v'=3 and v'=5.

IV. DISCUSSION

The singlet yield versus excess energy above the singlet threshold shows a rapid increase in the 0 - 300 cm^{-1} excess energy region and a slower increase above, Fig. 5. The total rate constant for ketene dissociation, the sum of the rate constants for singlet and triplet channels, has been directly measured as a function of energy by Potter et al..[18] Those measurements show that PST overestimates the singlet rate constant even for excess energies as low as 500 cm^{-1} above the singlet threshold and that a variational RRKM calculation for the singlet rate constant shows good agreement with the observed total rate constants over a wide energy range (450 - 5000 cm^{-1}). The triplet rate constants at several photolysis energies below the singlet threshold have been determined by measurement of CO appearance rates.[11] An RRKM calculation gives an accurate fit to the data near threshold but predicts a much faster increase with increasing photolysis energy than the experimental results. A good fit to the experimental results was obtained by treating the triplet rate as limited by a constant intersystem crossing rate.[11] The dashed line in Fig. 6, which fits the triplet rate constants at photolysis energies below the singlet threshold has been obtained for an intersystem crossing rate of 2.8×10^{8} s^{-1}.

From the singlet/triplet branching ratios measured in

this work, it is now possible to extract the triplet and singlet rate constants from the measured total rate constants. At excess energies of 450 to 2500 cm^{-1}, the triplet and singlet rate constants are obtained from the experimentally measured total rate constants and branching ratios (Fig. 7). The singlet rate constant obtained agrees well with variational RRKM. The experimental results from Ref. 11 and this work define a smooth curve for the triplet rate as shown by the dash-dot line in Figs. 6 and 7.

This monotonic increase with photolysis energy can be explained either by treating the triplet rate as being limited by an intersystem crossing rate which increases with energy, or by introducing of variational RRKM theory for the triplet channel. At the singlet threshold the energy for the triplet channel is a factor of two greater than the barrier height. It is thus reasonable to propose, as in variational RRKM theory, that the transition state for the triplet channel may move in along the reaction coordinate with increasing excess energy. This would give a slower increase of the triplet rate constant than for standard RRKM theory.

For energies less than 400 cm^{-1} above the singlet threshold, the total rate constant measurements are not available. However, the variational RRKM and PST predictions for the singlet rate constant can be used with the branching ratios to estimate triplet rate constants. In PST, the number of open singlet channels is directly counted for the

specific angular momentum, parity, and nuclear spin state of the excited ketene as a function of the excess energy above the singlet threshold. The density of reactant states is calculated by using the Whitten-Rabinovich formula[23], multiplied by (2J'+1) which is a degeneracy factor for K, and divided by four because there are four symmetry classes in the CNPI group for ketene.[14] The mean reaction time rate constant after thermal averaging for 4K is calculated according to the method in Refs. 11 and 17. The results are shown in Table I.

At 56 cm^{-1} excess energy, variational RRKM and PST give the same singlet rate constant. If the theoretical singlet rate constant at 56 cm^{-1} is combined with the experimental branching ratio to calculate the triplet rate constant, the point falls exactly on the experimentally defined curve for the triplet, Figs. 6 and 7. Variational RRKM starts to deviate from PST near 70 cm^{-1} excess energy.[24] At 110 cm^{-1} and 325 cm^{-1}, PST predicts a rate faster than predicted by variational RRKM by factors of 1.7 and 4.0, respectively. If variational RRKM singlet rate constants at these low excess energies (110 - 325 cm^{-1}) are used to calculate the triplet rate constants from the branching ratio measurements, the resultant triplet rate constants fall about 20% below the experimentally defined curve for k_t. They do show quantitatively good agreement with the fit to the low energy data obtained in Ref. 11 by assuming an intersystem crossing

rate of 2.8×10^8 s^{-1}. But the triplet rate constant, which is obtained from the variational RRKM singlet rate constant and the branching ratio at 110 cm^{-1}, is about 25% smaller than for 56 cm^{-1} excess energy (Fig. 6). This suggests that the variational RRKM rates in the 100 - 325 cm^{-1} region are about 20% smaller than the true singlet rate constants.

If the singlet rate constants at low excess energies (110 - 325 cm^{-1}) are assumed to be correctly given by PST, the resultant triplet rate constants, which are calculated from the branching ratios, show a rapid increase with increasing excess energy and the triplet rate constant at 325 cm^{-1} is 2.4 times larger than that obtained from experimental data at 450 cm^{-1}. The PST rates are clearly too large. The singlet rate constant at 110 cm^{-1} can be calculated using the branching ratio measurements and the triplet curve(-.-) in Figs. 6 and 7. The logarithm is 8.14, which is between the variational RRKM calculation of 8.00 and the PST value of 8.25. At 325 cm^{-1} excess energy, Log k_s= 8.68 is estimated compared to the PST and variational RRKM values of 9.19 and 8.60, respectively. Therefore, the singlet rate in the low excess energy region (56 -325 cm^{-1}), seems to increase with a slope between that of variational RRKM and PST.

Recently, Klippenstein and Marcus have calculated the vibrational and rotational product state distributions for ketene dissociation on the singlet surface at several photolysis energies by using PST and their version of

variational RRKM theory, which assumes adiabaticity for the conserved vibrational mode after the transition state is passed, but allows nonadiabaticity for the rotational degrees of freedom.[17] As mentioned earlier, the product rotational distributions calculated from both theories are nearly the same up to 2500 cm^{-1} excess energy above the singlet threshold. But the vibrational distributions from PST and the variational RRKM theory are different. Results for singlet methylene vibrational excitation are given in Ref. 16. For the CO product, the ratio of CO(v"=1) to CO(v"=0) at 2500 cm^{-1} excess energy above the singlet threshold is calculated to be 0.038 from variational RRKM theory. The separate statistical ensembles (SSE) model of Wittig and coworkers yields 0.041, using Eq. (4) of the following paper. PST gives 0.016.[17] The experimental result in this work is $(0.034 \pm 0.009)/\Phi_s$. The singlet yield at 2500 cm^{-1} excess energy is estimated to be 0.80 ± 0.10 from Fig. 5, and the corresponding ratio of CO(v"=1) to CO(v"=0) is 0.045 ± 0.017. This value is much closer to the variational RRKM and SSE models than to PST.

REFERENCES

(1) R. D. Levine and J. L. Kinsey, in Atom-Molecular Collision Theory - A Guide for the Experimentalist, edited by R. B. Bernstein (Plenum, New York, 1979).

(2) P. Pechukas and J. C. Light, J. Chem. Phys. 42, 3281 (1965).

(3) C. E. Klots, J. Phys. Chem. 75, 1526 (1971).

(4) M. Quack and J. Troe, Ber. Bunsenges. Phys. Chem. 78, 240 (1974); 79, 170 (1975); 79, 469 (1975).

(5) L. Brouwer, C. J. Cobos, J. Troe, H.-R. Dubal, and F. F. Crim, J. Chem. Phys. 86, 6171 (1987).

(6) C. Wittig, I. Nadler, H. Reisler, J. Catanzarite, and G. Radhakrishnan, J. Chem. Phys. 83, 5581 (1985).

(7) P. J. Robinson and K. A. Holbrook, Unimolecular Reactions (Wiley-Interscience, London, 1972).

(8) W. Forst, Theory of Unimolecular Reactions (Academic, N. Y. and London, 1973).

(9) D. M. Wardlaw and R. A. Marcus, Chem. Phys. Lett. 110, 230 (1984); J. Chem. Phys. 83, 3462 (1985).

(10) P. R. Bunker, P. Jensen, W. P. Kraemer, and R. Beardsworth, J. Chem. Phys. 85, 3724 (1986).

(11) I.-C. Chen and C. B. Moore, J. Phys. Chem. 94, 263 (1990).

(12) I.-C. Chen and C. B. Moore, J. Phys. Chem. 94, 269 (1990).

(13) W. H. Green, Jr., I.-C. Chen, and C. B. Moore, Ber. Bunsenges. Phys. Chem. 92, 389 (1988).

(14) I.-C. Chen, W. H. Green, Jr., and C. B. Moore, J. Chem. Phys. 89, 314 (1988).

(15) H. Reisler and C. Wittig, Annu. Rev. Phys. Chem. 37, 307 (1986).

(16) W. H. Green, Jr., A. J. Mahoney, C.-K. Cheng, and C. B. Moore, J. Chem. Phys. 94, 1961 (1991).

(17) S. J. Klippenstein and R. A. Marcus, J. Chem. Phys. 91, 2280 (1989).

(18) E. D. Potter, M. Gruebele, L. R. Khundkar, and A. H. Zewail, Chem. Phys. Lett. 164, 463 (1989).

(19) W. H. Green, Jr., Ph. D. Dissertation, University of California, Berkeley, 1988.

(20) D. J. Nesbitt, H. Petek, M. F. Foltz, S. V. Filseth, D. J. Bamford, and C. B. Moore, J. Chem. Phys. 83, 223 (1985).

(21) C. H. Greene and R. N. Zare, J. Chem. Phys. 78, 6741 (1983).

(22) R. L. Kurucz, Smithsonian Astrophysical Observatory, Special Report 374 (1976).

(23) I. W. M. Smith, Kinetics and Dynamics of Elementary Gas Reactions (Butterworths, London, 1980).

(24) S. J. Klippenstein, private communication.

Table I. Rate constants for dissociation of ketene vs. Energy.

			log k_t[b]			log k_s		
E[a]	Φ_s[c]	log(k_s+k_t)	Expt.	var-RRKM	PST	Expt.	var-RRKM	PST
56	0.15 (0.02)	--	8.43 (0.07)	8.43	8.43	7.68 (0.07)	7.68	7.68
110	0.34 (0.02)	--	8.45 (0.07)	8.30	8.54	8.14 (0.07)	8.00	7.68
325	0.60 (0.05)	--	8.50 (0.05)	8.42	9.01	8.68 (0.05)	8.60	9.19
450	0.62[d] (0.05)	9.04 (0.03)	8.62 (0.08)	--	--	8.83 (0.08)	8.80	9.40
1107	0.65 (0.08)	9.38 (0.07)	8.92 (0.08)	--	--	9.19 (0.09)	9.40	10.1
1435	0.70 (0.07)	9.59 (0.04)	9.06 (0.14)	--	--	9.43 (0.15)	9.60	10.4
1720	0.80 (0.08)	9.70 (0.10)	9.00 (0.30)	--	--	9.60 (0.32)	9.75	10.5
2521	0.70[d] (0.20)	10.0 (0.10)	9.33 (0.37)	--	--	9.88 (0.39)	10.0	10.8

a. The excess energy in cm^{-1} above the singlet threshold of 30,116.2 cm^{-1}.

b. The values are calculated from the var-RRKM singlet rate constants and the PST values of k_s.

c. Errors in parentheses are estimated from the fits in Figure 1.

d. The singlet yields measured at 425 and 2500 cm^{-1} are used for the rate constants at 450 and 2521 cm^{-1}, respectively.

Figure 1. The rotational distributions of CO(v"=0) products from ketene dissociations at photolysis energies below and above the singlet threshold energy (30 116.2 cm^{-1}). (a): The CO rotational distribution and the fit using two Gaussians at 10 cm^{-1} below the singlet threshold. The followings are the excess energies above the singlet threshold of the photolysis energies and the singlet yields corresponding to the best fits for (b)-(i).

(b): 56 cm^{-1}; 0.15, (c): 110 cm^{-1}; 0.34, (d): 325 cm^{-1}; 0.60, (e): 425 cm^{-1}; 0.62, (f): 1107 cm^{-1}; 0.65, (g): 1435 cm^{-1}; 0.70, (h): 1720 cm^{-1}; 0.80, (i): 2500 cm^{-1}; 0.75.

Figure 1-(a)

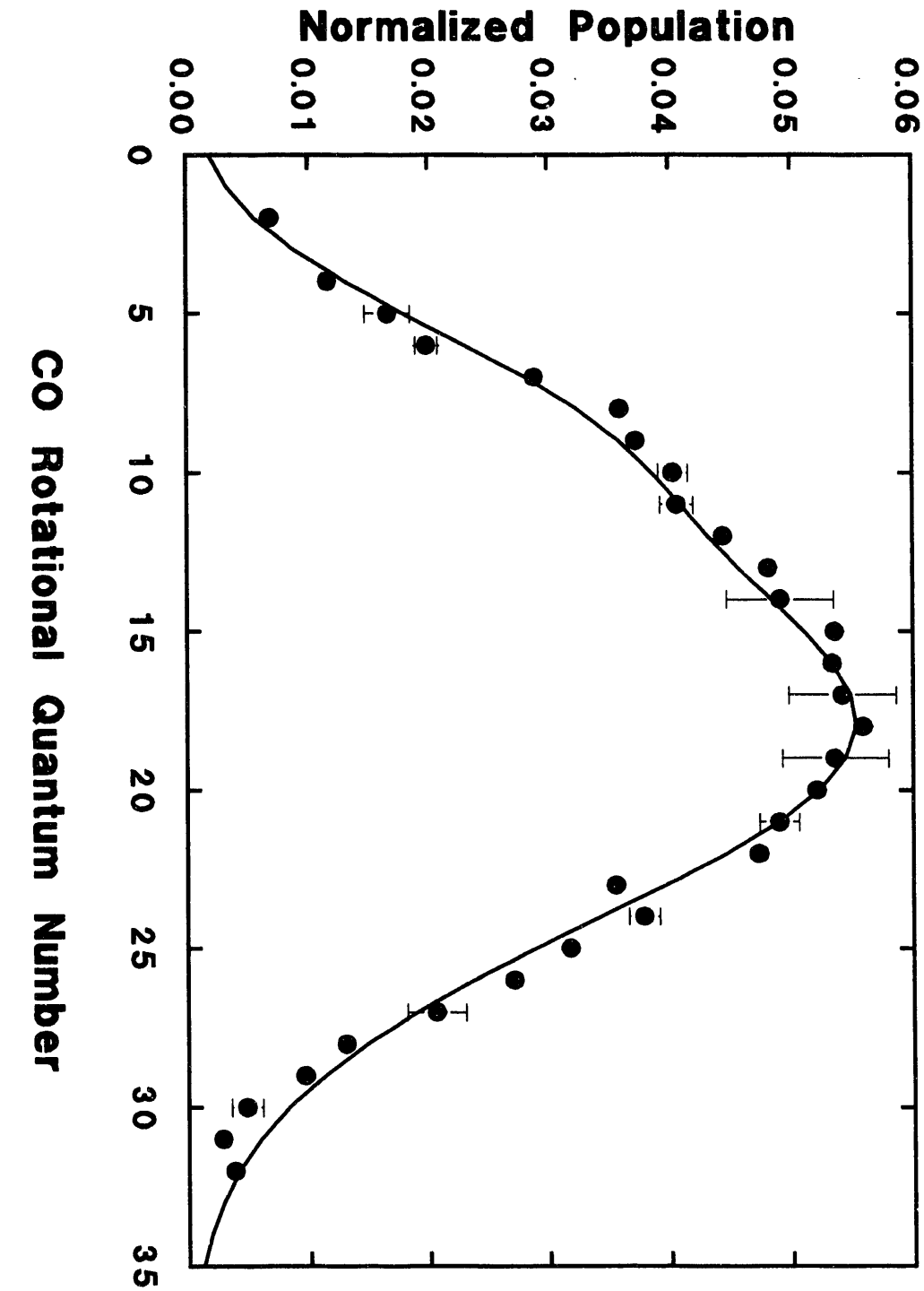
Normalized Population
0.00
0.01
0.02
0.03
0.04
0.05
0.06
0
5
10
15
20
25
30
35
CO Rotational Quantum Number

Figure 1 - (b)

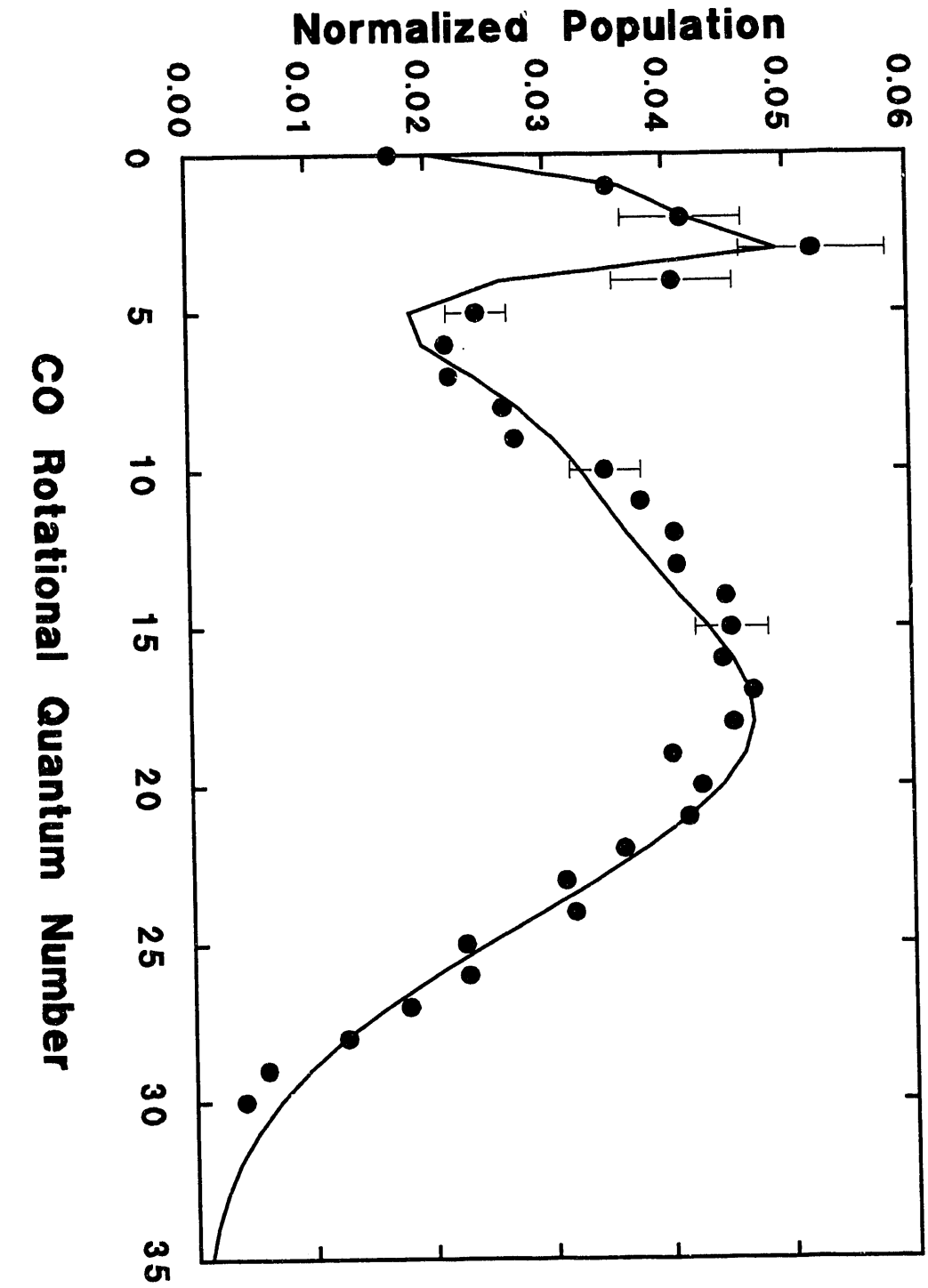
Normalized Population
0.00
0.01
0.02
0.03
0.04
0.05
0.06
0
5
10
15
20
25
30
35
CO Rotational Quantum Number

Figure 1-(c)

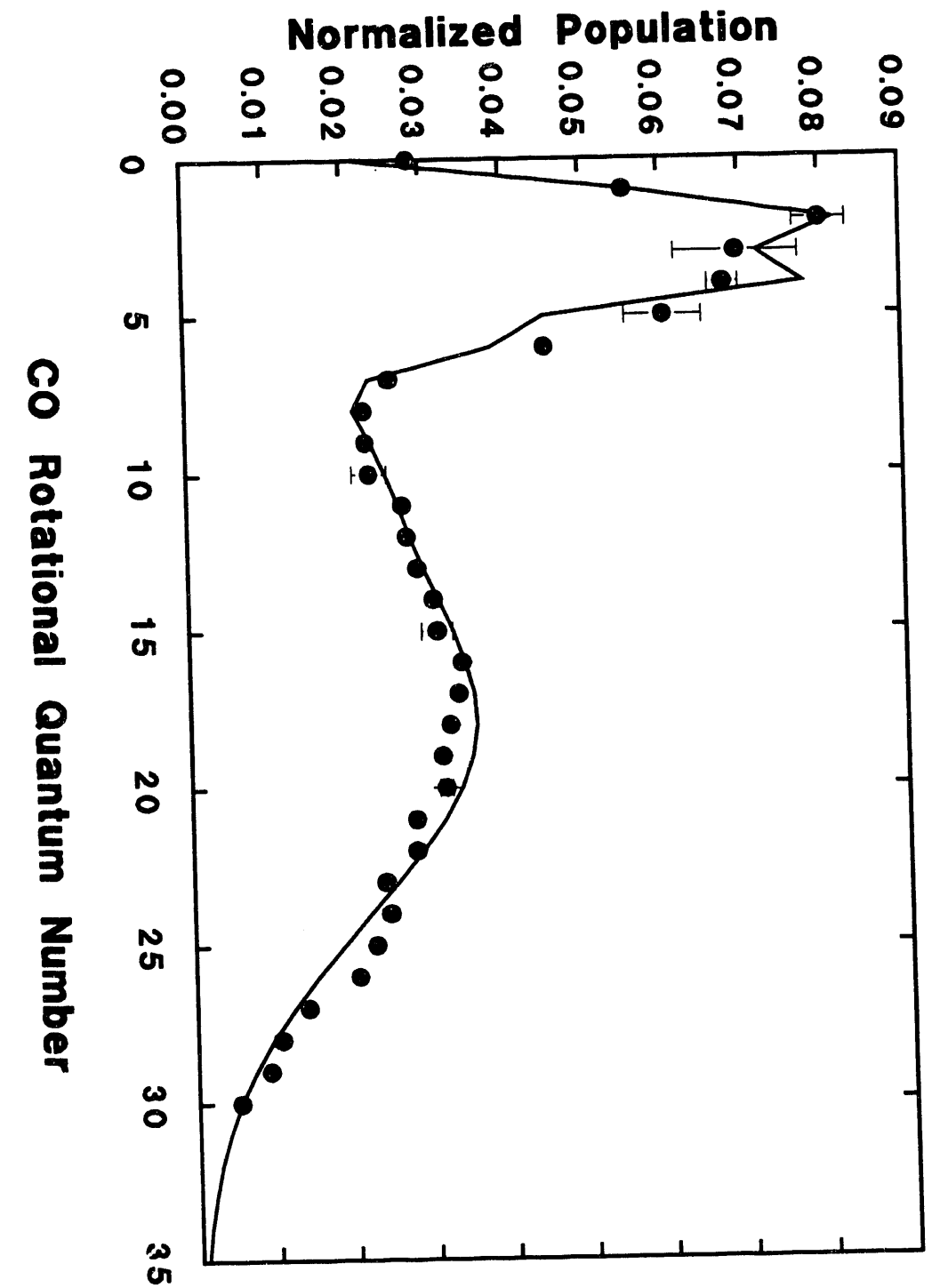
Normalized Population
0.00
0.01
0.02
0.03
0.04
0.05
0.06
0.07
0.08
0.09
0
5
10
15
20
25
30
35
CO Rotational Quantum Number

Figure 1-(d)

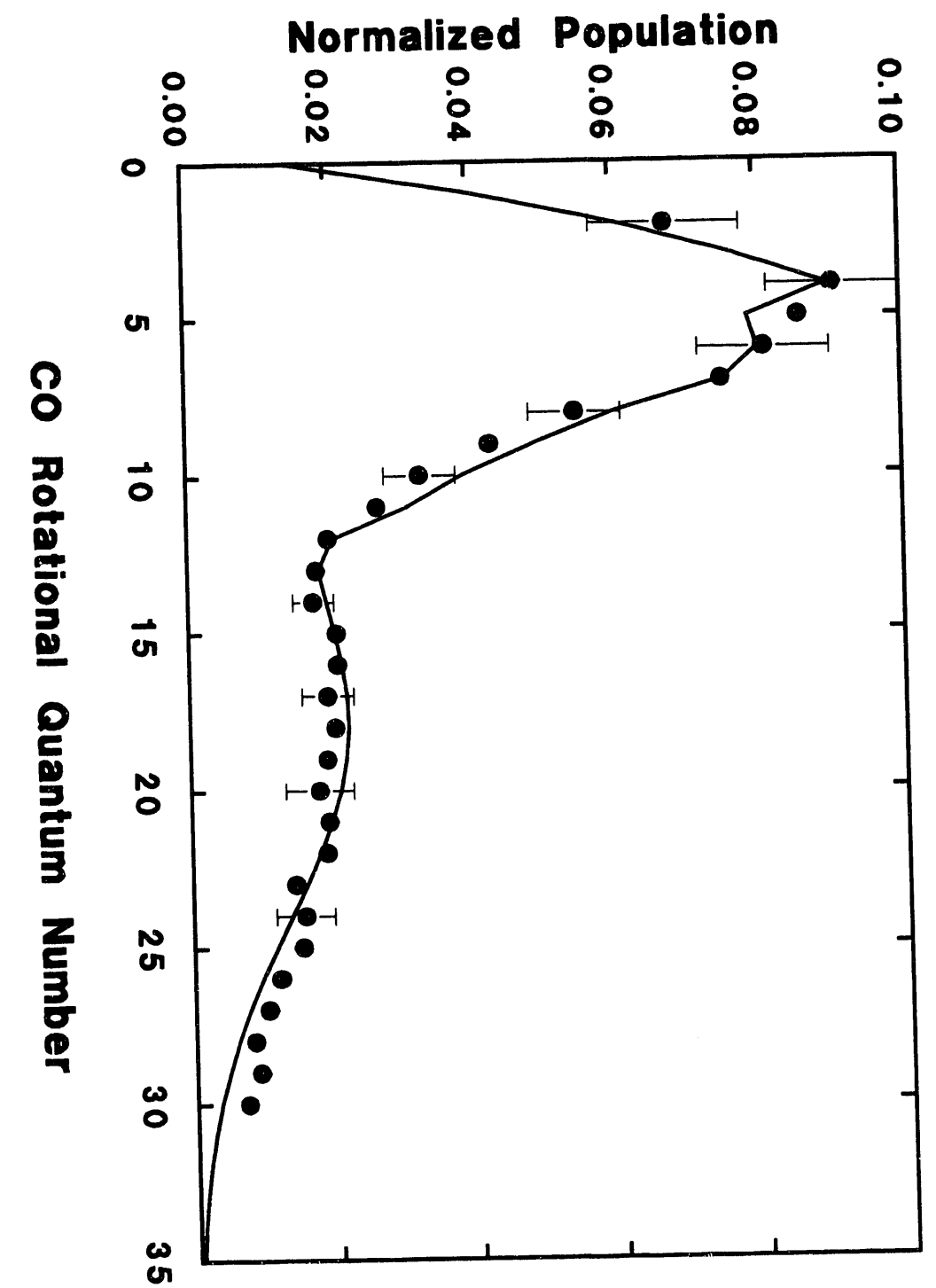
Normalized Population
0.00
0.02
0.04
0.06
0.08
0.10
0
5
10
15
20
25
30
35
CO Rotational Quantum Number

Figure 1-(e)

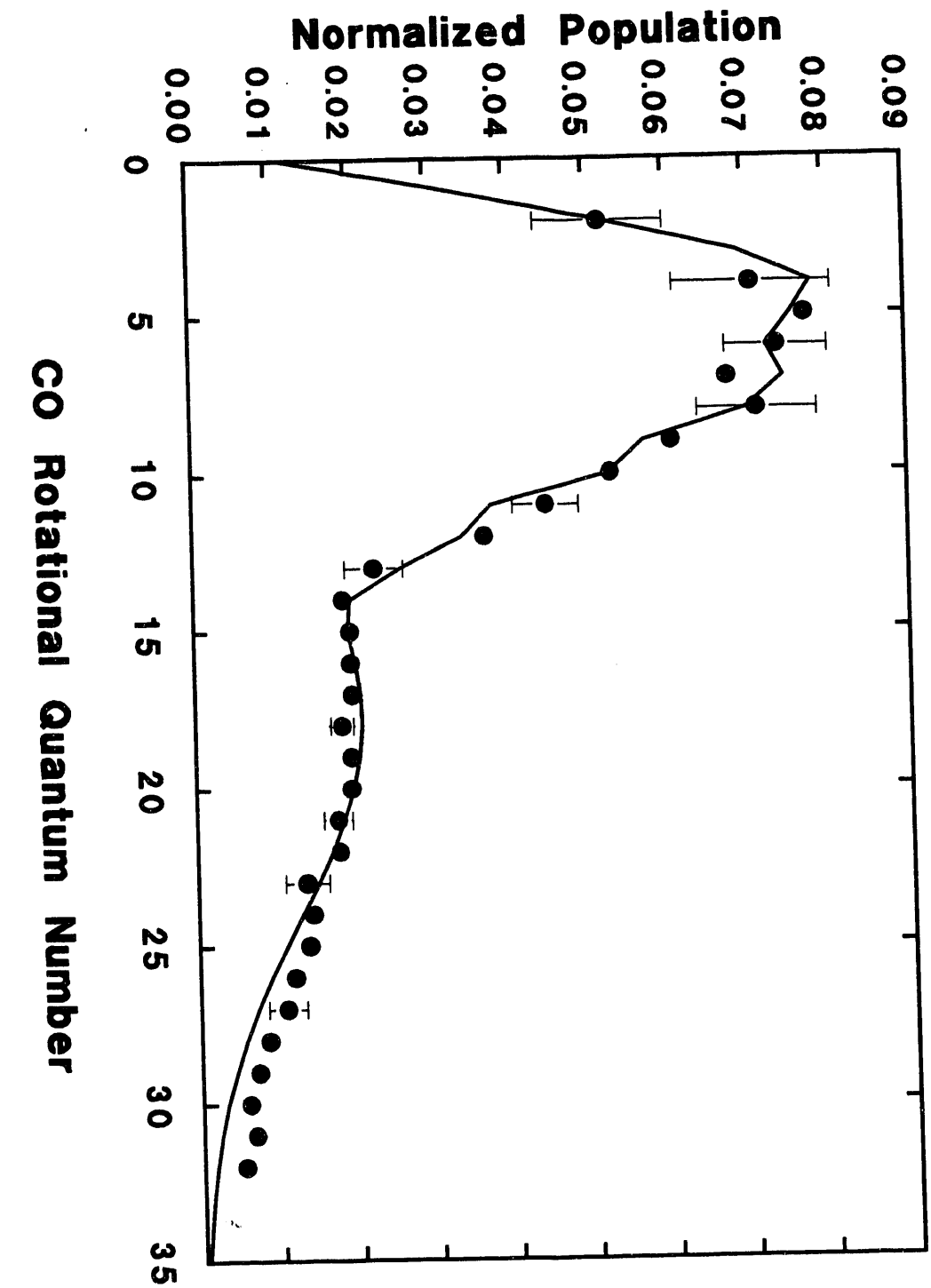
Normalized Population
0.00
0.01
0.02
0.03
0.04
0.05
0.06
0.07
0.08
0.09
0
5
10
15
20
25
30
35
CO Rotational Quantum Number

Figure 1-(f)

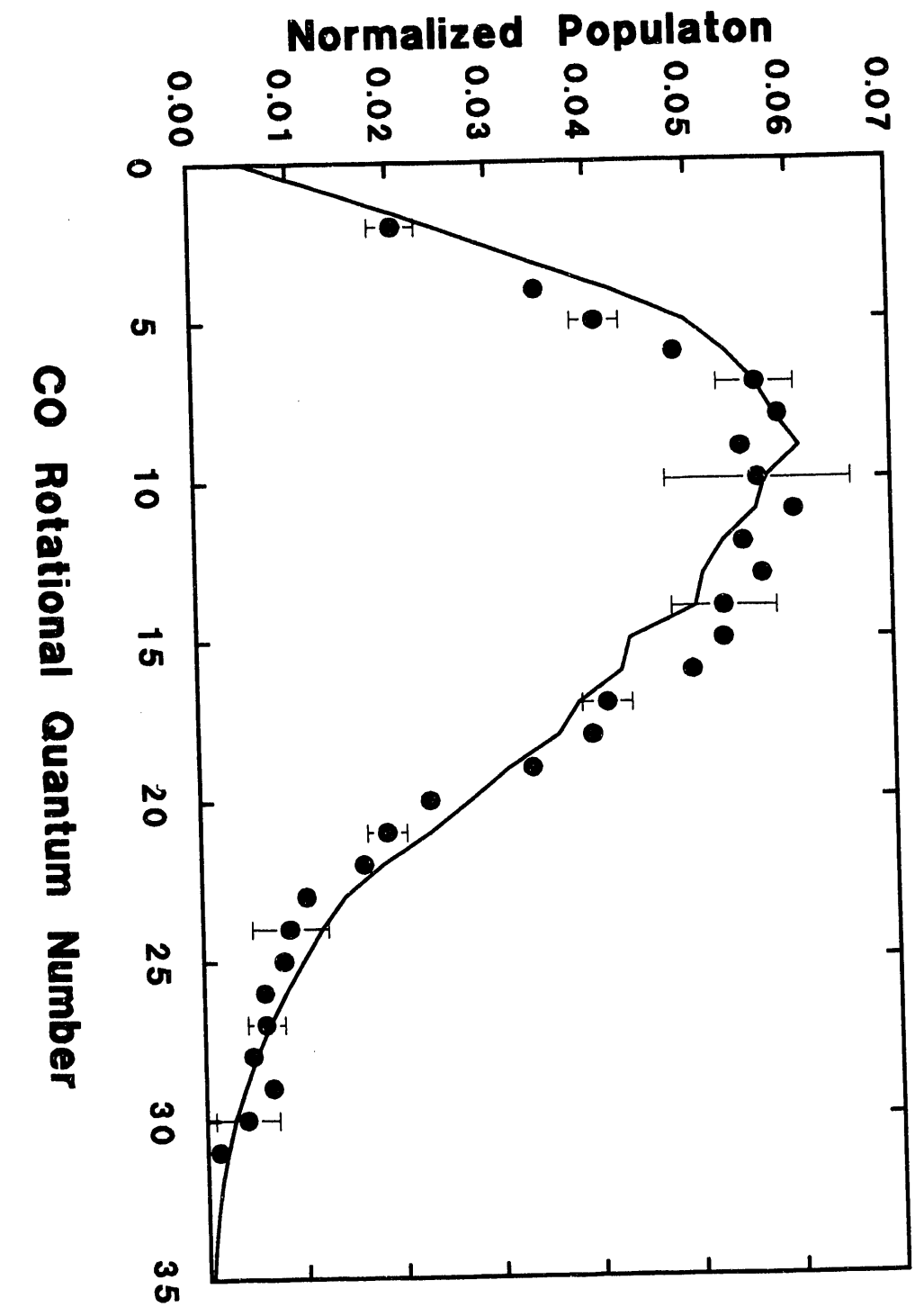
Normalized Populaton
0.00
0.01
0.02
0.03
0.04
0.05
0.06
0.07
0
5
10
15
20
25
30
35
CO Rotational Quantum Number

Figure 1-(g)

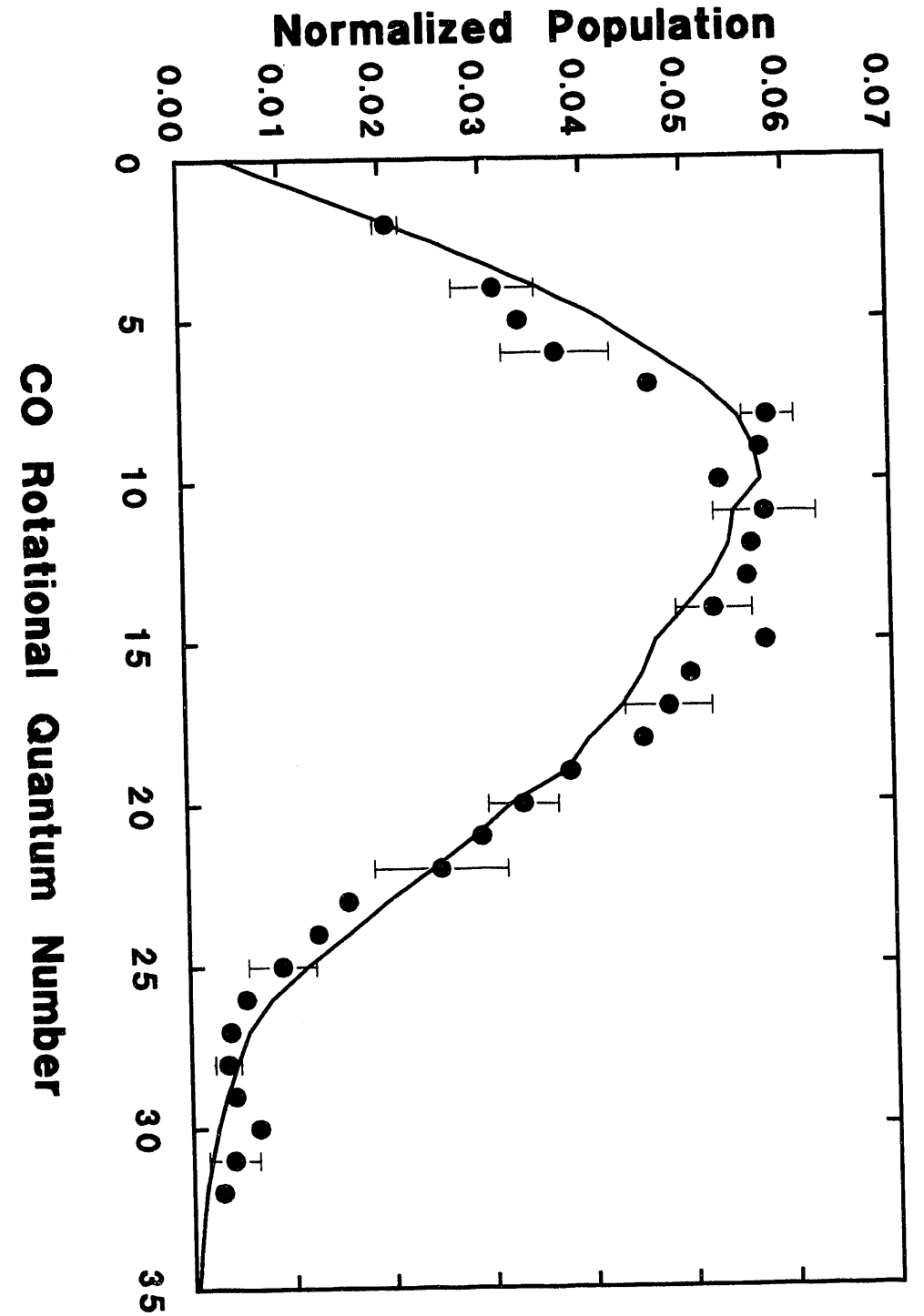
Normalized Population
0.00
0.01
0.02
0.03
0.04
0.05
0.06
0.07
0
5
10
15
20
25
30
35
CO Rotational Quantum Number

Figure 1-(h)

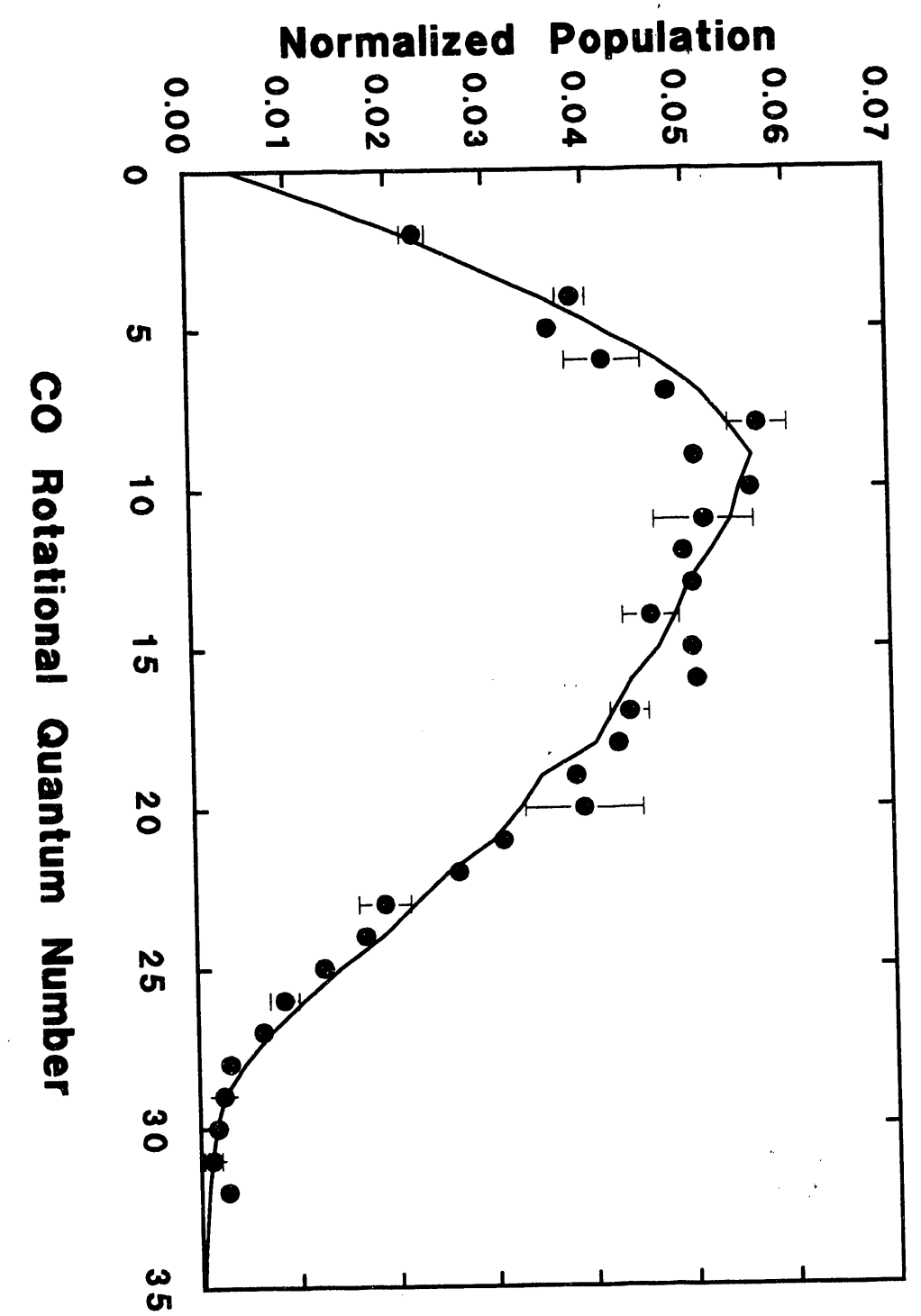
Normalized Population
0.00
0.01
0.02
0.03
0.04
0.05
0.06
0.07
0
5
10
15
20
25
30
35
CO Rotational Quantum Number

Figure 1-(i)

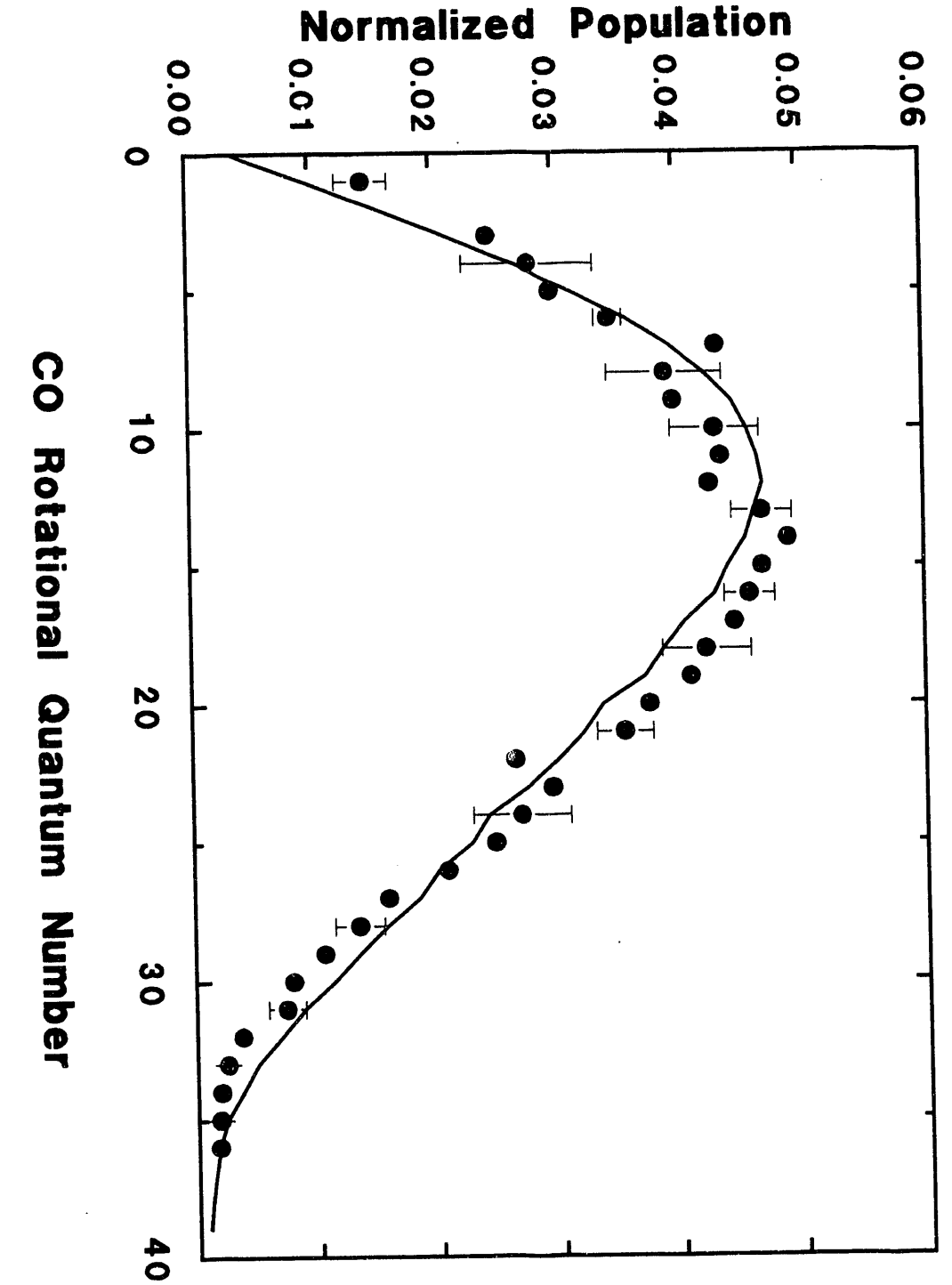
Normalized Population
0.00
0.01
0.02
0.03
0.04
0.05
0.06
0
10
20
30
40
CO Rotational Quantum Number

Figure 2. CO(v"=0) rotational distribution at 56 cm^{-1} above the singlet threshold is best fit with a singlet yield of 0.15. The curve (---) is the singlet contribution with a shape calculated from PST and the curve (...) is the triplet contribution.

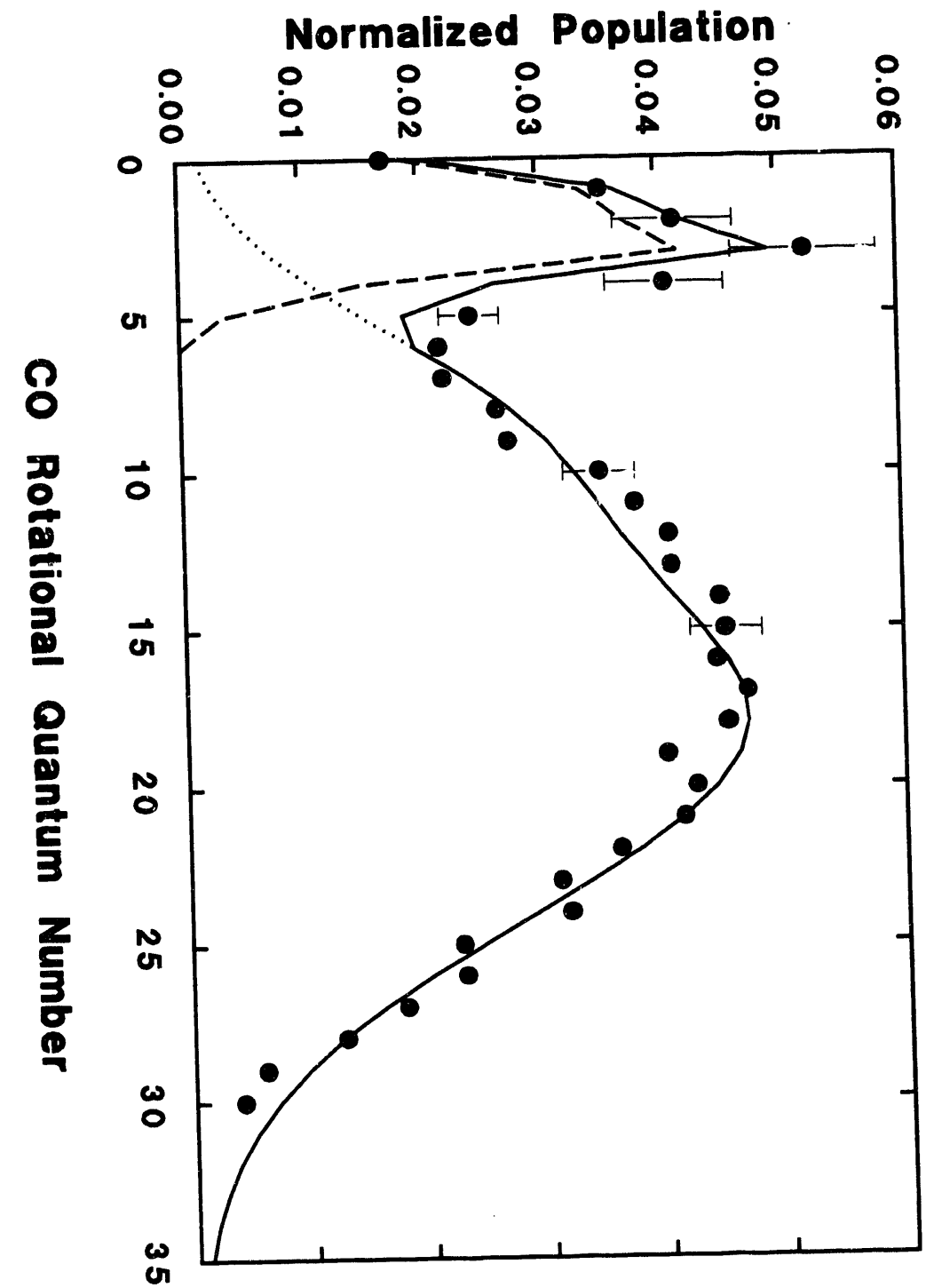
Normalized Population
0.00
0.01
0.02
0.03
0.04
0.05
0.06
0
5
10
15
20
25
30
35
CO Rotational Quantum Number

Figure 3. CO(v"=0) rotational distribution at 2500 cm^{-1} above the singlet threshold and a fit where the singlet yield is 0.80. A Gaussian curve (...) which peaks at 20 (ΔJ = 20) is used for the contribution of CO from the triplet channel. The curve (---) is the PST calculated singlet contribution.

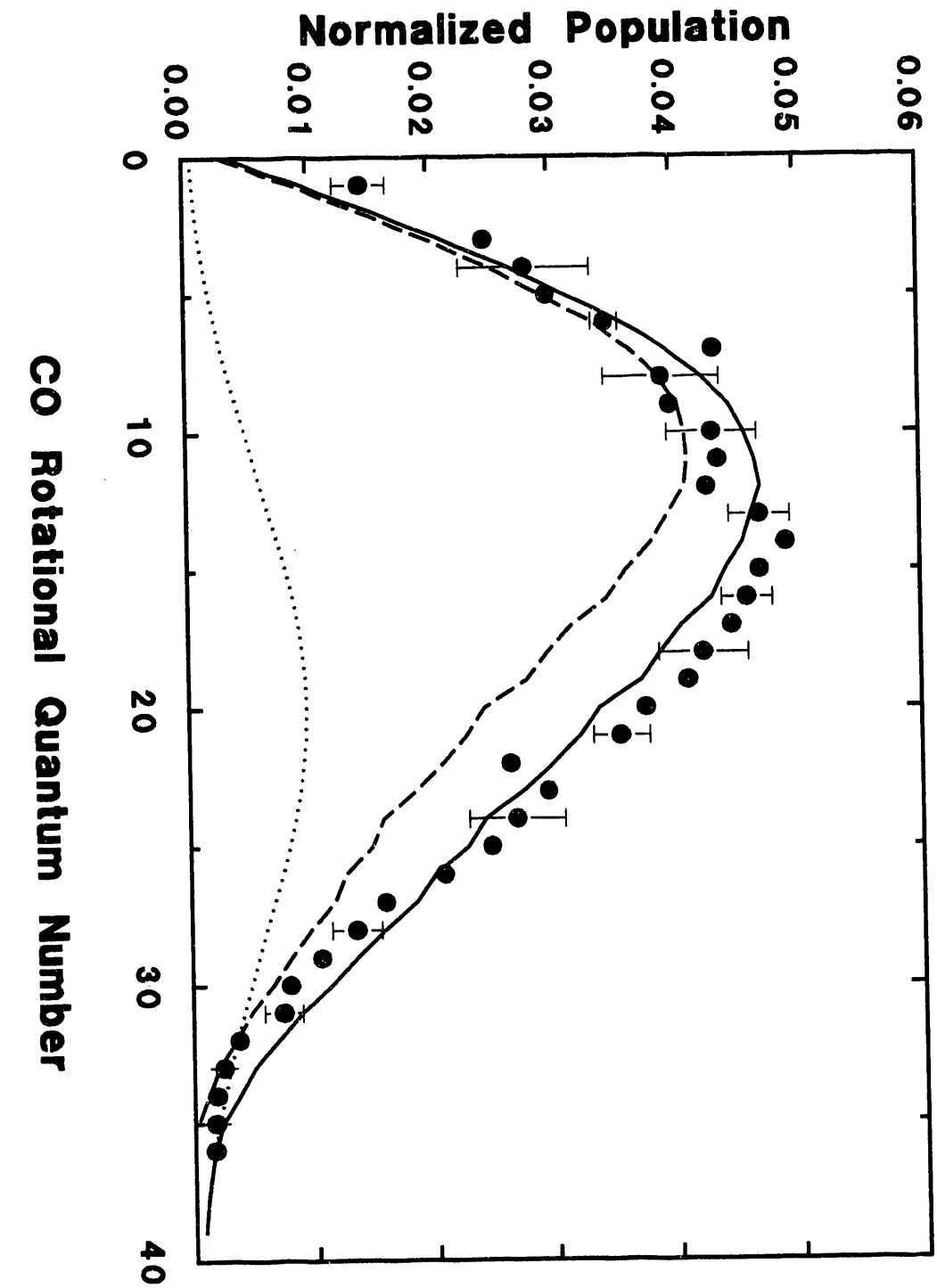
Normalized Population
0.00
0.01
0.02
0.03
0.04
0.05
0.06
0
10
20
30
40
CO Rotational Quantum Number

Figure 4. CO(v"=1) rotational distribution at 2500 cm^{-1} above the singlet threshold (filled circles), compared to the PST distribution (filled triangles). Both populations are normalized to unity for the comparison.

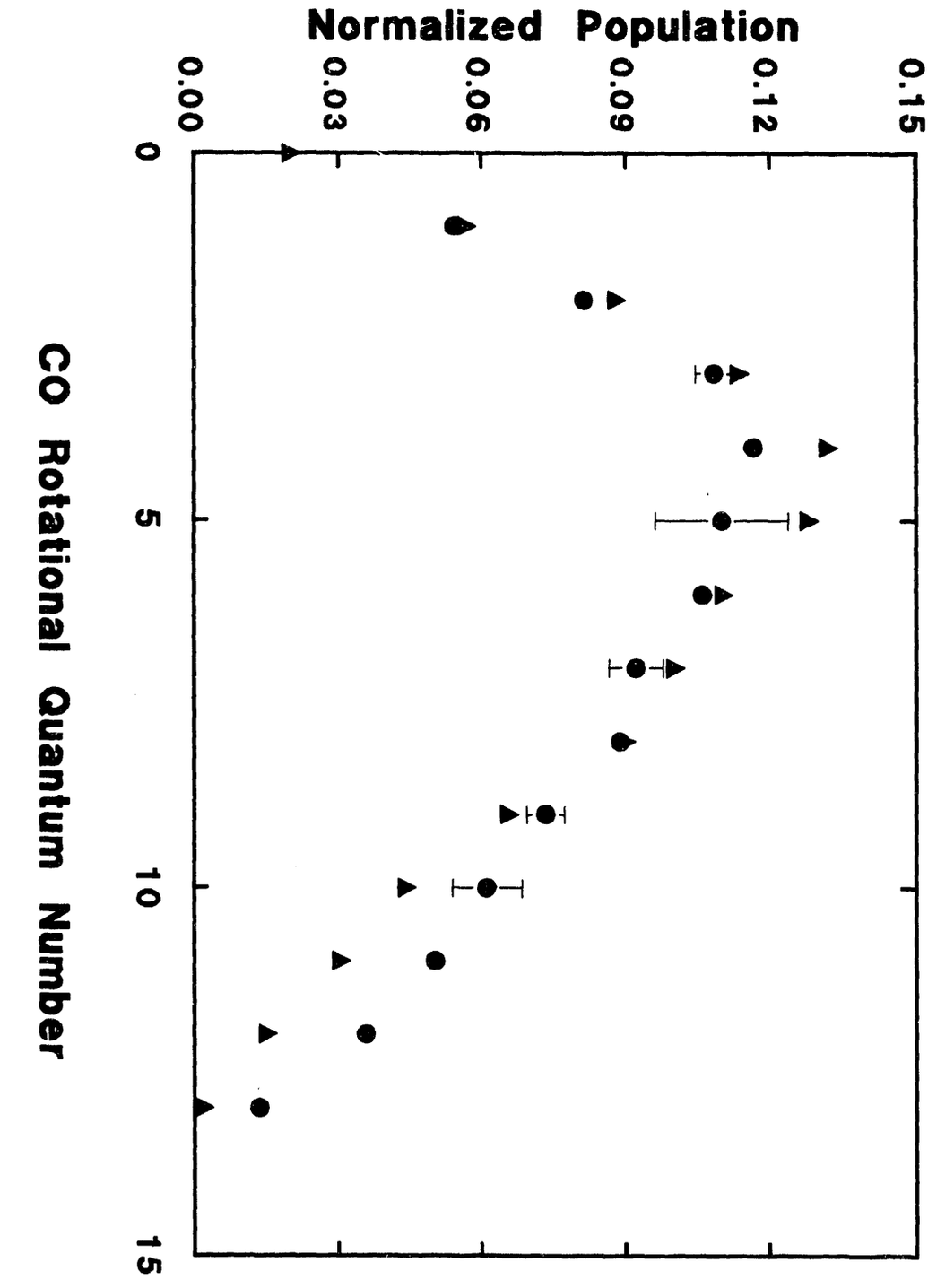
Normalized Population
0.00
0.03
0.06
0.09
0.12
0.15
0
5
10
15
CO Rotational Quantum Number

Figure 5. The singlet yield as a function of the excess energy above the singlet threshold. The curve (---) is a smooth interpolation which is drawn just to help the eyes.

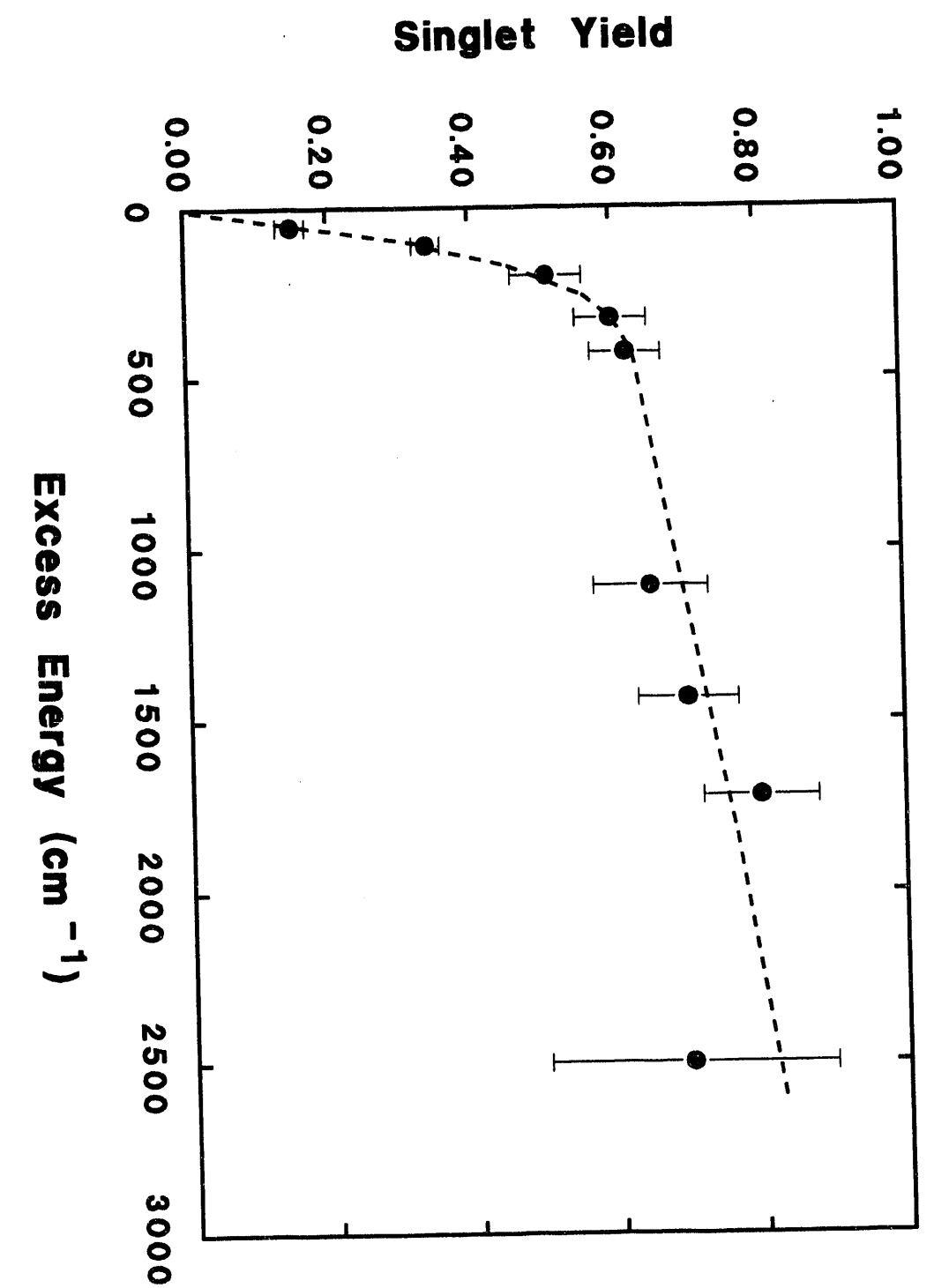
Singlet Yield
0.00
0.20
0.40
0.60
0.80
1.00
0
500
1000
1500
2000
2500
3000
Excess Energy (cm⁻¹)

Figure 6. The energy dependent triplet dissociation rate constant of ketene. The filled circles are the directly determined rate constants.[11] The filled triangles and squares are the triplet rate constants calculated from PST and variational RRKM singlet rate constants, respectively. At 56 cm^{-1} above the singlet threshold, both calculations give the same result. The solid curve is a RRKM calculation in Ref. 12. The curve (---) is the fit obtained for an intersystem crossing rate constant of 2.8×10^8 s^{-1}. The curve (-.-) is the smooth curve for the triplet rate constants which interpolates all experimental data as in Fig. 7. (+) point is the triplet rate constant extracted from the analysis of PHOFEX spectra of $^1CH_2(0_{00})$.[14] The singlet threshold energy is marked with an arrow.

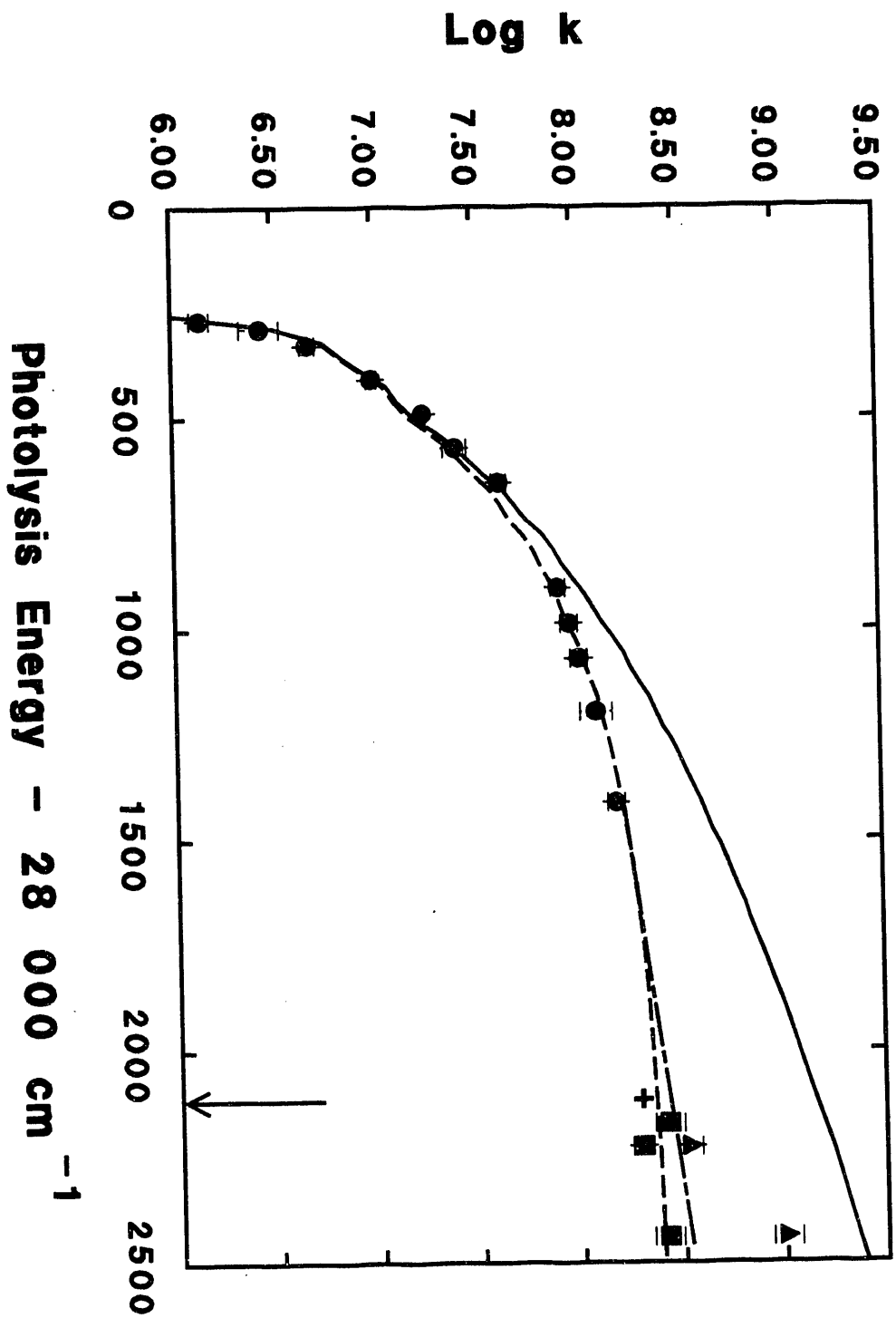
Log k
6.00
6.50
7.00
7.50
8.00
8.50
9.00
9.50
0
500
1000
1500
2000
2500
Photolysis Energy - 28 000 cm^{-1}

Figure 7. Energy dependence of the dissociation rate constants. The filled diamonds are the total rate constants measured in Ref. 18. The filled circles are the triplet rate constants calculated from the measured rates and branching ratios. The filled square is the triplet rate constant calculated from the PST or variational RRKM singlet rate constant at 56 cm^{-1} where both give the same result. Open triangles are singlet rate constants from the measured total rates and branching ratios. The curve (---) is the extrapolation of the triplet rate fit obtained for an k_{isc}= 2.8 x $10^{8}s^{-1}$. The curve (-.-) interpolates between the data of Fig. 6 (Ref. 11) and the data points(filled circles). The curve (...) is the PST singlet rate constant[17,18], and the solid curve represents variational RRKM calculation for the singlet rate constant.[17,18]

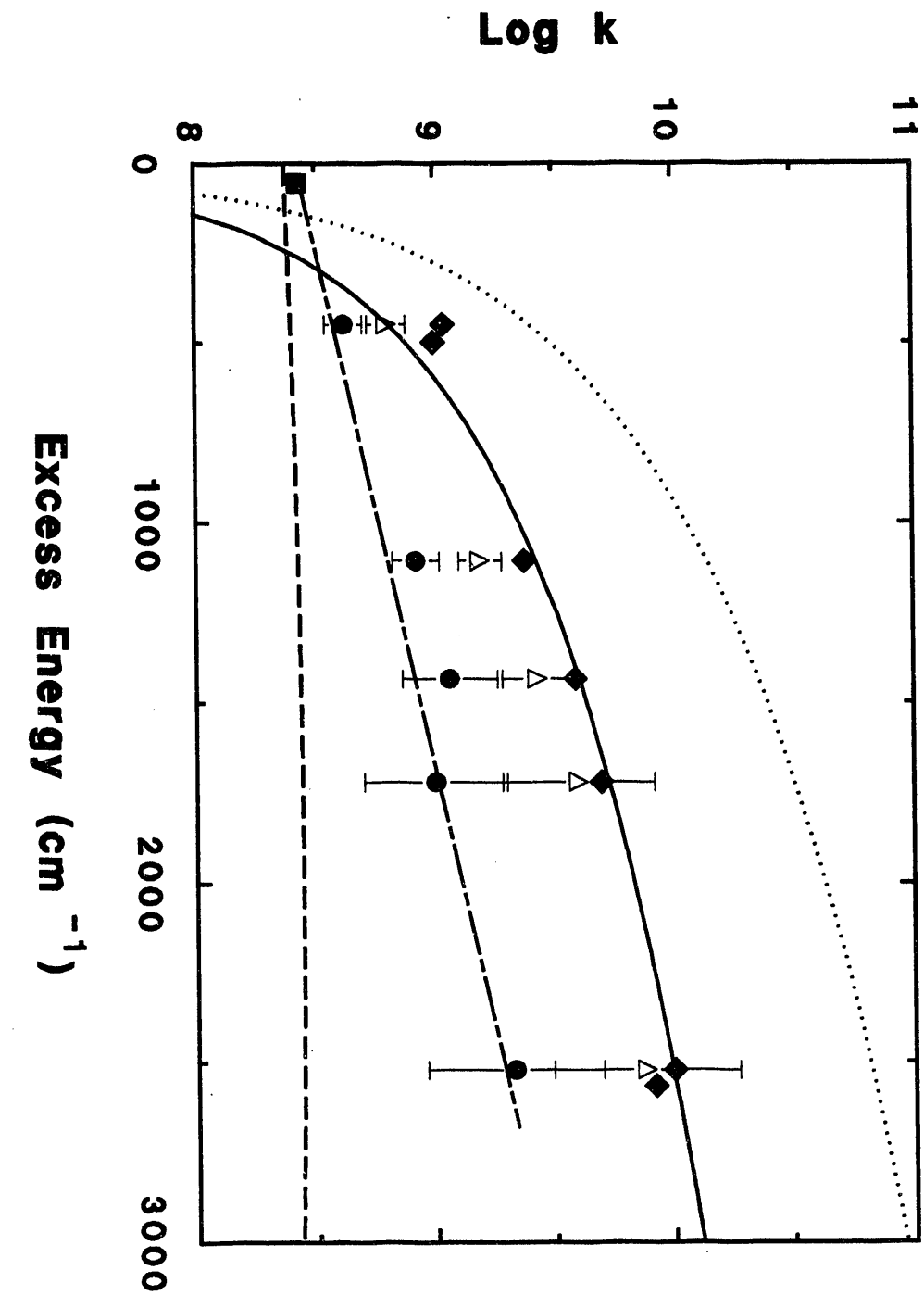
Log k
8
9
10
11
0
1000
2000
3000
Excess Energy (cm -1)

Part II

EXPERIMENTAL OBSERVATION OF VIBRATIONAL LEVEL THRESHOLDS OF THE QUANTIZED TRANSITION STATE IN THE PHOTODISSOCIATION OF KETENE

I. INTRODUCTION

The Rice, Ramsperger, Kassel, and Marcus (RRKM) theory, since its development in 1950's by R.A. Marcus, has been greatly successful in explaining the rates of a wide variety of chemical reactions such as thermal decomposition, collision-induced isomerization, and photoexcited reactions.[1] The RRKM theory is the quantum mechanical version of the standard classical transition state theory (TST) and developed for the rate of the unimolecular reaction. The RRKM theory is a statistical theory and based on assumptions that (i) the vibrational energy in the excited molecule is distributed statistically among the all vibrational degrees of freedom, (ii) the vibrational energy flows freely among the different degrees of freedom at a rate much faster than the reaction rate, and (iii) the rate of reaction is controlled by passage through the dynamical bottleneck separating the reactant from products on the potential energy surface (PES) for the reaction.

In the RRKM theory, the rate constant at total energy (E) and the total angular momentum (J) is given by

$$k(E,J) = \frac{N^{\ddagger}(E,J)}{h\rho(E,J)} \quad , \qquad (1)$$

where $N^{\ddagger}(E,J)$ is the number of energetically accessible vibrational states of transition state with energy less than E, $\rho(E,J)$ is the density of vibrational states of the

Zreactant, and h is Planck's constant.

Even though the RRKM theory has been nearly universally accepted for many decades, because of the lack of the knowledge about the potential energy surface in the vicinity of the transition state, the vibrational structure of the molecule at transition state has been estimated or simply fit to explain the experimental results. And also, due to the complicated nature of highly vibrationally excited reactant states, the density of reactant states in Eq.(1) has been estimated from data at much lower energies rather than measured directly. In this sense, the definitive test of RRKM theory has been difficult.

With the recent development of molecular beams and lasers, it is now possible to measure the rate constants for the reactants with well defined initial conditions. A molecular beam is used to minimize the internal thermal energy of the molecule in the ground state. The high-resolution lasers excite the molecule to well-defined reactant states and probe the quantum-state-resolved fragments. In addition, recent high level quantum mechanical calculations now provide quantitative predictions for the properties of transition states of small molecules.[2] Therefore, the RRKM theory has been subjected to more stringent tests. Using a variety of spectroscopic techniques such as overtone excitation, photon excitation followed by internal conversion, and stimulated excitation pumping (SE

kinetic studies for well-defined reactant states have been carried out for many unimolecular reactions.[3]

Recent measurements of state-specific rate constants have shown that the rate of unimolecular reaction is strongly dependent on the quantum mechanical character of initially prepared reactant state.[4-6] For unimolecular reactions without a reaction barrier, there has been recently a remarkable progress in both theories and experiments. For the barrierless reaction, the transition state is not well defined on the PES along the reaction coordinate, and many statistical theories such as prior theory, phase space theory (PST)[7], statistical adiabatic channel model (SACM)[8], separate statistical ensemble (SSE) model[9], and variational RRKM (var-RRKM) theory[10] have been developed to explain the kinetics and dynamics of barrierless unimolecular reactions. Among these theories, the var-RRKM theory is mainly developed for the rate of the reaction. The var-RRKM theory implements the concept of variational TST, and determines the location of the transition state by finding the minimum entropy on the PES along the reaction coordinate. The rate constants for the dissociation of NCNO and CH_2CO have been measured and quite well explained by var-RRKM theory.[11-13] But since the transition state for the barrierless reactions is quite loose, the reaction rate increases rapidly with increasing energy, and only the overall behavior of rate constants as a function of the energy could be compared with theory.

The transition state is defined on the potential energy surface along the reaction coordinate, and the bound vibrational motions of the molecule at the transition state are assumed to be decoupled from the reaction coordinate. The passage through the transition state is then vibrationally adiabatic, and the vibrational levels of the molecule at transition state represent reaction thresholds, that is, quantized channels connecting the reactant to products. The RRKM theory, as implicated in Eq.(1), predicts that the rate constant increases by steps with an amplitude equal to $1/[h\rho(E,J)]$ as the energy is increased through each vibrational state of the transition state. In this work, the steplike structures in rate constant have been observed for the first time in the unimolecular reaction of ketene. This is consistent with the fundamental idea of the transition state (RRKM) theory, and provides a strong test of the unimolecular reaction rate theory.

The three lowest electronic states of ketene are the ground singlet state (S_0), the first excited singlet state (S_1), and the first triplet state (T_1). The ketene molecule in the ground state is UV laser excited ($S_1 \leftarrow S_0$), internally converts and/or intersystem crosses, and dissociates into methylene and CO products (Figure 1). The ketene molecule dissociates into singlet methylene and CO fragments through the barrierless singlet potential energy surface with a threshold energy of 30,116 cm^{-1} (Figure 1).[14] The

photodissociation dynamics of CH_2CO on the singlet surface (singlet channel) has been recently extensively studied and the quantitative tests of various statistical theories have been carried out.[14-17] The threshold energy for the dissociation of ketene into triplet methylene and CO fragments (triplet channel) is lower than the threshold energy for the singlet channel, and there is a small barrier on the PES along the reaction coordinate. The measurements of CO fragment rotational distributions from triplet channel have shown that the release of the available energy into fragments is dynamically controlled by the vibrational structure of the molecule at the well-defined transition state.[18] In this work, the reaction rates for the triplet channel of ketene molecules which are initially prepared in the supersonic molecular jet are measured as a continuous function of the energy. The quantized transition state vibrational thresholds are revealed in clear steplike structures observed in rate constants.

II. EXPERIMENTAL METHODS

Ketene (CH_2CO) was prepared by passing acetic anhydride through a red-hot quartz tube, trapped at 77 K, and distilled from 179 K to 77 K twice before use. Deuterated ketene (CD_2CO) was prepared by the same method from deuterated acetic anhydride (Sigma, +99.0 % assay). The sample was stored at 77 K when it was not in use. For the experiment, ketene was kept at hexanes slush (179 K) where the vapor pressure of ketene is 50 torr. Helium carrier gas was bubbled through the sample and the gas mixture was expanded through the 0.5 mm diameter orifice of a pulsed nozzle into the vacuum chamber. The backing pressure of the carrier gas was 1.5 atmosphere and the background pressure in the vacuum chamber was maintained at 10^{-4} torr when the nozzle was on. Ketene was rotationally cooled by the supersonic expansion and the rotational temperature of ketene in the experiment was estimated to be about 3-5 K.[14]

A tunable UV laser source for the dissociation of ketene was obtained by frequency doubling of the dye laser output (Lambda Physik FL2002E; 0.2 cm^{-1} linewidth) pumped by the second harmonic output of Q-switched Nd:YAG laser (Spectra-Physics DCR-4). DCM, LDS698, and mixtures of those dyes in Methanol were used for the dye laser to generate 30-50 mJ/pulse of energy in the 680 nm - 720 nm range. The UV laser output was 6-10 mJ/pulse in the 360 nm - 340 nm region.

The laser pulse had 0.4 cm^{-1} of linewidth and 7 ns of time duration. The absolute frequency of the dye laser output was calibrated with an accuracy of ± 0.5 cm^{-1} using the optogalvanic spectrum of Ne gas. Direction and intensity of the UV laser output from KDP crystal were actively maintained and maximized, respectively, using Inrad Autotracker II during the scan of dye laser. The UV laser output was almost completely separated from the fundamental visible laser pulse through three reflections on UV dichroic mirrors before it entered the vacuum chamber.

A tunable vacuum UV (VUV) laser source was generated for the laser-induced fluorescence (LIF) detection of CO fragment using its rovibronic transitions in the ($A^1\Pi$ - $X^1\Sigma^+$) (v'=3 - v"=0) band. The output of the dye laser (Lambda Physik FL3002E; linewidth ≈ 0.2 cm^{-1} ; pulse length ≈ 7 ns; 15-20 mJ/pulse in the 430 nm - 450 nm range with Coumarin-440 dye in Methanol) pumped by third harmonic output of another Q-switched Nd:YAG laser (Continuum YG682-10) was frequency tripled through a Xe gas tripling cell to generate the VUV laser in the range of 143 nm - 150 nm. The efficiency of tripling is about 10^{-6}.[19] The fundamental dye laser output was focused into the center of 10 cm-long tripling cell filled with 20-40 torr of Xe gas by using a fused silica lens (f.l. = 7 cm). The generated VUV laser was collimated into the vacuum chamber by the CaF_2 lens (focal length = 8 cm) located at the exit of the tripling cell.

Pump and probe lasers were aligned to propagate colinearly from opposite ends of the vacuum chamber and cross the molecular beam pulse at 90°. The distance of the center of interaction region, which is defined by the overlap of lasers, from the nozzle orifice was 3-4 cm. The polarization of both laser pulses were parallel to the axis of jet expansion and perpendicular to the axis of fluorescence detection (*vide infra*). A small portion of the pump laser intensity was reflected from entrance window of the vacuum chamber before it crossed the molecular beam, detected by fast-response photodiode, and used for the normalization for pump laser intensity fluctuation. VUV probe laser passed the molecular beam, reflected from the exit window inside the vacuum chamber, attenuated by LiF diffuser, detected by solar blind VUV PMT (EMR 542G-08-19, LiF window) located at the perpendicular position to the direction of the laser beams, and used for normalization of VUV intensity fluctuation. The linearity of normalization was carefully checked.

The nozzle valve driver (Newport BV100) and two Nd:YAG lasers were triggered by the DG535 (SRS) pulse generator with 10 Hz repetition rate. The Nd:YAG laser for the photolysis laser was internally Q-switched. Scattered photolysis laser light was detected by the fast-response photodiode and the signal was used to trigger the boxcar (SR250 from SRS). The gate output of the boxcar which was delayed with respect to the trigger signal, amplified, and used to trigger the Q-

switch of the other Nd:YAG laser for generating delayed probe laser pulse. The delay between pump and probe lasers was varied by the delay function of the boxcar. Synchronization of the molecular beam pulse and the laser pulses was obtained by the internal delay function of the nozzle valve driver.

LIF of CO product was detected by a solar-blind VUV PMT (EMR 542G-09-19, MgF_2 window). It was placed so that the axis of fluorescence detection was perpendicular to the direction of the molecular beam expansion and the window of PMT was about 5 cm away from the interaction region (*vide supra*). A Cultured quartz window (Acton, 2" diameter) was used in front of the VUV PMT to reduce scattered VUV laser light. PMT signals were preamplified by 50 times using the dual amplifier (Hewlett-Packard, 8447D OPT 001), sampled and integrated by boxcar (SR250), digitized by A/D converter using DASH-8 (Metrabyte) board, and stored in the microcomputer (IBM PC/XT) using the data taking program.[20] Both pump and probe laser frequencies were controlled by the same computer.

Photofragment excitation (PHOFEX) spectra were obtained by monitoring the peak height of a specific rovibrational transition of the CO fragment while the photolysis laser frequency was scanned. The VUV probe laser frequency was fixed on a specific rovibrational transition of CO. The delay time between the pump and probe lasers was fixed with a time jitter less than 5 ns. PHOFEX curves were obtained

with 0.5-1 cm^{-1} resolution of the pump laser frequency. Each data point was averaged for 10-20 laser shots and PHOFEX curves were averaged for 3-5 scans.

Rate constants for photodissociation of ketene have been determined by measuring the appearance rates of CO fragment. The VUV probe laser frequency was fixed at a specific rovibrational transition of CO product and the CO LIF signal was monitored while scanning the delay time between pump and probe lasers at a fixed pump laser frequency. The delay time was scanned by SR265 software, which controls the delay between trigger signal and gate output of the boxcar via SR245 computer interface. Data acquisition was made by using the same software.

The CO product rise curves were obtained at photolysis energies where rate constants were in the 10^6 - $5x10^7$ s^{-1} range. Proper alignment of pump and probe lasers is the key for accurate measurement of rate constants. Before taking the CO rise curve at each photolysis energy, the validity of alignment was tested by taking the CO product rise curve at high photolysis energy where the lifetime of excited state is shorter than 50 ns. Flatness of CO LIF signal over long period of delay time after it reached the asymptotic level was evaluated and used to judge the proper set-up of experiment. Flatness up to 1.0 μs of delay time could be obtained with 20 mm^2 for the UV laser beam cross section. At the longer delay time, the UV excited ketene molecules start

to move out of the probing zone which is defined by the cross section of VUV probe laser beam (7-12 mm^2). For the measurement of slow reaction rates ($k(E) < 5 \times 10^6 s^{-1}$), the cross section of the pump laser beam was expanded by about four times using a telescope in order to compensate for the movement of the excited ketene molecule. Flatness up to 2.0 μs could be obtained. The diameter of expanded pump laser was about 1 cm in the interaction region, while that of the probe laser was 3-4 mm when it is assumed that diameter of blue visible fundamental laser is same as that of VUV laser beam. The probe laser was carefully aligned so that it overlapped with the portion of pump laser on the downstream side of the molecular beam pulse as shown in Figure 2. Because of the decrease in the pump laser energy density, the signal-to-noise (S/N) ratio went down and gave relatively large uncertainties for rate constants of slow reactions. Rate constant measurements down to $1.0 \times 10^6 s^{-1}$ were possible without any correction to the raw experimental data.

Each CO product rise curve was averaged over 15-20 scans and measured three times at each photolysis energy. Rate constant measurements were carried out as a function of photolysis energy with 2-4 cm^{-1} resolution. For checking reproducibility of data, each of three different measurements at the same photolysis energy was carried out in a different day with a new alignment of laser beams.

III. RESULTS

Similar types of experiments have been done for $CH_2CO \rightarrow CH_2(^3B_1) + CO(^1\Sigma^+)$ and $CD_2CO \rightarrow CD_2(^3B_1) + CO(^1\Sigma^+)$ reactions. Results are categorized into three different sections. In each section, results for both CH_2CO and CD_2CO will be presented. For convenience, "ketene" is used to refer both CH_2CO and CD_2CO.

A. CO PRODUCT ROTATIONAL DISTRIBUTIONS

The CO product rotational distributions have been obtained from rovibrationally resolved VUV LIF spectra for CO product by the same method as described in Ref. 18. The CO product rotational distributions from CH_2CO and CD_2CO obtained at the photolysis energies of 28,250 cm^{-1} and 28,410 cm^{-1} are shown in Figure 3 (a) and (b), respectively. The rotational distributions are Gaussian-shaped and peak at around J=12 for CH_2CO and J=11 for CD_2CO. The CO fragment acquires its angular momentum from the forces exerted as it passes through the exit valley of the potential energy surface. An impulsive force along the C-C bond at the transition state defined at the top of the reaction barrier models the observed distribution quite well.[18] The equilibrium structure and vibrational motions at the transition state are responsible for the peak position and width of the

distribution, respectively. This impulsive model using the *ab initio* transition state structure has been used for the calculation of CO product rotational distributions from the dissociation of CH_2CO and quite successful in explaining the distribution at photolysis energies near the reaction threshold region.[18] The solid lines in Figure 3 (a) and (b) are calculated CO rotational distributions using the same model as described in Ref. 18. The details of the impulsive model and calculation are discussed later.

B. RATE CONSTANTS (k(E))

The CO product rise curve is least-squares fit by a single exponential function.[21] The pulse widths of pump and probe lasers (7ns) are convoluted in the fitting for reaction faster than $5x10^7$ s^{-1} by the same method described in Ref. 21. For the measurements of rate constants less than 10^7 s^{-1}, the effect of the convolution of laser pulse widths is negligible compared to experimental error and has been neglected in the fitting process.[21] The standard deviation for the least-squares fit to an individual CO rise curve is much less than the difference between each of the three data points. These latter are used to estimate the uncertainty of measured rate constants.

When the CO fragment is probed at a long delay time after UV excitation, rotational to transnational energy

transfer might occur due to collisions because of the kinetic energies of the CO fragments. The collisional relaxation of CO product in the molecular beam has been tested by comparing the CO rise curves for low-J and high-J CO products. The CO rise curves for the Q(6) and Q(12) transitions from the CD_2CO dissociation at 28,900 cm^{-1} ($k \approx 3 \times 10^7$ s^{-1}) are shown in Figure 4 (a) and (b), respectively. The curve in Figure 4 (c) is the ratio of the CO population rise curve probing the Q(6) transition to that probing the Q(12) transition. Collisional relaxation from high J's to low J's has been clearly observed at around 2.5 μs delay time for the detection geometry employed in this work. This makes it impossible to measure lifetimes longer than 1.5 μs.

The CO product rise curves obtained by monitoring the LIF signal of the Q(12) transition of CO fragments from the CH_2CO and CD_2CO dissociations at photolysis energies of 28,423 and 28,500 cm^{-1} are shown in Figure 5 (a) and (b), respectively. The single exponential fits are shown as solid lines and give the rate constants of 1.0×10^7 s^{-1} and 3.6×10^6 s^{-1} for the CH_2CO and CD_2CO dissociations, respectively. The rate constants have been measured for LIF transitions probing different J states of CO such as Q(13) and Q(6) transitions and rate constants are found to be the same as those obtained by using the Q(12) transition within experimental error as demonstrated earlier by Chen and Moore.[21] In the threshold region of the photolysis energy,

the most probable angular momentum of CO product is around J=12 and the Q(12) transition is one of the well isolated peaks in LIF spectrum. Therefore, the Q(12) transition has been used for all rate constant measurements.

Rate constants as a function of the photolysis energy, k(E), are plotted in Figure 6 and Figure 7 for CH_2CO and CD_2CO, respectively. Each data point represents the average of three differently measured rate constants and error bars on selected data points are two times the estimated standard deviation of the mean of the three points from the true value, $[\Sigma^3_{i=1}((x_i-\overline{x})^2/6)]^{1/2}$. The threshold energy for the dissociation of CD_2CO is found to be about 55 cm^{-1} higher than that for CH_2CO due to the zero point energy difference (*vide infra*). Rate constants for the dissociation of CD_2CO are roughly four times smaller than those for CH_2CO, and rate constant measurement in the threshold region for CD_2CO dissociation turns out to be impossible with our apparatus for the reasons mentioned earlier. Distinct steps in k(E) associated with the first few transition state vibrational level thresholds are observed in the first 200-300 cm^{-1} region above the reaction thresholds for both isotopes. The structure becomes washed out rapidly at higher photolysis energy due to both the uncertainties of data and the increase in number of accessible transition state vibrational levels.

C. PHOTOFRAGMENT EXCITATION (PHOFEX) SPECTRA

Photofragment Excitation (PHOFEX) spectra probing the Q(12) transition of CO product from CH_2CO at 50 ns delay time and from CD_2CO at 200 ns delay time are shown in Figure 8 (a) and Figure 9 (a), respectively. The PHOFEX signal can be expressed as

$$S(E,v,J,\Delta t) \propto \sigma(E) * P(E,v,J) * [1 - \exp(-k(E)*\Delta t)] \quad (2)$$

where S is the intensity of LIF signal probing CO(v,J) product, $\sigma(E)$ is the absorption cross section of parent molecule, P(E,v,J) is the probability of CO fragment to be populated in the (v,J) quantum state, k(E) is the rate constant, and Δt is the reaction time which corresponds to the delay time between the pump and probe lasers. For a short delay time, the pulse widths of lasers are to be considered.

The absorption spectrum of CH_2CO at room temperature is a diffuse structureless band for the $S_1 \leftarrow S_0$ transition.[22] Presumably this is the result of fast internal conversion. The analysis of singlet CH_2 PHOFEX spectra shows that $\sigma(E)$ is nearly constant over 100 cm^{-1} ranges of photolysis energy.[14] The simulated PHOFEX curves using directly measured k(E) data in Eq. (2) for a constant $\sigma(E)$ and P(E,v,J) are compared with the experimental PHOFEX curves in Figure 8 (b) and Figure 9

(b) for CH_2CO and CD_2CO, respectively. Great similarity has been found for both isotopes in the first 200 - 300 cm^{-1} region above the reaction thresholds. Positions and amplitudes of steps in PHOFEX curves are quite well reproduced by $[1-\exp(-k(E)*\Delta t)]$. This confirms that the structures observed in k(E) are real and implies that it is a good approximation that the $\sigma(E)*P(E,v,J)$ term is nearly constant over this small range of energy just above threshold. Highly resolved fine structures in PHOFEX curves are therefore most likely to be associated with the structures in k(E).

At higher photolysis energy, over 28,500 cm^{-1} for CH_2CO, the simulated PHOFEX signal is still increasing with increasing energy while the experimental curve starts to level off. This deviation comes from the neglect of the $\sigma(E)*P(E,v,J)$ term in the calculation of simulated PHOFEX curve. A more striking deviation is observed in the PHOFEX curve for the Q(2) transition probing CO (v=0,J=2) product from CH_2CO, which is shown in Figure 8 (c). The overall shape of the curve is quite different from that for CO (v=0,J=12) product while the reaction times are the same for both PHOFEX curves. In the CO(v=0,J=2) PHOFEX curve a sharp peak is observed at around 28,500 cm^{-1} of photolysis energy, where the CO(v=0,J=12) PHOFEX curve starts to level off. It means that a noticeable change in product rotational distribution occurs at around 28,500 cm^{-1} of photolysis energy. The width of the

CO rotational distribution is determined by the characteristic vibrational motion of a molecule at the transition state.[18] Therefore, the comparison of PHOFEX curves for CO product with different J's gives another unique way to observe vibrational thresholds of transition state. The PHOFEX spectrum probing CO(v=0,J=2) from the dissociation of CD_2CO is given in Figure 9 (c). It shows more steps and peaks at even high photolysis energies where the structures in both k(E) and the CO(v=0, J=12) PHOFEX curve become washed out, revealing more vibrational thresholds of the transition state. The quantitative analysis of PHOFEX in terms of the change of CO product rotational distribution as a function of the total available energy will be made based on the impulsive model in the following.

IV. ANALYSIS and DISCUSSION

The observation of structures in k(E) is consistent with one of the fundamental ideas of transition state theory (RRKM theory), that the reaction probability is controlled by flux through quantized thresholds of the transition state. Therefore, the obvious first step in analysis is to carry out RRKM calculations for comparison to the experimental results.

This section will be presented by the following order. (1) Coupling of three lowest electronic states (S_1, S_0, T_1) in the UV excited ketene will be considered for the observed rate constant expression. (2) General equations for RRKM calculation including rotational levels and one-dimensional tunneling will be introduced. (3) Symmetry selection rules involved in the photodissociation of ketene will be discussed under different assumptions for rotation-vibration coupling in highly vibrationally excited reactant. (4) Model calculation for hindered rotor energy levels of ketene at transition state will be carried out based on *ab intio* transition-state structure.[23] (5) Reaction barrier and imaginary frequency related to the width of barrier will be calculated by RRKM fits for k(E) data in the reaction threshold region. (6) Assignment for C-C-O bending mode of ketene at transition state will be tried through the analysis of PHOFEX curves for different J's of CO fragment. (7) Based on the arguments in (1)-(6), RRKM calculations will be

compared with experimental results.

A. Coupling of Electronic States

UV photolysis pulses (0.4 cm^{-1} linewidth; 7 ns pulse width) excite a set of eigenstates of the form

$$|\Psi_n\rangle = \sum_i \alpha_{ni} |S_{1i}\rangle + \sum_j \beta_{nj} |S_{0j}\rangle + \sum_k \gamma_{nk} |T_{0k}\rangle \quad . \qquad (3)$$

Eigenstates with the most S_1 character are preferentially excited by the laser pulse, since only S_1 states carry significant oscillator strength. Ketene undergoes internal conversion ($S_0 \leftarrow S_1$) and/or intersystem crossing ($T_1 \leftarrow S_1, S_0$) on a time scale shorter than the UV pulse and the time for unimolecular dissociation on S_0 or T_1 surface, Figure 1. Nonradiative decay rates of S_1 states are uncertain at present time and roughly estimated to be in the wide range of $2.5 \times 10^9 - 4 \times 10^{13}$ s^{-1}.[14,24,25] The internal conversion rate constant for CH_2CO is shown to be greater than 10^9 s^{-1} at the singlet threshold (30,116.2 ± 0.4 cm^{-1}).[14] This rate is not expected to change much as photolysis energy decreases to 28,200 - 29,000 cm^{-1}. The measured rate constants in this work are much less than 10^9 s^{-1}, and it is a good assumption that the dissociation of ketene on the triplet surface occurs through the strong coupling of T_1 states to the statistical mixture

of S_1 and S_0 states. Photolysis energies used in the present work are much below the singlet threshold and only dissociation on the triplet surface is possible. With the approximation that any pure T_1 state within a narrow energy range would have a decay rate, k_T, the dissociation rate constant for a particular ketene eigenstate can be expressed by

$$k_n = k_T \sum_j |\gamma_{nj}|^2 \quad . \tag{4}$$

(i) For the case of strong coupling of all three electronic states, both the internal conversion and intersystem crossing are much faster than the decay rate of the T_1 states (k_T). Thus the excited state is the statistical mixture of S_1, S_0, and T_1 states, and the statistical weights are proportional to the density of vibrational states of each electronic state. That is,

$$\sum_i |\alpha_{ni}|^2 \approx \frac{\rho(S_1)}{\rho_{total}} \quad , \quad \sum_j |\beta_{nj}|^2 \approx \frac{\rho(S_0)}{\rho_{total}} \quad , \quad \sum_k |\gamma_{nk}|^2 \approx \frac{\rho(T_1)}{\rho_{total}} \tag{5}$$

where $\rho(S_1)$, $\rho(S_0)$, and $\rho(T_1)$ are densities of states on the S_1, S_0, and T_1 states, respectively. The sum of the densities of states, ρ_{total}, is dominated by $\rho(S_0)$. The rate of formation of CO fragment for the triplet channel of ketene dissociation, k_t, from Eq. (1), can be expressed by

$$k_t \approx k_T \frac{\rho(T_1)}{\rho_{total}} \quad , \tag{6}$$

where $k_T = N^{\ddagger}/[h\rho(T_1)]$ ($N^{\ddagger}$ is the number of energetically accessible states of transition state). Therefore, the dissociation rate of ketene on the triplet surface, k_t, which is equivalent to the appearance rate of the fragment is given by

$$k_t = \frac{N^*}{h\rho_{total}} \quad . \tag{7}$$

(ii) For the case of weak coupling of T_1 states to S_1 and S_0 states which are strongly coupled to each other, the initially excited state can be described as a statistical mixture of S_1 and S_0 states and it has mostly S_0 character because of the dominant density of states of S_0 over that of S_1. The following kinetic scheme is very useful.[21]

$$N^* \underset{k'_{isc}}{\overset{k_{isc}}{\rightleftharpoons}} T_1 \xrightarrow{k_T} CH_2(^3B_1) + CO \tag{8}$$

N^* is the initial state of ketene which has mostly S_0 character. Solution of rate equations set by the above kinetic scheme gives the rate of the product formation as follows:[21]

$$[\,P\,] = A\,[1 - \exp(-k_t t)]\ , \tag{9}$$

$$k_t = \frac{k_{isc} k_T}{(k_{isc'} + k_T)}\ . \tag{10}$$

From the Golden rule, $k_{isc}'/k_{isc} \approx \rho(S_0)/\rho(T_1)$ and $k_T = N^{\ddagger}(E)/[h\rho(T_1)]$, thus the observed rate constant can be rewritten by

$$k_t = \frac{N^*}{h\rho(S_0) + \frac{N^*}{k_{isc}}}\ . \tag{11}$$

Taking the reverse, it becomes

$$\frac{1}{k_t} = \frac{1}{k_0} + \frac{1}{k_{isc}}\ , \tag{12}$$

where $k_0 = N^{\ddagger}/[h\rho(S_0)]$. Therefore, the observed rate constant is equivalent to k_0 when $k_{isc} \gg k_0$, and the rate of the product formation will be limited by the intersystem crossing rate when $k_0 \gg k_{isc}$.

Rate constants for the dissociation of CH_2CO on the triplet surface have been measured in the 28,289 - 29,412 cm^{-1} range of the photolysis energy by Chen and Moore.[21] The RRKM calculation for k_0 using *ab initio* values for vibrational frequencies of transition states predicts 3-5 times higher rate constants than experimental results at photolysis energies higher than 29,000 cm^{-1}. The fit to the experimental

rate constants using Eq. (12) gives the lower bound for intersystem crossing rate, $k_{isc} \approx 2 \times 10^8$ s^{-1} at 30,000 cm^{-1}.[21] But this deviation of the experiment from the RRKM calculation could result from the movement of the transition state along the reaction coordinate as energy increases. That is, as energy increases above the adiabatic vibrational thresholds, the transition state moves in along the reaction coordinate, and therefore the transition state gets tighter to give the slower reaction at high energy. Direct measurement of rate constants and singlet/triplet branching ratios at photolysis energies above the singlet threshold has allowed the direct measurement of k_t at even higher energies than the singlet threshold.[12,16] It has been found that the dissociation rate of CH_2CO on the triplet surface, k_t, is 4.0 (± 0.7) $\times 10^8$ s^{-1} at 30,566 cm^{-1} of the photolysis energy and increases slowly with increasing energy.[16] The measured rate constants in the present work can be expressed by k_0. This is specially true in the first 500 cm^{-1} range above the reaction threshold, where the rate of the reaction is slow ($k < 3 \times 10^7$ s^{-1}).

For both strong and weak coupling cases, the rate constant for the formation of product on the triplet surface in the threshold region, where k_t is lower than 5×10^7 s^{-1}, is expected to be predicted by Eq. (7). For deuterated ketene this is more true because the rate of product formation, k_t, is slower while the internal conversion or intersystem

crossing rate are expected to be faster due to the increase of the density of vibrational states in S_0 and T_1 states.

B. General Equations for RRKM calculation

The RRKM calculation for rate constant of unimolecular reaction of ketene considering rotational energy levels and one-dimensional tunneling along the reaction coordinate can be expressed by the following formula for the case of complete K-mixing (K = -J to J).[26]

$$k(E,J) = \frac{\sum_{K^*=-N}^{N} \sum_{n} P(E - \epsilon^*_{n,N,K^*})}{\sum_{K=-J}^{J} h\rho(E - W_{J,K})} \qquad (13)$$

$$\epsilon^*_{n,N,K^*} = V_0 + W^*_{N,K^*} + \sum_{i=1}^{s-1} h\nu^*_i (n_i + \frac{1}{2}) \qquad (14)$$

$$W^*_{N,K^*} = \frac{1}{2}(B^*+C^*)[N(N+1) - K^{*2}] + A^*K^{*2} \qquad (15)$$

$$W_{J,K} = \frac{1}{2}(B+C)[J(J+1) - K^2] + AK^2 \qquad (16)$$

E is the total energy which is the sum of the photolysis energy and thermal energy of the parent molecule in the pulsed molecular jet. J is the angular momentum of the excited state of ketene. N is the rotational angular

momentum of ketene at the transition state on the T_1 surface. V_0 is the reaction barrier relative to reactants, which is the difference between zero-point energies of reactant in the ground state (S_0) and transition state in T_1 state. The number of vibrational degrees of freedom of the stable molecule, s, is 9 for ketene and n represents the set of vibrational quantum numbers for the transition state. Ketene in the ground state is near-prolate asymmetric top (κ= -0.997).[27] The symmetric top approximation is used for the calculation of rotational energy levels for both reactants and transition state. The K and K‡ in the symmetric top approximation (K_a and K_a‡ in the asymmetric top expression) are the projections of the rotational angular momentum, N (J = N + S in Hund's case (b) for triplet state), on the molecule-fixed a axis for the molecule in the excited reactant state and the transition state, respectively.

Nuclear spin conservation may restrict accessible K and K‡ quantum numbers for different initial nuclear spin states of ketene molecule in the ground state. Rotational constants of UV excited ketene molecules are assumed to be same as those (A,B,C) in the ground state. A‡, B‡, and C‡ are rotational constants of ketene at transition state and calculated from *ab initio* transition state structure,[23] giving A‡ = 2.50 cm^{-1}, B‡ = 0.268 cm^{-1}, and C‡ = 0.242 cm^{-1} for CH_2CO. In the RRKM calculation, rotational constants for transition state are modified due to the strong coupling of the

torsional mode and the overall rotation of the molecule (*vide infra*).

$P(E_1)$ is the transmission probability for each quantized reaction threshold of the transition state calculated for one-dimensional tunneling along the reaction coordinate. When the inverted parabolic function is assumed for the shape of the exit barrier along the reaction coordinate, $P(E_1)$ is given by

$$P(E_1) = \frac{e^{\epsilon}}{1 + e^{\epsilon}} \tag{17}$$

$$\epsilon = \frac{2\pi E_1}{h\nu_i} , \tag{18}$$

where ν_i is the imaginary frequency related to the width of the exit barrier.[27,28]

The generalized Eckart potential function has known to provide a more accurate representation of the barrier.[28,29] When Eckart potential function is used for the shape of the exit barrier, $P(E_1)$ is expressed by[26]

$$P(E_1) = \frac{\sinh(a)\ \sinh(b)}{\sinh^2(\frac{a+b}{2}) + \cosh^2(c)} , \tag{19}$$

where

$$a = \frac{4\pi}{h\nu_i} \sqrt{(E_1+V_0)}\ \frac{\sqrt{V_0 V_1}}{\sqrt{V_0} + \sqrt{V_1}} , \tag{20}$$

$$b = \frac{4\pi}{h\nu_i}\sqrt{(E_1+V_1)}\ \frac{\sqrt{V_0V_1}}{\sqrt{V_0}+\sqrt{V_1}}\ , \qquad (21)$$

$$c = 2\pi\sqrt{\frac{V_0V_1}{h\nu_i} - \frac{1}{16}}\ . \qquad (22)$$

V_0 is, as before, the barrier height relative to reactants and V_1 is the barrier height relative to products. RRKM calculations using either Eq. (17) or Eq. (19) as the transmission probability produce about the same results.[21] Only the Eq. (19) is used for the RRKM calculation.

The density of reactant states, $\rho(E)$, has been often estimated by harmonic state count which can be accurately calculated by Whitten-Rabinovitch (WR) approximation.[30] The density of reactant states by WR approximation, $\rho_{WR}(E,J=0)$, is given by

$$\rho_{WR}(E,J=0) = \frac{(E+E_{zp})^{s-1}}{(s-1)!\ \prod_{i=1}^{s}\nu_i}\ , \qquad (23)$$

where E_{zp} is the zero-point energy of ketene molecule and ν_i is the i-th fundamental vibrational frequency of ketene. Fundamental vibrational frequencies obtained from IR spectroscopic study of ketene are used.[31] Because of the anharmonicity of vibrational frequencies, actual $\rho(E,J)$ is expected to be higher than the WR approximation. Recent

spectroscopic studies have shown that the actual density of states for a number of molecules is significantly higher than predicted by harmonic counts.[5,6,32,33] For example, direct count of states from the stimulated emission pumping (SEP) spectroscopy of HFCO has shown that the actual density of states for vibrationally excited state of HFCO at 16,000 cm^{-1} is about four times higher than calculated by anharmonic direct counting.[6] Stark level-crossing spectroscopic study of D_2CO by Polik et al. has demonstrated that the experimentally measured density of states for vibrationally excited state of D_2CO in S_0 state at the energy of 30,000 cm^{-1} is about 10 or 6 times higher than harmonic or anharmonic state counts, respectively.[5]

The experimentally obtained CO (v,J) product rise curve is the sum of CO product rise curves for different initial quantum states of ground state ketene. With the approximation that individual CO rise curve follows a single exponential behavior, the experimentally observed CO product rise curve can be expressed by

$$M(t) = A \sum_m P_m (1 - e^{-k_m t}) \approx A (1 - e^{-k_{ob} t}) , \qquad (24)$$

that is,

$$e^{-k_{ob} t} \approx \sum_m P_m e^{-k_m t} , \qquad (25)$$

where M(t) is the population of the product as a function of

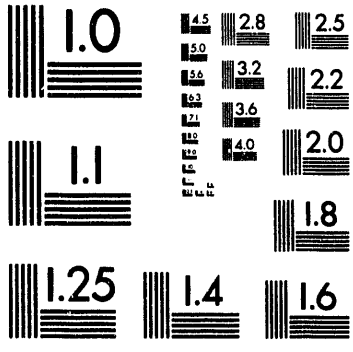
1.0
1.1
1.25
1.4
1.6
1.8
2.0
2.2
2.5
2.8
3.2
3.6
4.0
4.5
5.0
5.6
6.3
7.1

2 of 3

the reaction time, A is an arbitrary constant, k_{ob} is the measured rate constant determined from a single exponential fit to experimental CO product rise curve, m represents initial quantum state, P_m is the normalized relative population of molecule in m state, and k_m is the rate constant for initial m state. If both sides of Eq. (25) are integrated over the time from 0 to ∞, Eq. (25) becomes

$$\frac{1}{k_{ob}} = \sum_m \frac{P_m}{k_m}. \qquad (26)$$

The observed rate constant, k_{ob}, is the mean reaction time rate constant, and this has been found to give the accurate value for true averaged rate constant.[13,34]

C. Symmetry Selection Rules

In the absence of external fields, there are certain quantities that are conserved throughout the dissociation. For example, total energy (E) and the total angular momentum (F, M_F) are conserved. Neglecting the extremely weak interaction, parity with respect to inversion (Π) is also conserved. Another important factor to be conserved in the dissociation is the symmetry of the total eigenfunction. Therefore, the RRKM rate constant in Eq. (1) can be rewritten as

$$k(E,F,\Pi,\Gamma) = \frac{N^*(E,F,\Pi,\Gamma)}{h\,\rho(E,F,\Pi,\Gamma)} \quad , \qquad (27)$$

where Γ represents the symmetry class of the total wavefunction for the eigenstate. The importance of including symmetry factors in rate constant calculation has been emphasized for a number of years.[35] The strong dependence of rate constant on the vibrational symmetry in the photodissociation of formaldehyde has been predicted by Miller.[36] Recent state-specific rate constant measurements using the SEP technique for HFCO dissociation has shown that dissociation rates can be strongly dependent on vibrational symmetry of reactant states in the tunneling region.[6]

On the short time scale of photodissociation, the nuclear spin quantum number (I,M_I) is also expected to be conserved. The conservation of nuclear spin quantum number in the photodissociation of ketene has been demonstrated in recent studies of PHOFEX spectra for $^1CH_2$ (J_{KaKb}) fragment in the singlet threshold region by Green, Chen, and Moore.[14] They found that threshold energies for $^1CH_2$ fragments in ortho states ($I=1$; K_a+K_c = odd) are $\approx$ 9.7 cm^{-1} lower than the sum of the singlet threshold energy (30,116.2 $\pm$ 0.4 cm^{-1}) and the rotational energy term values of probed $^1CH_2$ fragments, while those for $^1CH_2$ fragments in para state ($I=0$; K_a+K_c = even) are exactly the same as the sum of the singlet threshold energy and their rotational energies. The ortho states of ketene ($I=1$; $K_a=1$) in the ground state lie about 9.7 cm^{-1} higher than

the para states (I=0; K_a=0). This means that $^1CH_2$ fragments in ortho (para) states originate exclusively from ortho (para) states of ketene. An upper limit for the nuclear spin conversion in the singlet photodissociation has been set at 1.7 %.[14]

The photodissociation of ketene on the triplet surface involves UV optical excitation ($S_1 \leftarrow S_0$), internal conversion ($S_0 \leftrightarrow S_1$), and intersystem crossing ($T_1 \leftrightarrow S_0, S_1$) processes. Selection rules for angular momentum quantum numbers and symmetries for many degrees of freedom in each process are different, and need to be considered for each case.

Ketene molecule in both ground and excited states is a slightly asymmetric prolate top. The molecular a,b,c axes are chosen to be z,y,x axes in body fixed coordinates, respectively, according to I^1 representation, Figure 10. The projection of rotational angular momentum on "a" axis, $|K|$, is a nearly good quantum number for ketene. Selection rules for a nearly good quantum number, K, will be considered in the following sections. Photodissociation of ketene on the triplet surface may occur in C_s^{II} (in-plane bent) or C_s^{I} (out-of-plane bent) transition states. The C_s^{I} transition state is a supertransition state for the interconversion of two equivalent C_s^{II} transition states. Distinct steps in k(E) are observed in the reaction threshold region where only C_s^{II} transition state is energetically accessible. Symmetry selection rules for only the C_s^{II} transition state will be

considered. Symmetry species of all degrees of freedom for ketene molecule in all electronic states will be classified in C_{2v} molecular symmetry (MS) group which is isomorphic with the appropriate CNPI group. This is a reasonable assumption at the photolysis energy used in this work considering the torsional motion and/or tunneling of strongly bent ketene molecules in excited states over the bending potential barrier at highly vibrationally excited states ($E_{vib} \approx 10^4$ cm^{-1} for S_1 and T_1 states).[23] At the transition state, two equivalent bent molecules interconvert by the torsional motion with a small barrier (1.25 kcal/mol CISD calculation) and C_{2v} symmetry classes are applied. When it is the case that C_{2v} (MS) group is reduced to C_s (MS) group, the correlation of symmetry classes between two MS groups needs to be done. Symmetry selection rules for the dissociation of CH_2CO will be presented. The extension to CD_2CO is straight forward. Different nuclear spin statistics for CH_2CO and CD_2CO will be described.

(i) UV excitation ($S_1 \leftarrow S_0$)

The optical transition from $S_0(^1A_1)$ to $S_1(^1A_2)$ state is electronically forbidden and vibronically allowed for electric dipole radiation. From A_1 vibronic symmetry in the S_0 ground state, A-type, parallel transition gives rise to a_2 vibrational states in S_1. B-type and C-type, perpendicular

transitions excite b_1 and b_2 vibrational states, respectively. The selection rules for total angular momentum and parity are

$$\Delta F = 0 \ (F \neq 0), \ \pm 1; \ + \leftrightarrow - \ . \tag{28}$$

The nuclear spin quantum number is conserved and the selection rules become

$$\Delta J = 0 \ (J \neq 0), \ \pm 1; \ \Delta I = 0; \ + \leftrightarrow - . \tag{29}$$

The selection rules for the K quantum number in the symmetric top approximation are

$$\Delta K = 0 \ (\text{A-type,parallel}); \quad \Delta K = \pm 1 \ (\text{B-,C-types,perpendicular}). \tag{30}$$

The population of (J',K') in S_1 state is determined by the product of Hönl-London factor and the initial population of (J,K) states of ketene molecule in the ground state prepared in the supersonic jet. Nuclear spin is found not to be cooled down in the molecular jet. Initial (J,K) states of ketene are othrewise populated according to a Boltzman distribution for a rotational temperature of 3 - 5 K.

(ii) Internal Conversion ($S_0 \leftarrow S_1$)

Internal conversion from A_1, B_2, and B_1 vibronic symmetries in S_1 state gives rise to a_1, b_2, and b_1 vibrational states in S_0 state with the selection rules,

$$\Delta J = 0;\ \Delta I = 0;\ \Delta K = 0;\ + \leftrightarrow +,\ - \leftrightarrow - \ . \qquad (31)$$

The S_0 state is highly vibrationally excited and strong anharmonic coupling should be expected. Also, strong Coriolis coupling may mix the vibrational states with different symmetry classes. In the strong vibration-rotation coupling case, K is not expected to be a nearly good quantum number any more. In the extreme case, K may be completely mixed and have values from -J to J. Stark level-crossing spectroscopic study for deuterated formaldehyde has shown that K in highly vibrationally excited states in the S_0 state of D_2CO may be conserved at the low J's accessed in the molecular jet.[5,37] Due to the lack of spectroscopic information for highly vibrationally excited states of ketene, the extent of the coupling is not certain at the present time. Since only K = 0,1 states are significantly populated in the ketene molecule in the supersonic jet while J is populated up to 7, the extent of K-mixing in highly vibrationally excited states is very important in assignment of rovibrational thresholds of transition states. Two limiting cases for K-mixing will be discussed later in this paper.

(iii) Intersystem crossing ($T_1 \leftarrow S_0$, S_1)

When the electron spin-orbit coupling is strong, the triplet electronic state is split into three different electronic electron-spin states. Two electron spins in triplet state give the symmetry classes, $\Gamma_{espin} = A_2 \oplus B_1 \oplus B_2$ in C_{2v} group. This combines with the symmetry of electronic wavefunction, $\Gamma_e = A_2$ in T_1 state, to give the symmetries of electronic electron-spin states, $\Gamma_{es} = A_1 \oplus B_2 \oplus B_1$. In this case, the symmetry selection rules for intersystem crossing might be determined by the symmetry of the product of the electron-spin and electronic wavefunctions, Γ_{es}. When this is the case, the spin-orbit matrix element for the coupling between $^1A_2$ (S_1) and $^3A_2$ (T_1) states vanishes, and only second-order or higher-order singlet-triplet interaction is possible.[38] On the other hand, first-order spin-orbit coupling is allowed between $^1A_1$ (S_0) and $^3A_2$ (T_1). Hence intersystem crossing might be favorable between S_0 and T_1 states. If the vibronic couplings of the electronic states are not strong, the direct intersystem spin-orbit coupling could be allowed only through one of the three electronic electron-spin states of T_1 states. In this case, only a_1, b_2, and b_1 vibrational states in T_1 are strongly accessible, since a_2 vibrational states are symmetry forbidden in S_0 state (*vide supra*). This means that a_2 vibrational states are only weakly accessible in T_1 state. In this case, the selection rules are

obtained by the conservation of the rovibrational symmetries of the two electronic states, and given by, using the notation in Hund's case (b),

$$\Delta J = 0;\ \Delta N = 0, \pm 1;\ \Delta K = 0;\ + \leftrightarrow +,\ - \leftrightarrow - \ . \qquad (32)$$

In the case of strong vibronic coupling, symmetry selection rules are loosened, and vibrational states with all symmetry classes in T_1 state are allowed. In this case, the intersystem crossing through the spin-orbit vibronic coupling or the spin-orbit rotational coupling is possible, and the selection rules become [38]

$$\Delta J = 0;\ \Delta N = 0, \pm 1;\ \Delta K = 0, \pm 2, \text{ or } \Delta K = \pm 1. \qquad (33)$$

(iv) Nuclear Spin Statistics

Nuclear spin statistical weights for ketene are determined by the symmetry of the nuclear spin wavefunctions. In CH_2CO, hydrogen atoms have a nuclear spin of ½. Four nuclear spin wavefunctions generate the representation, $\Gamma_{ns} = 3A_1 \oplus B_2$ in C_{2v} (MS) group, where three A_1 states correspond to I=1 (ortho) nuclear spin states and one B_2 state is I=0 (para) state. Since hydrogen nuclei are fermions, the total symmetry, Γ_{total} should be either B_1 or B_2. Therefore, since the vibronic symmetry of CH_2CO in the ground state is A_1, only

b_1 (K_a=odd, K_c=even) or b_2 (K_a=odd, K_c=odd) rotational states can combine with ortho (I=1) states while a_1 (K_a=even, K_c=even) or a_2 (K_a=even, K_c=odd) rotational states combine with para (I=0) state.

For the case of CD_2CO, deuterons have a spin of 1 and each deuteron can have three different nuclear spin wavefunctions. Hence nine nuclear spin wavefunctions are generated for CD_2CO and give the representation, $\Gamma_{ns} = 6A_1 \oplus 3B_2$, where five A_1 states correspond to the quintet (I=2) functions, one A_1 state is the singlet (I=0) function, and three B_2 states are the triplet (I=1) functions. Since deuterons are bosons, the total symmetry should be A_1 or A_2. Therefore, in the ground state CD_2CO (A_1 vibronic symmetry), only a_1 (K_a=even, K_c=even) or a_2 (K_a=even, K_c=odd) rotational states combine with ortho (I=2,0) states, while b_1 (K_a=odd, K_c=odd) or b_2 (K_a=odd, K_c=even) rotational states can combine with para (I=1) states. Interestingly, for CD_2CO, the ortho (I=0,2) states combine with K=even and the para (I=1) states combine with K=odd, which is opposite to the case for CH_2CO where K=odd is ortho (I=1) states and K=even is para (I=0) state. Nuclear spin statistical weights for CH_2CO molecule are "3" for ortho and "1" for para, while for CD_2CO they are "6" for ortho and "3" for para.

It should be noted that the nuclear spin statistical weights for rotational states are dependent on the symmetry of vibronic state. This is specially important for the

molecule at the transition state, where the thresholds for rovibrational energy levels of transition state can be observable.

D. Hindered Internal Rotation of ketene at the Transition state

Distinct steps in k(E) for the dissociation of ketene are observed in the first 200 - 300 cm^{-1} region above the reaction threshold. The *ab initio* (DZP CISD) values for vibrational frequencies of C_s^{II} transition state have been scaled by multiplying the ratio of the experimental values to the *ab initio* values for vibrational frequencies of the ground state ketene. The scaled *ab initio* vibrational frequencies are 154 cm^{-1} for H-C-C-O torsion, 252 cm^{-1} for C-C-O bending, and 366 cm^{-1} for CH_2 wag, as listed in Table I.[23] The spacings in the energies between the first two distinct steps in k(E) are around 100 cm^{-1} for CH_2CO and around 80 cm^{-1} for CD_2CO (Figure 6 and 7), and these steps are most likely to be associated with the lowest vibrational frequency mode, H(D)-C-C-O torsion, of ketene at the transition state.

The observed vibrational frequency for the H-C-C-O torsional mode seems to be about 50 % less than scaled *ab initio* values for CH_2CO transition state. This means that the actual transition state is looser in the torsional motion

than predicted by *ab initio* calculation. The H(D)-C-C-O torsional motion of the molecule can be treated as the hindered internal rotation with a small barrier. The *ab initio* values for the barrier to internal rotation are 1.25 (CISD) or 1.10 (CIDVD) kcal/mol.[23] In order to explain experimental results, model calculations for hindered internal rotation of ketene at transition state are carried out. The *ab initio* C_s^{II} transition state structure is used for the evaluation of moments of inertia for both CH_2CO and CD_2CO (Figure 10). The *ab initio* C_s^{I} transition state structure gives about the same values for moments of inertia. The barrier to internal rotation is varied to give the reasonable values close to the observed vibrational energies of ketene at transition state.

The torsional motion can be described as the relative internal rotation of CH_2 (CD_2) and CO groups about the symmetric axis. For convenience, the methylene group which has a symmetry axis is called the "top", and the CO group which does not have a symmetry is called the "frame". The origin of the potential barrier for the hindered internal rotation is not clearly understood, and a periodic sinusoidal potential function has been often used.[39] The potential energy for the two-fold symmetry can be expanded in a cosine series as

$$V(\theta) = \frac{V_0}{2}\,(1 - \cos(2\theta)) + \frac{V_1}{2}\,(1 - \cos(4\theta)) + \bullet\bullet \qquad (34)$$

where V_0 is the barrier height, V_1 changes the shape of the potential function, and θ is the relative angle between the two parts of the molecule. The effect of the parameter V_1 on the shape of the potential function is shown in Figure 11. The moment of inertia of the symmetric top about the C-C bond, I_{top}, is 1.88 amu*Å^2 while that of the frame, I_{frame}, is 16.9 amu*Å^2. In this case, when $I_{frame} > I_{top}$, the principal axes method (PAM), which uses the set of principal axes of the whole molecule as the coordinate system is useful.[40]

For an asymmetric top with a single two-fold internal rotor, the Hamiltonian can be written as[41,42]

$$\mathbf{H} = \mathbf{H}_{rot} + F\,(p - \mathbf{P})^2 + V(\theta) \quad . \tag{35}$$

Here, H_{rot} is the standard rigid-rotor asymmetric rotational Hamiltonian and F is the effective rotational constant for the internal motions of the top about its symmetric axis, which is calculated as follows:

$$F = \frac{h^2}{8\pi^2 r I_{top}} \; ; \quad r = 1 - \sum_g \frac{\lambda_g}{I_g} \; , \quad g = (a,b,c) \quad . \tag{36}$$

Here, I_{top} is the moment of inertia of the top about the symmetric axis, (I_a, I_b, I_c) are the principal moments of inertia of the whole molecule, and $(\lambda_a, \lambda_b, \lambda_c)$ are the direction cosines of the symmetric axis of the top to the principal axes.

Since there is a plane of symmetry, λ_c vanishes. The momenta $\mathbf{P}$ and $\mathbf{p}$ are defined as

$$\mathbf{P} = \sum_i \mathbf{P}_i \hat{i} \; ; \; \mathbf{P}_i = \frac{\partial T}{\partial \omega_i} \; , \quad (i=a,b,c) \; ; \; p = \frac{\partial T}{\partial \theta} \; , \qquad (37)$$

where T = (H-V) and ω_i is the angular velocity about i axis.

In the second term in Eq. (35), $(\mathbf{p}-\mathbf{P})$ represents the relative angular momentum of the top and the frame. The Hamiltonian in Eq. (35) can be rewritten as

$$\mathbf{H} = A^{*\prime} \mathbf{P}_a^2 + B^{*\prime} \mathbf{P}_b^2 + C^* \mathbf{P}_c^2 - 2F(\alpha \mathbf{P}_a p + \beta \mathbf{P}_b p) \qquad (38)$$
$$+F\alpha\beta (\mathbf{P}_a \mathbf{P}_b + \mathbf{P}_b \mathbf{P}_a) + Fp^2 + V(\theta) \; ,$$

where

$$A^{*\prime} = A^* + F\alpha^2 \; , \quad B^{*\prime} = B^* + F\beta^2 \; , \quad \alpha = \frac{\lambda_a I_{top}}{I_a} \; , \quad \beta = \frac{\lambda_b I_{top}}{I_b} \; . \qquad (39)$$

The Hamiltonian matrix element can be set up using the symmetric prolate top - free rotor basis set. Nonvanishing elements of the Hamiltonian matrix are

$$\langle J\,K\,M\,m \mid \mathbf{H} \mid J\,K\,M\,m \rangle =$$

$$A^{*\prime}K^2 + \frac{1}{2}(B^{*\prime}+C^{*})\,[J(J+1)-K^2] - 2F\alpha Km + Fm^2 + \frac{V_0}{2} + \frac{V_1}{2} \qquad (40)$$

$$\langle J\,K\,M\,m \mid \mathbf{H} \mid J\,K\pm1\,M\,m \rangle =$$

$$F\beta\,[\tfrac{1}{2}\alpha(2K\pm1) - m]\,[J(J+1) - K(K\pm1)]^{\frac{1}{2}} \qquad (41)$$

$$\langle J\,K\,M\,m \mid \mathbf{H} \mid J\,K\pm2\,M\,m \rangle =$$

$$\frac{1}{4}(B^{*\prime}-C^{*})\,[J(J+1) - K(K\pm1)]^{\frac{1}{2}}\,[J(J+1) - (K\pm1)(K\pm2)]^{\frac{1}{2}} \qquad (42)$$

$$\langle J\,K\,M\,m \mid \mathbf{H} \mid J\,K\,M\,m\pm2 \rangle = -\frac{V_0}{4} \qquad (43)$$

$$\langle J\,K\,M\,m \mid \mathbf{H} \mid J\,K\,M\,m\pm4 \rangle = -\frac{V_1}{4} \qquad (44)$$

The effect of internal rotation is quite noteworthy. The diagonal matrix element term of (-2FαKm) arises from the coupling of internal rotation and the overall rotation. The effective rotational constants about the principal axes have been modified due to the effect of internal rotation.

The off-diagonal matrix elements for K are very small for the nearly symmetric top ketene molecule at transition state ($\beta \approx 0.0092$, $(B^{*\prime}-C^{*}) \approx 0.026$ cm^{-1} for CH_2CO), and K-splitting is not expected to be observed with the experimental resolution of 1 cm^{-1} in this work. Thus the matrix elements off-diagonal in K are neglected in the

calculation. In this case, Hamiltonian matrix elements at a specific K quantum number can be set using the free-rotor basis set as follows:

$$\langle m \mid \mathbf{H} \mid m \rangle = F m^2 - 2F\alpha Km + \frac{V_0}{2} + \frac{V_1}{2} \qquad (45)$$

$$\langle m \mid \mathbf{H} \mid m\pm2 \rangle = -\frac{V_0}{4} \qquad (46)$$

$$\langle m \mid \mathbf{H} \mid m\pm4 \rangle = -\frac{V_1}{4} \qquad (47)$$

The energy levels of hindered internal rotor at each K quantum number are calculated by diagonalizing the above Hamiltonian matrix, and the rovibrational energy levels are calculated by adding the symmetric top approximated rotational energies using ($A^{\ddagger\prime}$,$B^{\ddagger\prime}$,$C^{\ddagger}$) as rotational constants. The 40 x 40 Hamiltonian matrix is diagonalized to give the eigenvalues. The corresponding eigenfunctions are the linear combinations of the free rotor wavefunctions with different m quantum numbers. All parameters used in the calculation are listed in Table II.

Because the coupling between K and m is significant,[43] the symmetry for the rovibrational state, Γ_{rv}, is determined for each (m,K) rovibrational state. As mentioned earlier, nuclear spin statistical weights of the rovibrational states are determined by considering the total symmetry. The nuclear spin statistical weights for (m,K) rovibrational states are determined in Hund's case (b), since the

rotational spin-orbit coupling is not expected to be larger than the rotational energy. In Table III and IV, energy levels with nuclear spin statistical weights for hindered rotor states coupled to K quantum numbers are listed for CH_2CO and CD_2CO transition states, respectively, when V_0 = 330 cm^{-1} and V_1 = -20 cm^{-1}. In Table III and IV, the hindered rotor energy levels coupled to each K are listed with respect to the corresponding zero-point energies. The splitting of the zero-point energies due to the coupling of the hindered internal rotation and the overall rotation is less than ≈ 2 cm^{-1} and neglected in the RRKM calculation. For the rovibrational energies of (N,K,m) rovibrational states, the rotational energies using the symmetric-top approximation are added.

Since the nuclear spin quantum number (I,M_I) is expected to be conserved, the threshold energies for ortho states of CH_2CO at the transition state should be ≈ 9.7 cm^{-1} lower than the energy term values listed in Tables III, while the threshold energies for para states remain the same (*vide supra*). For CD_2CO, since ortho states (K=0) lie below para states (K=1) in the ground state, threshold energies for para rovibrational states should be ≈ 5.0 cm^{-1} (energy difference between 1_{10} and 0_{00} states) lower than the energy term values listed in Tables IV, while those for ortho states remain unchanged.

Since the extent of K-mixing in highly vibrationally

excited states of ketene is not known at the present time, the accessible K quantum number of ketene at transition state is not certain. If K is strictly conserved throughout the dissociation, according to selection rules for K in Eqs. (30)-(31), only $|K| = 0 - 2$ states will be significantly accessible. For the case of complete K-mixing, $|K| = 0 - J'$ states are accessible, where J' can be populated up to 5 (≈5% at J=5). Two limiting cases will be considered in RRKM calculations in section G.

E. Reaction Barrier and Tunneling

The reaction barrier relative to the products, E_b, and the imaginary frequency, ν_i, along the reaction coordinate for the triplet channel of ketene have been determined by fitting the rate constant data in the threshold region using RRKM calculations as described in Eqs. (13) - (22) and the rotational term values of ketene at the transition state. K is assumed to be strictly conserved in RRKM calculations (*vide infra*).

For the CH_2CO dissociation, since the sharp step in k(E) is observed in the short range of the photolysis energy (28,200 - 28,300 cm-1), the uncertainty in the threshold energy has been greatly reduced. The first rise in k(E) in the 28,250-28,300 cm^{-1} region of photolysis energy is well reproduced by RRKM calculation when E_{th}(triplet) = 28,250 ± 10

cm^{-1} and ν_i = (100 ± 40) *i* cm^{-1} in Figure 12 (a). If K is assumed to be completely mixed in RRKM calculations, the lower imaginary frequency (≈ 80 *i* cm^{-1}) and higher density of reactant states (≈ 1.2 times) should be used to fit rate constants in the threshold region (*vide infra*). Threshold energy is the difference between zero-point energy (ZPE) levels of ground state of parent molecule and transition state. The singlet-triplet splitting of CH_2, Δ_{ST}, has been measured to be 3147 ± 5 cm^{-1}.[44] The singlet threshold energy for CH_2CO dissociation has been accurately measured by the $^1CH_2$ PHOFEX spectra, E_{th}(singlet) = 30,116.2 ± 0.4 cm^{-1}.[14] Therefore, the reaction barrier relative to the products, E_b, is determined by

$$E_b = [\ \Delta_{ST} - \{\ E_{th}(\text{singlet}) - E_{th}(\text{triplet})\ \}\ ] \qquad (48)$$

to give E_b = 1281 ± 15 cm^{-1} (3.66 ± 0.05 kcal/mol). This is about 40 % less than the *ab initio* calculation of 5.8 kcal/molecule.[23]

For the dissociation of CD_2CO, k(E) measurement in the reaction threshold region was not possible experimentally (*vide supra*), and the first distinct step in PHOFEX spectrum for CO (v=0,J=12) product taken at a 1.7 μs reaction time has been used for the calculation of the threshold energy. In the PHOFEX spectrum, there is small background signal giving a long tail below the threshold energy due to the existence

of CH_2CO as a impurity (<≈2%) and vibrationally hot CD_2CO (<≈10%). This background tail makes it impossible to evaluate the imaginary frequency for the ZPE level of the transition state. The first distinct step in the Q(12) PHOFEX curve is observed in the 28,280 -28,330 cm^{-1} region of photolysis energy and give the reaction threshold energy of 28,310 ± 15 cm^{-1} (E_{th}'), Figure 12 (b). The solid line in Figure 12 (b) is the RRKM rate constant calculated without the tunneling correction. The zero-point energies of parent $CH(D)_2CO$ molecules and $^3CH(D)_2$ fragments are calculated using the spectroscopic and theoretical results, respectively, and listed in Table V.[31,45] The barrier height relative to products, E_b', is given by

$$E_b' = E_b + ZPE(^3CH_2-^3CD_2) - [E_{th}+ZPE(CH_2CO-CD_2CO) - E_{th}'], \quad (49)$$

where $ZPE(^3CH_2-^3CD_2)$ is the difference of zero-point energies between $^3CH_2$ and $^3CD_2$ fragments, 886 cm^{-1}, and $ZPE(CH_2CO-CD_2CO)$ is the difference of zero-point energies between the ground states of CH_2CO and CD_2CO, 1156 cm^{-1}. The estimated reaction barrier is found to be 1071 ± 40 cm^{-1} (3.06 ± 0.10 kcal/molecule). The difference in ZPE's between CH_2CO and CD_2CO at transition states can be estimated by $[E_{th} - E_{th}' + ZPE(CH_2CO-CD_2CO)\}\ ]$ to give 1096 ± 20 cm^{-1}. The vibrational frequencies of CD_2CO transition state are calculated by normal-mode analysis using the *ab initio* (DZP CISD level

calculation) values for force constants and geometry parameters of CH_2CO transition state (Table I). The difference between *ab initio* values for ZPE's of CH_2CO and CD_2CO transition states is calculated to be 1095 cm^{-1}. If the torsional frequencies listed in Tables III and IV are used for the calculation of the zero-point energies, it becomes 1091 cm^{-1}. These agree very well with the experimentally estimated value of 1096 cm^{-1}. The energetic diagram for the triplet channels of the CH_2CO and CD_2CO dissociations is shown in Figure 13.

A much lower imaginary frequency than predicted by *ab initio* calculation (523 *i* cm^{-1}) had to be used to explain the first step in k(E) for CH_2CO dissociation. The imaginary frequency has been estimated by the calculation of one-dimensional tunneling probability assuming the Eckart potential function for the exit valley of the potential energy surface along the reaction coordinate. Therefore, the imaginary frequency obtained here has a meaning only if this simple one-dimensional picture is valid. In this picture, the low imaginary frequency implies the existence of a very broad barrier along the reaction coordinate. Other approaches to explain the observed sharp step in k(E) are possible. For example, if a small potential minimum exists on the PES along the reaction coordinate at the transition state, the transmission probabilities associated with the quantized transition states would have "resonance-like"

features giving sharp resonances right at the threshold energies of the transition state.[46] Since the single step in k(E) is associated with many rotational threshold energy levels of the transition state, it is nontrivial to extract the tunneling probability associated with a single quantum state of the molecule at transition state. Hence a complete test of this model for the detailed step shapes in the dissociation rate of ketene is not possible at the present time. The angular momentum resolved rate constant measurement would be very useful for this purpose.

F. The C-C-O bending mode of ketene at transition state

The partitioning of the available energy into the degrees of freedom of the products in the dissociation of ketene on the triplet surface is dynamically controlled due to the existence of a small barrier on the potential surface along the reaction coordinate. The fast energy release from the transition state occurs through the repulsive exit valley on the potential energy surface. The CO fragment angular momentum distribution is determined by the repulsive energy and the characteristic vibrational structure of the transition state through which ketene dissociates. The angular momentum released to the CO fragment for each vibrational state of ketene at transition state is unique, and information about the vibrational structure of the

transition state could be obtained from the change of CO product rotational distribution as a function of the available energy.

The CO fragment rotational distributions from the CH_2CO dissociation at photolysis energies near the reaction threshold have been measured by Chen and Moore.[18] The impulsive model considering the effect of zero-point motions of ketene at the transition state reproduces the experimental, Gaussian-shaped distribution quite well, as shown in Figure 3. The impulsive model assumes that the repulsive energy, the total available energy for products, is oriented entirely along the dissociative C-C bond as an impulse. In this case, the available energy, E_{avl}, is released as the kinetic energies of repulsive carbon atoms. Since recoiling carbon atoms have the same mass, half of the available energy is released into each fragment. From the conservation of linear momentum, the translational energy of CO fragment is given by

$$E_t(CO) = \frac{m_C}{m_C + m_O} \frac{1}{2} E_{avl} \quad , \tag{50}$$

where m_x is the mass of atom X. The torque generated by the impulse gives the angular momentum for CO fragment, and the rotational energy of CO fragment is given by

$$E_{rot}(CO) = \frac{m_O}{m_C + m_O} \sin^2\delta \; \frac{1}{2} E_{avl} \quad , \qquad (51)$$

where δ is the angle of C-C-O.

The impulsive model is physically not very reasonable because it predicts the partitioning of the available energy into vibrational degrees of freedom of fragments even when the available energy is not enough to excite the vibration of fragments. The modified impulsive model is a more reasonable one to use. In the modified impulsive model, vibration of fragment is treated adiabatically (i.e. infinitely stiff bonds for the fragments) and the energy which goes into vibration in the impulsive model partitions between fragment rotation and translation. The available energy for rotation and translation of fragments for each vibrational level, E_{avl}', is given by

$$E'_{avl} = E_{avl} - E_{vib}(v_{CH_2}, v_{CO}) \quad , \qquad (52)$$

where v_{CH2} and v_{CO} are vibrational quantum numbers for CH_2 and CO fragments, respectively. The rotational energy for CO fragment is given by

$$E_{rot}(CO) = \frac{m_O \sin^2\delta}{(m_C+m_O)\left[1 - \frac{m_O}{2(m_C+m_O)}\cos^2\delta\right]} \; \frac{1}{2} E'_{avl} \quad . \qquad (53)$$

The modified impulsive model calculation using *ab initio* transition state structure (C_s^{II}, CISD) predicts that 22.6 %

of the available energy goes into the rotational energy of CO fragment when it is assumed that 10 % of $^3CH_2$ fragment is vibrationally excited at the photolysis energies near the reaction threshold of CH_2CO dissociation.[47] This agrees very well with the experimental data of 22.4 %.[18]

The impulsive model predicts only the average rotational energy, and the corresponding angular momentum of CO fragment is determined by

$$J_{CO} = \left[\frac{B_{CO} + 4E_{rot}(CO)}{4B_{CO}}\right]^{\frac{1}{2}} - \frac{1}{2} \quad , \tag{54}$$

where B_{CO} is the rotational constant of CO fragment. The width of rotational distribution originates primarily from the zero-point vibrational motion of ketene at the transition state.[18,48] The effect of the overall rotation of the parent molecule is negligible, since only low J's of the reactant is significanlty populated in the supersonic beam.[18,49] The detailed model for the calculation of the width of the CO rotational distribution from the zero-point vibrational motions has been described in Refs. 18, 48, and 49. Briefly, the Cartesian coordinates of linear momentum of five atoms of ketene at transition state are calculated at classical turning points for each normal mode, and the corresponding CO fragment angular momentum is classically calculated at a fixed equilibrium geometry of ketene at transition state. The calculated CO angular momenta transferred from six in-plane normal modes are perpendicular to the molecular plane,

and convoluted in the manner appropriate for a Gaussian function to give the classically allowed CO angular momentum uncertainty along the c axis, $\Delta J_{\perp}$. The zero-point motions of two out-of-plane normal modes give the uncertainty of CO angular momentum along the C-C bond, $\Delta J_{\parallel}$. The most probable J of CO fragment calculated from the impulsive model, J_{imp}, is perpendicular to the molecular plane. The Gaussian-shaped CO rotational distribution is calculated by the convolution of the distribution of the angular momentum perpendicular to the molecular plane, $P_0(J_{\perp})$, and that along the C-C bond, $P_0(J_{\parallel})$, as follows:

$$P(J) = \left\{ \int_0^{2\pi} \frac{\exp\left[-(J_{\perp}-J_{imp})^2/(\Delta J_{\perp})^2 - J_{\parallel}^2/(\Delta J_{\parallel})^2\right] d\phi}{\pi \Delta J_{\perp} \Delta J_{\parallel}} \right\}_J , \quad (55)$$

where J is the magnitude of total angular momentum, $J_{\perp} = J\cos\phi$, and $J_{\parallel} = J\sin\phi$. The integral over ϕ is numerically evaluated and converted to the quantum state distribution by binning into the nearest rotational quantum number.

The zero-point motion from the C-C-O bending mode gives the largest contribution to the width for the CO rotational distribution ($\Delta J_{\perp} \approx 5$).[19] The scaled *ab initio* frequency for C-C-O bend is 252 cm^{-1}, and a noticeable change of CO rotational distribution is expected to occur when the first quantum of C-C-O bending mode of ketene at the transition state is energetically accessible. In the harmonic

oscillator approximation, the momentum distribution for the first quantum of C-C-O bend is a bimodal Gaussian function. The CO angular momentum transferred from the first quantum of C-C-O bend would reflect the bimodal linear momentum distribution. The distribution of CO angular momentum transferred from C-C-O bending motion at (v=1) C-C-O bend, $P_1(J_\perp)$, is determined by the bimodal Gaussian-shaped linear momentum distribution, and given by

$$P_1(J_\perp) = \frac{2}{\sqrt{\pi}(\Delta J_{\perp 1})^3} J_\perp^2 \exp[-\frac{(J_\perp)^2}{(\Delta J_{\perp 1})^2}] \quad , \qquad (56)$$

where $\Delta J_{\perp,1}$ is the CO angular momentum uncertainty along the c axis calculated from the classically allowed maximum linear momenta of atoms at (v=1) C-C-O bending mode. Now, the distribution of angular momentum perpendicular to the molecular plane only from the C-C-O bending motion, $P_1(J_\perp)$, is convoluted with that from the other in-plane zero-point vibrational motions. This gives the distribution of the CO angular momentum perpendicular to the molecular plane from (v=1) C-C-O bend state, $P'(J_\perp)$. The CO rotational distribution from (v=1) C-C-O bend is calculated by the convolution of $P'(J_\perp - J_{imp})$ with $P_0(J_\parallel)$. The effect from vibrationally excited H-C-C-O torsional mode is also included by the same way as above. But this time, the vibrational motion of the torsional mode contribute to the distribution of angular momentum which is along the C-C bond, $J_\parallel$.

The CO rotational distribution at an available energy

can be calculated by summing the distributions from each vibrational state of ketene at transition state multiplied by the corresponding statistical weight of each vibrational state. The vibrational frequencies for hindered internal rotation listed in Table III are used to determine the population of each vibrational state. The yields of the CO fragment in (v=0,J=2) state, P(E,v=0,J=2), and in (v=0,J=12) state, P(E,v=0,J=12), are calculated as a function of the available energy.

In Figure 14 (a), the PHOFEX curve probing the Q(2) transition of CO taken at a 50 ns reaction time is divided by the PHOFEX curve probing the Q(12) transition of CO taken at 50 ns of the reaction time. From Eq. (2), the $\sigma(E)*[1-\exp(-k(E)*\Delta t)]$ terms for these PHOFEX curves are canceled out, and the ratio of these PHOFEX curves gives the ratio of the yield of the CO fragment in (v=0,J=2) state to that in (v=0,J=12) state. The calculated P(E,v=0,J=2)/P(E,v=0,J=12) is shown in Figure 14 (b). The overall shape of the ratio as a function of the energy is well explained by the calculation, and the sharp peaks at around 28,500 and 28,600 cm^{-1} in the curve in Figure 14 (a) are well reproduced by the calculation, Figure 14 (b), when the vibrational frequency of C-C-O bend is 250 ± 10 cm^{-1}. This agrees very well with the scaled *ab initio* values of 252 cm^{-1}. For CD_2CO, the vibrational frequencies for torsional mode of the molecule at transition state is about 20 % lowered by the isotopic shift, and the effect of C-C-O

bending mode on the CO rotational distribution is less pronounced than that for CH_2CO as shown in Figure 9 (c). Since much more vibrational states of the transition state are involved in the small range of the photolysis energy compared to CH_2CO, the quantitative calculation for the CO(v=0,J=2) PHOFEX curve from the dissociation of CD_2CO is complicated and has not been tried at the present time. The distinct steps observed in the Q(2) PHOFEX in Figure 9 (c) are also likely to be associated with the C-C-O bending modes by the same reason as above, and the energies associated with these steps could be very helpful for the assignment of the C-C-O bending mode.

G. The RRKM Calculations

The RRKM calculations are carried out using Eqs. (13)-(16). The angular momentum distribution of the excited reactant states from parallel (A-type) or perpendicular (B-,C-types) transitions are identical within one unit of the angular momentum; the linestrengths of the perpendicular transition are used for the RRKM fits presented here. The rate constants are calculated for each angular momentum (J'), and averaged over the distribution of J' in the reactant states. The selection rules of N for the intersystem crossing ($\Delta N = 0, \pm 1$) are applied, and the distribution of rotational angular momentum (N) at the transition state is

thus extended one more unit. The rate constants for each nuclear spin state are calculated separately and averaged with the proper nuclear spin statistical weights.

For the energy levels of the H(D)-C-C-O torsional modes of transition states, the hindered internal rotor energy levels are calculated by the method described in section D with varying V_0 and V_1. The rotational energies corresponding to (N,K) states of ketene at transition states are added to the calculated hindered rotational energies at each K state. Since the nuclear spin quantum number is conserved, the energy levels of (m,K) states with ortho or para states are used for the rate constants for ortho or para states of the reactant, respectively. The vibrational frequencies for C-C-O bend ($\nu_7^{\ddagger}$), $CH(D)_2$ wag ($\nu_8^{\ddagger}$), and $CH(D)_2$ rock ($\nu_5^{\ddagger}$) of transition states are important factors in the RRKM fits to the experimental results, and these are varied from the scaled *ab initio* values to fit the experimental results. The vibrational frequency for C-C-O bend of CH_2CO at transition state is found to be around ≈ 250 cm^{-1} from the analysis of the Q(2) PHOFEX spectrum in section F, and varied within ± 10 cm^{-1} for the RRKM calculations. The density of vibrational states of the reactant, $\rho(E)$, is varied to fit the experimental results by multiplying $\rho_{WP}(E)$ by the scale factor, f, where $\rho(E) = f * \rho_{WR}(E)$.

The most distinct steps observed in k(E) for both CH_2CO and CD_2CO dissociations are associated with the torsional

modes of the molecules at transition state which have been treated as hindered internal rotation approximation in section D. The hindered internal rotation is strongly coupled to the K quantum number of the molecule at the transition state. Each K state coupled to each hindered rotor energy level of transition state has its own threshold energy for the dissociation. Therefore, the most sensitive factor in carrying out the RRKM calculation is the population of the accessible K states of the molecule at transition state. The selection rules for K quantum number, as discussed earlier, depend on the mechanism of the intersystem crossing, and the extent of K-mixing in highly vibrationally excited states. Since these are uncertain at the present time, the categorization into three cases for K states of ketene at transition state would be very meaningful.

The RRKM calculations can be carried out for the following three cases:

(A) K is totally mixed in the highly vibrationally excited states of the reactant, and the population of K states are determined by the population of the J' states.

(B) K is nearly conserved in the highly vibrationally excited states of the reactant and K=0-4 are accessible at transition state due to the second-order intersystem spin-orbit coupling (*vide supra*).

(C) K is conserved throughout the internal conversion, intersystem crossing, and the dissociation, and only K=0-2

are accessible at transition state.

Since the ground state ketene molecule is supersonically cooled to the rotational temperature of 3-5 K, only low J' states are significantly populated in the reactant states. Therefore, even in the case of (A), the case of the complete K-mixing, only K=0-4 states are significantly populated, and the RRKM calculations for the cases of (A) and (B) give the nearly same results. Thus RRKM calculations are carried out for the cases of (A) and (C).

The spin-orbit coupling of ketene at transition state is not expected to be larger than the rotational energy, and Hund's case (b) is applied in determining the symmetries of rovibrational states of ketene at transition state. Thus the electron spin multiplicity of 3 is multiplied by the number of the vibrational states of the transition state. In the case (C), the relative linestrengths for the parallel and perpendicular transitions could be important in determining the relative populations of K states due to the different selection rules of K for two transitions, as discussed in section C. But in the case (C), since K is restricted to K= 0-2, the threshold energies for different K states at a vibrational state of transition state are within a narrow energy range of $\approx$ 12 cm^{-1}, and it was found that the RRKM fits are insensitive to the type of the optical transitions. The RRKM fits assuming the same linestrengths for two transitions are presented.

In order to reproduce the sharp steps observed in k(E) by the RRKM calculations, the number of vibrational states of the transition state, $N^{\ddagger}(E)$, is calculated without one-dimensional tunneling except for the first step in k(E) for the CH_2CO dissociation, which is associated with zero-point energy level of transition state. That is, instead of P(x) in Eq.(13), the normal step function, h(x), is used. The step function is defined as follows.

$$h(x) = 0, \quad x<0$$
$$= 1, \quad x>0 \qquad (57)$$

(i) The case of K-mixed

(i)-(1) The RRKM fits to k(E) of the CH_2CO dissociation

The RRKM rate constants for the CH_2CO dissociation are calculated for the case (A), using the parameters listed in Table VI, and compared with the experiment in Figure 15 (a). The step function, Eq. (57), is used for the RRKM fit as the transmission probability to give the solid line in Figure 15 (a). The experimental rate constants and the RRKM rate constants are overall in a good agreement. The positions and amplitudes of the observed steps in k(E) are quantitatively very well reproduced by the RRKM calculation in the 28,350 - 28,500 cm^{-1} range of the photolysis energy.

For convenience, the first four distinct steps in the measured rate constants are marked with arrows and assigned to steps (I), (II), (III), and (IV) in Figure 15 (a). According to the RRKM calculation for the case of K-mixed, each step can be assigned to:

(I) - the zero-point energy level of the transition state,

(II) - the first excited hindered rotor states with K=0 for a nuclear spin state,

(III) - K=3 state at the (II) vibrational state,

(IV) - the second excited hindered rotor states with K=0.

For the step (I), the RRKM fit using the step function does not reproduce the experiment in terms of the slope of the step. The RRKM fit with one-dimensional tunneling correction using Eqs. (19)-(22) with the imaginary frequency of 100 i cm^{-1} is shown as the broken line, and still does not explain the experimental results in the reaction threshold region. For the best fit to the experiment, the density of states of the reactant needs to be 1.2 times higher than that used in the RRKM fit shown as the solid line in Figure 15 (a). This is inconsistent with the good agreement between the RRKM fit and the experiment at higher photolysis energies above the reaction threshold. Therefore, this could be the negative evidence against this model. But since the uncertainties of the measured rate constants in the reaction threshold region are relatively large, this is not conclusive.

For the steps (II) and (IV), the RRKM fit using the step function as the transmission probability gives the excellent agreement in terms of both the positions and amplitudes of steps in k(E). The RRKM calculations considering the tunneling through the barrier with a imaginary frequency higher than 30-40 i cm^{-1} do not predict the observed sharp steps. In Figure 15 (b), the RRKM fit including the tunneling through the barrier with the imaginary frequency of 40 i cm^{-1} is shown with the experiment. The sharp slope of the steps in measured k(E) could not be reproduced.

The step (III) which might be associated with the K=3 state is not perfectly matched with the RRKM fit in terms of the amplitude of the step. The RRKM fit predicts a small amplitude in k(E) at K=3, while the experiment shows a rather sharp step at the same position of the energy. The relative amplitudes of the steps associated with K rotational states are related to the relative populations of K states of the reactant. The relative distribution of K quantum numbers in the reactant results from UV excitation, internal conversion, K-mixing, and the more complicated intersystem crossing. Even though the population of K states in S_1 state can be calculated for each type of the transition, there are still many uncertain factors to be considered such as the relative magnitude of the spin-orbit coupling matrix element for different (J,K) states and the extent of K-mixing in highly vibrationally excited reactant states. The measurement of

the angular momentum resolved rate constants would be extremely useful for the explanation of the fine structures of observed rate constants.

(i)-(2) The RRKM fits to k(E) of the CD_2CO dissociation

The RRKM calculation for k(E) of the CD_2CO dissociation is carried out for case (A), the case of complete K-mixing, in Figure 16. The step function is used for the transmission probability. The parameters used in the RRKM fit are listed in Table VI. The same values for V_0 and V_1 as used for CH_2CO rate constants are used for CD_2CO. The RRKM calculations with the tunneling turned out to give the same conclusion as described above for the CH_2CO dissociation, and this is not shown.

The first two steps above the reaction threshold, the steps (II) and (III) in Figure 16, are associated with the first and second excited hindered rotor energy levels of the transition state, and the RRKM fit is in good agreement in terms of both the amplitudes and positions. But for the step (III), the RRKM fit is about 5-10 cm^{-1} blue shifted compared to the experiment, and there are some deviations for the rate constants at photolysis energies higher than 28,550 cm^{-1}. These deviations could result from vibrational anharmonicity and/or strong coupling of rovibrational states at the transition state.

The most striking feature in k(E) for the CD_2CO dissociation is the resonance-like structure observed in the step (II) in Figure 16. The RRKM calculation does not predict the sharp peak in rate constants. The similar type of the structure in k(E) is also observed for the CH_2CO dissociation, Figure 15 (a), though it is less pronounced than that for CD_2CO. These resonance-like features in rate constants could result from the existence of energy minimum for the transition state on the potential energy surface along the reaction coordinate.[46] The reaction coordinate might not be completely decoupled from the other vibrational motions of the molecule at the transition state, and one may need to consider the complicated multi-dimensional potential energy surface in the vicinity of the transition state and the dynamics of recrossing.

(ii) The case of K-conserved

(ii)-(1) The RRKM fits to k(E) of the CH_2CO dissociation

The RRKM rate constants for CH_2CO dissociation are calculated for case (C), using the parameters listed in Table VII, and compared with the experiment in Figure 17. The step function, Eq. (57), is again used for the RRKM fit as the transmission probability to give the solid line in Figure 17. This fit also gives overall good agreement with the

experiment. For the case of K-conserved, case (C), only the states with K=0-2 are accessible in the transition state, and the RRKM calculations generate much sharper steps than those for the case of K-mixed. Therefore, the RRKM parameters for the case (C) need to be significantly changed from those used for the case (A). The parameters for the hindered internal rotation, V_0 and V_1, are changed to 240 and 20 cm^{-1}, respectively. The energy levels of the hindered rotor states are calculated in the same way as described in section D, and the energy levels are listed in Table VIII. The vibrational frequencies for the C-C-O bend and CH_2 wag are changed within ± 20 cm^{-1} from the values used in the RRKM fit for the case (A). And also the density of reactant states, $\rho(E)$, is changed. The best fit is obtained when f = 1.67 ± 0.17, and this is about 1.2 times higher than that obtained from the RRKM fit for the case (A).

The RRKM fit shown as the solid line in Figure 17 is overall in good agreement with experiment. The positions and amplitudes of the first two steps in k(E) are quantitatively very well reproduced by the RRKM calculation. The first four distinct steps in the measured rate constants are marked with arrows and assigned to steps (I), (II), (III), and (IV) in Figure 17. According to the RRKM calculation for the case of K-conserved, each step can be assigned to:

(I) - the zero-point energy level of the transition state,

(II) - the first excited hindered rotor states,

(III) - the split second or third excited hindered rotor states,

(IV) - the third or fourth excited hindered rotor states.

For the step (I), as in the case (A), the RRKM fit using the step function does not reproduce the experiment in terms of the slope of the step. But differently from the case (A), the RRKM fit for the case (C) with one-dimensional tunneling correction using Eqs. (19)-(22) with the imaginary frequency of 100 i cm^{-1} gives the excellent agreement with the experiment in the reaction threshold, as shown in Fig 17 (the dashed line). This could be positive evidence for the case (C), which assumes that K is strictly conserved throughout the dissociation.

For the steps (II), the RRKM fit using the step function as the transmission probability gives excellent agreement in terms of both the positions and amplitudes of steps in k(E). The RRKM calculations considering the tunneling through the barrier with a imaginary frequency higher than 40 i cm^{-1} do not predict the observed sharp steps, as demonstrated before in Figure 15 (b).

The step (III) which could be associated with split hindered rotor states is not matched with the RRKM fit in terms of the amplitudes and positions of the steps. The RRKM fit reproduces the step in measured k(E) observed at around 28,340 cm^{-1} of the photolysis energy, but it predicts additional steps in k(E) at the region of the energy between

the steps (III) and (IV). And also the step (IV) observed in measured k(E) is not reproduced by the RRKM fit. This is not explainable with the current simple treatment of the vibrational modes of the molecule at transition state.

(ii)-(2) The RRKM fits to k(E) of the CD_2CO dissociation

The RRKM calculation for k(E) of the CD_2CO dissociation is carried out for case (C), the case of K-conserved, in Figure 18. The step function is used for the transmission probability. The parameters used in the RRKM fit are listed in Table VII. Assuming that the bare barrier heights for the internal rotation, the barriers with respect to the zero-point energies of the other seven vibrational frequencies, are same for the CH_2CO and CD_2CO transition states, the parameters of V_0 = 230 cm^{-1} and V_1 = 20 cm^{-1} are used for the calculation of hindered rotor energy levels of CD_2CO transition state (Table VIII). The parameters used in the RRKM fit are listed in Table VII. The RRKM calculations with the tunneling turned out to give the same conclusion as described above for CH_2CO dissociation, and this is not shown.

The first two steps above the reaction threshold, steps (II) and (III) in Figure 18, are associated with the first

and second excited hindered rotor energy levels of the transition state, and the RRKM fit is in excellent agreement in terms of both the amplitudes and positions. Actually, in the entire range of photolysis energies where the rate constants of CD_2CO dissociation are measured, the RRKM fit reproduces the experiment beautifully.

(iii) Density of reactant states, $\rho(E)$

Since clear steps associated with vibrational states of the ketene molecule at its transition state are observed, it is now possible to measure the density of vibrational states of the reactant directly. The RRKM fits to k(E) of the CH_2CO and CD_2CO dissociations for the case (A) or (C) give the scale factors of f = 1.40 or 1.67 for CH_2CO and 1.88 or 2.14 for CD_2CO, respectively, where $\rho(E) = f * \rho_{WR}(E)$, as listed in Tables VI and VII. The WR approximation gives the ≈ 3.5 times higher density of reactant states for CD_2CO than that for CH_2CO. This combines with the ratio of f numbers (1.88/1.40) [≈ (2.14/1.67)] to give the actual ratio of density of states of CD_2CO to that of CH_2CO in the excited reactants, $[\rho(E;CD_2CO) / \rho(E;CH_2CO)] \approx 4.7 \pm 0.8$. The WR approximation is found out to be very useful in predicting the relative density of states for the reactants. At the photolysis energy of 28,500 cm^{-1}, the actual densities of

vibrational states of reactant are found to be ≈ 1.9 (2.3) x 10^4 ($/cm^{-1}$) and ≈ 9.0 (10) x 10^4 ($/cm^{-1}$) for CH_2CO and CD_2CO, respectively, where the values in parentheses are those from the RRKM fits for the case of K-conserved (*vide supra*).

(iv) The transition state vibrational frequencies

The *ab initio* calculations for the geometry and vibrational frequencies of ketene at its transition state by Allen and Schaefer were extremely useful in the interpretation of experimental results in this work. The impulsive model calculation based on the geometry of the *ab initio* transition state structure predicts the CO product rotational distribution quantitatively. The scaled *ab initio* value for the C-C-O bend of CH_2CO transtion state, 252 cm^{-1}, is in excellent agreement with the experimentally estimated value of 250 cm^{-1}. For the RRKM fits to the experiment, the scaled *ab initio* vibrational frequencies for some modes had to be about 80 ± 10 % red-shifted (See Table VI). Thus the actual transition state is somewhat looser than predicted by the *ab initio* calculations. The barrier of the internal rotation of ketene at transition state is found to be around 0.94 ± 0.10 kcal/mol or 0.66 ± 0.10 kcal/mol, which is 80 - 60 % of the *ab initio* values of 1.10 (CIDVD calculation) or 1.25 (CISD calculation) kcal/mol.

V. SUMMARY and CONCLUSION

Steplike structures are observed in the unimolecular reaction rate constants of ketene on the triplet surface. The sharp steps observed in the reaction threshold provide accurate values of 1281 ± 15 cm^{-1} and 1071 ± 40 cm^{-1} for the reaction barriers relative the products for the CH_2CO and CD_2CO dissociations, respectively. The measured rate constants are quantitatively well reproduced by the RRKM calculations. The distinct steps observed in the first 200 cm^{-1} region above the reaction threshold are associated with the hindered internal rotor energy levels. The barrier of the internal rotation is found to be 0.94 ± 0.10 or 0.66 ± 0.10 kcal/mol for both the CH_2CO and CD_2CO transition states depending on the model used for the RRKM calculations. The scaled *ab initio* vibrational frequencies had to be 80 ± 10 % red-shifted to fit the experiment.

The CO product rotational distribution is dynamically controlled by the shape of the exit valley of the potential energy surface and vibrational structure of the molecule at its transition state. The relative probability of low J's of CO product is most sensitive the C-C-O bending motions of the molecule at transition state and the vibrational frequency of C-C-O bend has been extracted from the CO (v=0,J=2) PHOFEX curve.

The RRKM calculations are sensitive to the dynamics of

K-mixing involved in the photodissociation. The RRKM calculations are carried out for two limiting cases, where K is completely mixed or K is strictly conserved. Most of the steplike structures in k(E) are quite well reproduced with the RRKM fits. But the RRKM fits for neither cases are perfectly matched with the fine structures observed in measured k(E) for both the CH_2CO and CD_2CO dissociations. The steplike structures in k(E) at energies above the reaction threshold are best reproduced by the RRKM fits when a step function is used for the transmission probability of each quantized channel. For the reaction threshold region for the CH_2CO dissociation, the RRKM fit using one-dimensional tunneling with an imaginary frequency of (100 ± 40) i cm^{-1} gives a good agreement with the experiment. The experiment suggests that the reaction thresholds might have resonance-like features in rate constants. The detailed theoretical approach for dealing with the possible coupling of bound vibrational motions of the molecule at the transition state to the reaction coordinate would be desirable.

The density of vibrational states of the excited reactant is directly calculated from the RRKM fits to measured rate constants. The Whitten-Rabinovitch approximation gives a good estimation for the ratio of the densities of CH_2CO and CD_2CO reactant states. The absolute value for the density of states are found to be 1.4 - 1.7 or 1.8 - 2.1 times higher than predicted by the WR approximation

in the 28,200 - 28,700 cm^{-1} range of the energy for CH_2CO or CD_2CO, respectively.

In this work, RRKM theory has been tested for the first time with quantum-mechanically resolved experiment and the RRKM theory was found to be excellent in predicting the rate constants of the unimolecular reaction of ketene. Both the number of the vibrational states of the transition state and the density of states of the reactant are well defined in the steplike structured rate constants. But the detailed fine structures in k(E) could not be explained by the conventional RRKM theory. The dynamics of K-mixing in highly vibrationally excited reactant states still remains uncertain. For a better understanding of the reaction dynamics associated with quantized reaction thresholds of the transition state, detailed calculations for the potential energy surface in the vicinity of the transition state will be necessary. Experimentally, the measurement of the angular momentum resolved rate constants, k(E,J), would be especially helpful in understanding the dynamics of K-mixing in the highly vibrationally excited state of the reactant.

REFERENCES

(1) R. A. Marcus and O. K. Rice, J. Phys. Colloid Chem. 55, 894 (1951); R. A. Marcus, J. Chem. Phys. 20, 359 (1952); R. B. Bernstein and A. H. Zewail, J. Phys. Chem. 90, 3467 (1986).

(2) C. E. Dykstra, Annu. Rev. Phys. Chem. 32, 25 (1981); C. W. Bauschlicher, S. R. Langhoff, P. R. Taylor, Adv. Chem. Phys. 77, 103 (1990).

(3) F. F. Crim, Annu. Rev. Phys. Chem. 35, 657 (1984); H. Reisler and C. Wittig, Annu. Rev. Phys. Chem. 37, 307 (1986); W. H. Green, C. B. Moore, and W. F. Polik, Annu. Rev. Phys. Chem. 43, 591 (1992).

(4) L. Brouwer, C. J. Cobos, J. Troe, H.-R. Dubal, and F. F. Crim, J. Chem. Phys. 86, 6171 (1987); T. R. Rizzo, C. C. Hayden, and F. F. Crim, Faraday Disc. Chem. Soc. 75, 276 (1983).

(5) W. F. Polik, D. R. Guyer, and C. B. Moore, J. Chem. Phys. 92, 3453 (1990).

(6) Y. S. Choi and C. B. Moore, J. Chem. Phys. 97, 1010 (1992).

(7) P. Pechukas and J. C. Light, J. Chem. Phys. 42, 3281 (1965); C. E. Klots, J. Phys. Chem. 75, 1526 (1971).

(8) M. Quack and J. Troe, Ber. Bunsenges. Phys. Chem. 78, 240 (1974); 79, 170 (1975); 79, 469 (1975).

(9) C. Wittig, I. Nadler, H. Reisler, J. Catanzarite, and G. Radhakrishnan, J. Chem. Phys. 83, 5581 (1985).

(10) D. M. Wardlaw and R. A. Marcus, Chem. Phys. Lett. 110, 230 (1984); J. Chem. Phys. 85, 3724 (1986).

(11) S. J. Klippenstein, L. R. Khundkar, A. H. Zewail, and R. A. Marcus, J. Chem. Phys. 89, 4761 (1988).

(12) E. D. Potter, M. Gruebele, L. R. Khundkar, and A. H. Zewail, Chem. Phys. Lett. 164, 463 (1989).

(13) S. J. Klippenstein and R. A. Marcus, J. Chem. Phys. 91, 2280 (1989); 93, 2418 (1990).

(14) W. H. Green, I-C. Chen, and C. B. Moore, Ber. Bunsenges. Phys. Chem. 92, 389 (1988); I-C. Chen, W. H. Green, and C. B. Moore, J. Chem. Phys. 89, 314 (1988).

(15) W. H. Green, A. J. Mahoney, Q.-K. Zheng, and C. B. Moore, J. Chem. Phys. 94, 1961 (1991).

(16) S. K. Kim, Y. S. Choi, C. D. Pibel, Q.-K. Zheng, and C. B. Moore, J. Chem. Phys. 94, 1954 (1991).

(17) S. K. Kim and C. B. Moore, unpublished result.

(18) I-C. Chen and C. B. Moore, J. Phys. Chem. 94, 269 (1990).

(19) R. Hilbig and R. Wallenstein, IEEE J. Quant. Elect. 17, 1566 (1981).

(20) C. D. Pible, Ph. D. thesis, University of California at Berkeley, (1992).

(21) I-C. Chen and C. B. Moore, J. Phys. Chem. 94, 263 (1990).

(22) R. N. Dixon and G. H. Kirby, Trans. Faraday Soc. 62, 1406 (1966); R. G. W. Norrish, H. G. Crone, and O. Saltmarsh, J. Chem. Soc. 1533 (1933).

(23) W. D. Allen and H. F. Schaefer III, J. Chem. Phys. 89, 329 (1988); 84, 2212 (1986).

(24) J. W. Rabalais, J. M. McDonald, V. Scherr, and S. P. McGlynn, Chem. Rev. 71, 73 (1971).

(25) V. Zabransky and R. W. Carr, J. Phys. Chem. 79, 1618 (1975).

(26) W. H. Miller, J. Am. Chem. Soc. 101, 6810 (1979).

(27) P. D. Mallinson and L. Nemes, J. Mol. Spectrosc. 59, 470 (1976).

(28) H. S. Johnston, " Gas Phase Reaction Rate Theory", Ronald Press, New York (1966).

(29) C. Eckart, Phys. Rev. 35, 1303 (1930).

(30) G. Z. Whitten and B. S. Rabinovitch, J. Chem. Phys. 38, 2466 (1963).

(31) C. B. Moore and G. C. Pimentel, J. Chem. Phys. 38, 2816 (1963).

(32) E. Abramson, R. W. Field, D. Imre, K. K. Innes, and J. L. Kinsey, J. Chem. Phys. 83, 453 (1985).

(33) A. Geers, J. Kappert, F. Temps, and W. Wiebrecht, Ber. Bunsenges. Phys. Chem. 94, 1219 (1990).

(34) W. Nadler and R. A. Marcus, Chem. Phys. Lett. 144, 24 (1988).

(35) M. Quack, Mol. Phys. 34, 477 (1977); p.355 in "Symmetries and Properties of Non-Rigid Molecules" ed. by J. Maruani and J. Serre, Elsevier press, New York (1983).

(36) W. H. Miller, J. Am. Chem. Soc. 105, 216 (1983).

(37) R. Hernandez, W. H. Miller, C. B. Moore, and W. F. Polik, J. Chem. Phys. (in press).

(38) C. G. Stevens and J. C. D. Brand, J. Chem. Phys. 58, 3324 (1973); J. C. D. Brand and C. G. Stevens, J. Chem. Phys. 58, 3331 (1973).

(39) C. C. Lin, Rev. Mod. Phys. 31, 841 (1959).

(40) E. B. Wilson, J. Chem. Rev. 27, 11 (1940); B. L. Crawford, J. Chem. Phys. 8, 273 (1940).

(41) G. Brocks, A. van der Avoird, B. T. Sutcliffe, and J. Tennyson, Mol. Phys. 50, 1025 (1983).

(42) P. A. Stockman, R. E. Bumgarner, S. Suzuki, and G. A. Blake, J. Chem. Phys. 96, 2496 (1992).

(43) G. Herzberg, "Molecular Spectra and Molecular Structure - II. Infrared and Raman Spectra of Polyatomic Molecules", D. Van Nostrand press, New York (1945). See p. 496.

(44) P. R. Bunker, P. Jensen, W. P. Kraemer, and B. Beardsworth, J. Chem. Phys. 85, 3724 (1986); P. Jensen and P. R. Bunker, J. Chem. Phys. 89, 1327 (1988).

(45) P. R. Bunker and P. Jensen, J. Chem. Phys. 79, 1224 (1983).

(46) R. S. Friedman and D. G. Truhlar, Chem. Phys. Lett. 183, 539 (1991).

(47) C. C. Hyden, D. M. Newmark, K. Shobatake, R. Sparks, and Y. T. Lee, J. Chem. Phys. 76, 3607 (1982).

(48) H. B. Levene and J. J. Valentini, J. Chem. Phys. 87, 2594 (1987).

(49) K. L. Carleton, T. J. Buttenhoff, and C. B. Moore, J. Chem. Phys. 93, 3907 (1990).

Table I. The scaled *ab initio* vibrational frequencies for the C_s^{II} transition states of CH_2CO and CD_2CO.

	CH_2CO[a]	CD_2CO[b]
ν_1(a′) asym C-H(D) stretch	3178	2380 (2573)
ν_2(a′) sym C-H(D) stretch	2997	2150 (2314)
ν_3(a′) C-O stretch	2029	2029 (2153)
ν_4(a′) $CH(D)_2$ scissor	1183	874 (930)
ν_5(a′) $CH(D)_2$ rock	472	383 (406)
ν_6(a′) C-C stretch	523*i*	514*i* (550*i*)
ν_7(a′) C-C-O bend	252	224 (232)
ν_8(a") $CH(D)_2$ wag	366	276 (283)
ν_9(a") H(D)-C-C-O torsion	154	126 (127)

a. Taken from Ref. 23.

b. Frequencies in parentheses are unscaled vibrational frequencies calculated by normal-mode analysis using *ab initio* force constants of CH_2CO. The same scale factors as used for CH_2CO are multiplied to give the values without parentheses.

Table II. Molecular parameters used in the calculation of hindered internal rotation energy levels of the transition state.

Parameters[a]	CH_2CO	CD_2CO
I_a	6.74	8.59
I_b	62.9	71.0
I_c	69.6	79.6
λ_a	0.95	0.95
λ_b	0.31	0.31
F	12.1	7.56
I_{top}	1.88	3.76
$A^{\ddagger\prime}$	3.35	3.26
$B^{\ddagger\prime}$	0.268	0.237
$C^{\ddagger}$	0.242	0.212

a. The units are amu*Å^2 for I_x (x=a,b,c,top) and cm^{-1} for F, $A^{\ddagger\prime}$, $B^{\ddagger\prime}$,and $C^{\ddagger}$. The *ab initio* (DZP CISD level calculation) C_s^{II} transition state structure is used for both CH_2CO and CD_2CO.

Table III. The energy levels and nuclear spin statistical weights of hindered internal rotor states coupled to different K quantum numbers for the CH_2CO transition state.[a]

m	K=0	K=1	K=2	K=3	K=4
0	0	(0)	0	(0)	0
-1	(0)	0	(0)	0	(0)
+1	(105)	105	(105)	105	(105)
-2	106	(106)	105	(105)	106
+2	196	(197)	200	(197)	196
-3	(206)	204	(200)	205	(206)
+3	(263)	267	(276)	265	(263)
-4	305	(292)	280	(296)	304
+4	325	(341)	360	(336)	327
-5	(415)	387	(366)	393	(410)
+5	(418)	448	(474)	441	(434)
-6	546	(509)	482	(517)	538
+6	546	(584)	616	(576)	554

a. The energy levels are in cm^{-1} and calculated when V_0 = 330 cm^{-1} and V_1 = -20 cm^{-1} in Eqs. (46)-(47). The energy values in parentheses are ortho states (I=1) and those without parentheses are para states (I=0). The rotational energy term values for (J,K) states are not included. The listed energy values in each column are those with respect to the corresponding zero-point energy levels.

Table IV. The energy levels and nuclear spin statistical weights of hindered internal rotor states coupled to different K quantum numbers for the CD_2CO transition state.[a]

m	K=0	K=1	K=2	K=3	K=4
0	(0)	0	(0)	0	(0)
-1	0	(0)	0	(0)	0
+1	84	(84)	84	(84)	84
-2	(85)	85	(84)	85	(85)
+2	(164)	164	(164)	164	(164)
-3	165	(164)	165	(165)	165
+3	231	(234)	231	(232)	233
-4	(240)	237	(239)	239	(238)
+4	(281)	290	(282)	284	(287)
-5	315	(297)	310	(306)	301
+5	329	(352)	335	(340)	346
-6	(397)	364	(384)	378	(370)
+6	(399)	435	(413)	420	(428)

a. The energy levels are in cm^{-1} and calculated when V_0 = 330 cm^{-1} and V_1 = -20 cm^{-1} in Eqs. (46)-(47). The energy values in parentheses are ortho states (I=2,0) and those without parentheses are para states (I=1). The rotational energy term values for (J,K) states are not included. The listed energy values in each column are those with respect to the corresponding zero-point energy levels.

Table V. The zero-point vibrational energies of ketene and methylene in the ground states.[a]

	CH_2CO	CD_2CO
$S_0(^1A_1)$[b]	6712	5556
TS[c]	5316	4221
$^3CH(D)_2$ fragment[d]	3495	2609

a. The unit is cm^{-1}.

b. Calculated from the values in Ref. 31.

c. Calculated from the scaled *ab initio* vibrational frequencies (See Table I.)

d. Calculated from the values in Ref. 45.

Table VI. The parameters used in the RRKM calculation for the fits to experimental results (the case of K-mixed).

	CH_2CO	CD_2CO
T_{rot}	4 K	4 K
E_{th}	28,250 cm^{-1}	28,305 cm^{-1}
ν_i [a]	100 *i* cm^{-1}	---
f [b]	1.40	1.88
V_0	330 cm^{-1}	330 cm^{-1}
V_1	-20 cm^{-1}	-20 cm^{-1}
$\nu_5^{\ddagger}$ ($CH(D)_2$ rock)	472 cm^{-1} [c]	340 cm^{-1}
$\nu_7^{\ddagger}$ (C-C-O bend)	240 cm^{-1}	190 cm^{-1}
$\nu_8^{\ddagger}$ ($CH(D)_2$ wag)	326 cm^{-1}	200 cm^{-1}

a. The imaginary frequency (ν_i) is used only for the fit to the first step in k(E) for CH_2CO dissociation.

b. $\rho(E) = \rho_{WR}(E) * f$; $\rho(E)$ is used for the RRKM fits. The $\rho_{WR}(E)$ is the density of vibrational states of reactant calculated from Whitten-Rabinovitch approximation; $\rho_{WR}(E) = 1.36 \times 10^4$ ($/cm^{-1}$) for CH_2CO (S_0) and 4.78×10^4 ($/cm^{-1}$) for CD_2CO (S_0) at E = 28,500 cm^{-1}.

c. The scaled *ab initio* vibrational frequency for ν_5 is listed. This is not important in RRKM calculation for measured rate constants in the 28,250 - 28,650 cm^{-1} region of the photolysis energy.

Table VII. The parameters used in the RRKM calculation for the fits to experimental results (the case of K-conserved).

	CH_2CO	CD_2CO
T_{rot}	4 K	4 K
E_{th}	28,250 cm^{-1}	28,315 cm^{-1}
ν_i [a]	100 *i* cm^{-1}	---
f [b]	1.67	2.14
V_0	240 cm^{-1}	230 cm^{-1}
V_1	20 cm^{-1}	20 cm^{-1}
$\nu_5^{\ddagger}$ ($CH(D)_2$ rock)	472 cm^{-1} [c]	340 cm^{-1}
$\nu_7^{\ddagger}$ (C-C-O bend)	250 cm^{-1}	180 cm^{-1}
$\nu_8^{\ddagger}$ ($CH(D)_2$ wag)	306 cm^{-1}	230 cm^{-1}

a. The imaginary frequency (ν_i) is used only for the fit to the first step in k(E) for CH_2CO dissociation.

b. $\rho(E) = \rho_{WR}(E) * f$; $\rho(E)$ is used for the RRKM fits. The $\rho_{WR}(E)$ is the density of vibrational states of reactant calculated from Whitten-Rabinovitch approximation; $\rho_{WR}(E) = 1.36 \times 10^4$ ($/cm^{-1}$) for CH_2CO (S_0) and 4.78×10^4 ($/cm^{-1}$) for CD_2CO (S_0) at E = 28,500 cm^{-1}.

c. The scaled *ab initio* vibrational frequency for ν_5 is listed. This is not important in RRKM calculation for measured rate constants in the 28,250 - 28,650 cm^{-1} region of the photolysis energy.

Table VIII. The energy levels and nuclear spin statistical weights of hindered internal rotor states coupled to different K quantum numbers for the CH_2CO and CD_2CO transition states.[a]

	CH_2CO			CD_2CO		
m	K=0	K=1	K=2	K=0	K=1	K=2
0	0	(0)	0	(0)	0	(0)
-1	(0)	0	(0)	0	(0)	0
+1	(99)	100	(101)	82	(82)	82
-2	103	(103)	101	(83)	82	(83)
+2	164	(167)	172	(145)	147	(145)
-3	(189)	182	(174)	151	(148)	150
+3	(209)	219	(233)	183	(190)	185
-4	276	(254)	238	(212)	196	(206)
+4	278	(302)	323	(220)	240	(226)
-5	(383)	352	(329)	278	(250)	266
+5	(383)	415	(441)	278	(309)	291
-6	514	(477)	449	(358)	323	(344)
+6	514	(553)	585	(358)	396	(374)

a. The energy levels are in cm^{-1} and calculated when (V_0 = 240, V_1 = 20 cm^{-1}) for CH_2CO; (V_0 = 230, V_1 = 20 cm^{-1}) for CD_2CO. The energy values in parentheses are ortho states and those without parentheses are para states. The rotational energy term values for (J,K) states are not included. The listed energy values in each column are those with respect to the corresponding zero-point energy levels.

Figure 1. The three lowest potential energy surfaces of ketene along the reaction coordinate. The ketene molecule is excited by a UV laser pulse to the first excited singlet state (S_1), undergoes the internal conversion to S_0 or intersystem crossing to T_1, and dissociates into $^1CH_2$ + CO (Singlet Channel) or $^3CH_2$ + CO (Triplet Channel) fragments.

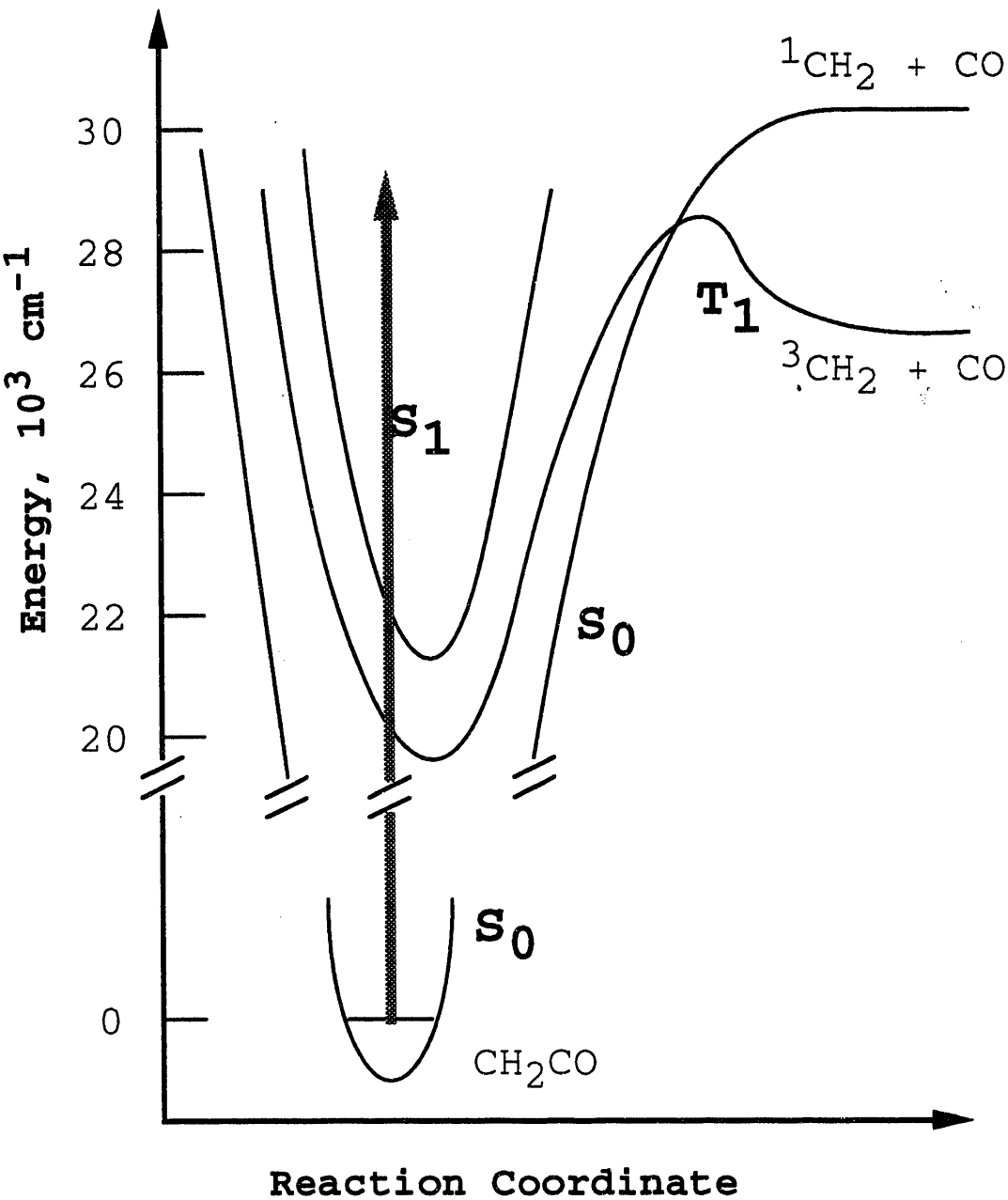
Energy, 10^3 cm^{-1}
30
28
26
24
22
20
0
$^1CH_2$ + CO
T_1
$^3CH_2$ + CO
S_1
S_0
S_0
CH_2CO
Reaction Coordinate

Figure 2. Cross section of the VUV LIF detection geometry in the molecular beam chamber. The cultured quartz (C.Q.) window is used in front of the VUV PMT to reduce the scattered light. For the rate constant measurements for the slow reactions, the expanded pump laser is overlapped with the VUV probe laser in the downstream of the molecular jet. The distances of PMT and the orifice of the nozzle from the interaction region are about 5 cm and 3 cm, respectively. The diameters of UV pump and VUV probe lasers are about 1 cm and 4 mm, respectively.

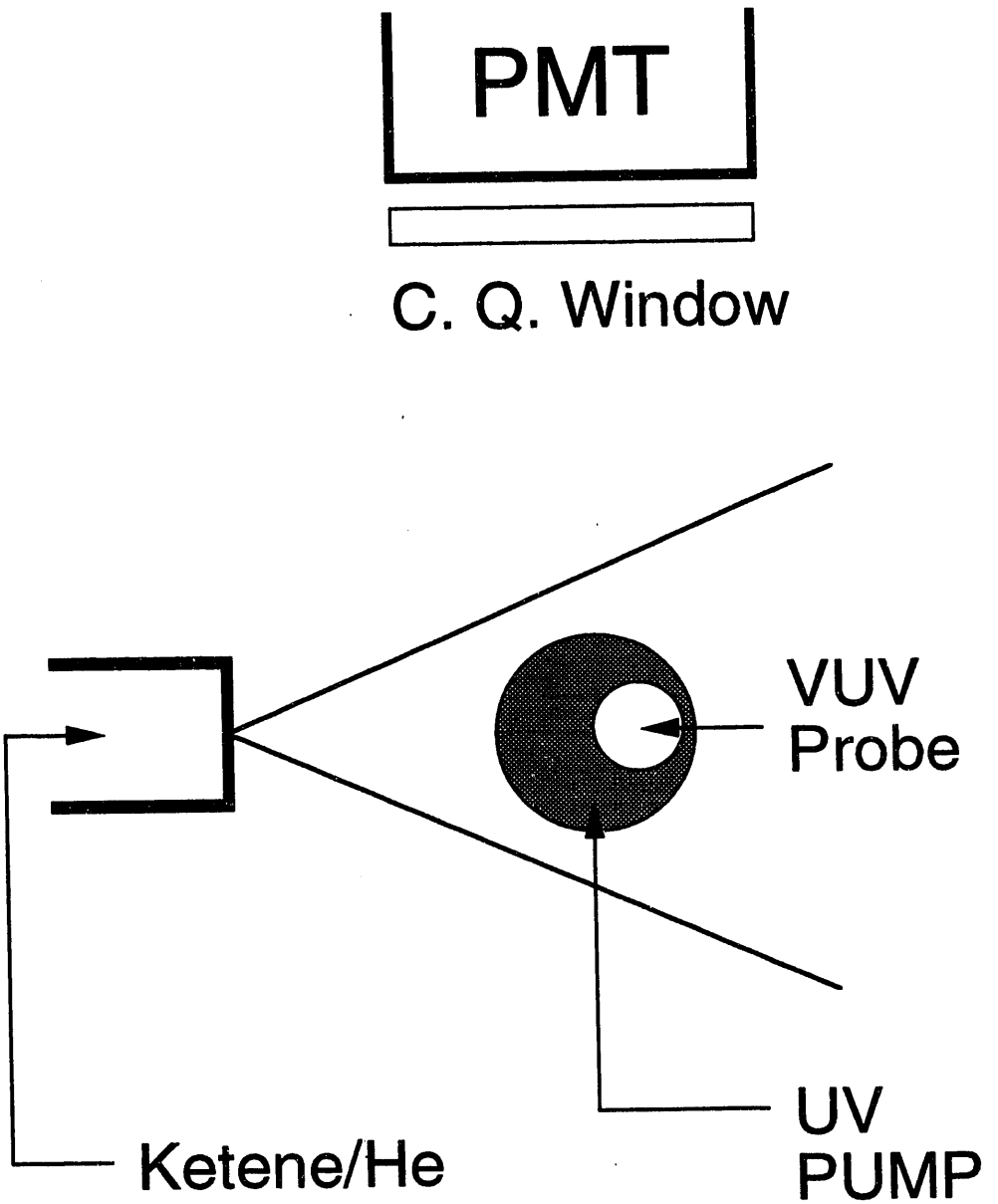
PMT
C. Q. Window
VUV
Probe
UV
PUMP
Ketene/He

Figure 3. The CO product rotational distributions from the dissociations of ketene. The solid lines are the fits calculated by the same method described in Ref. 18: (a) from the CH_2CO dissociation at 28,450 cm^{-1}, 1μs; (b) from the CD_2CO dissociation at 28,410 cm^{-1}, 1μs.

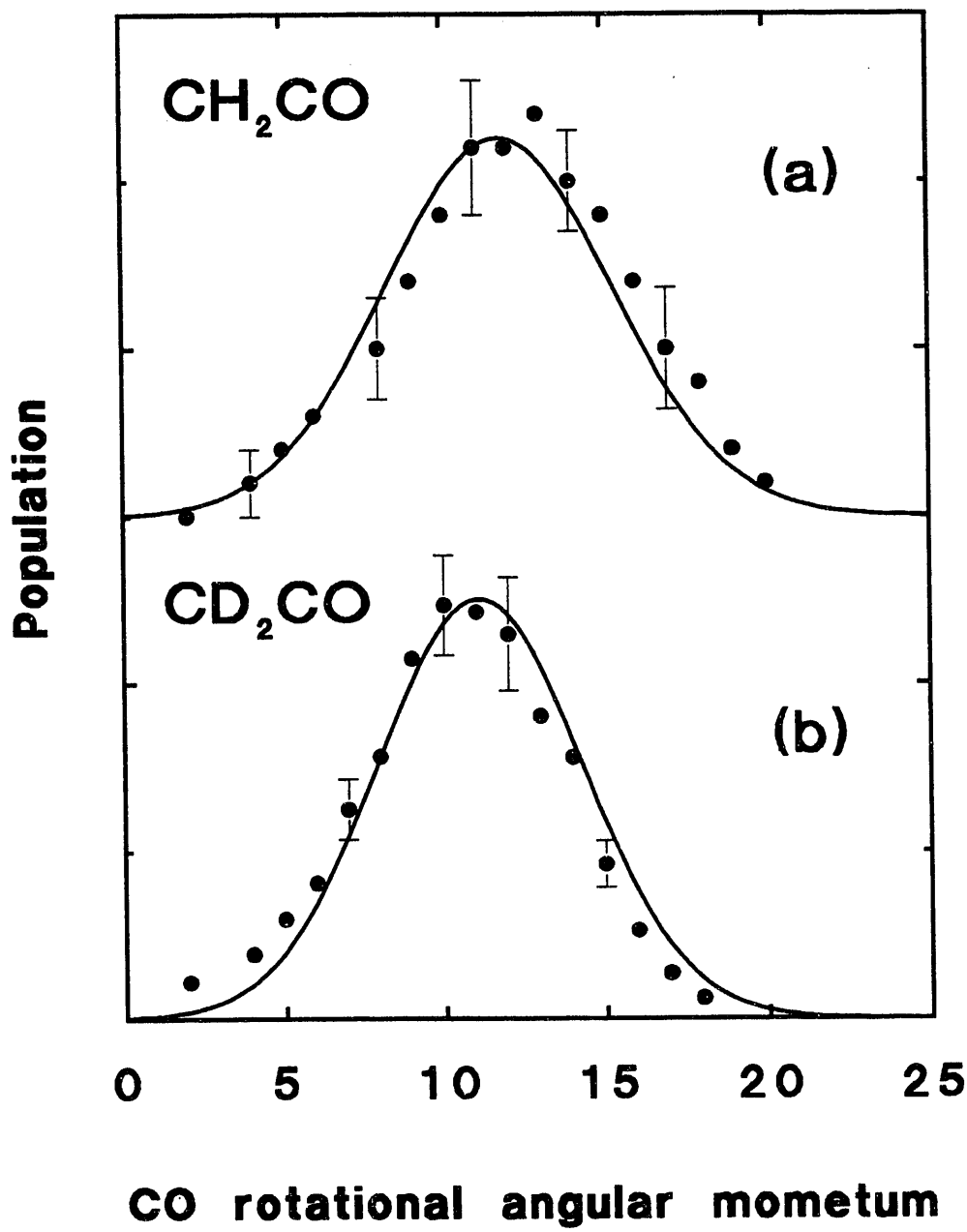
CH2CO
(a)
CD2CO
(b)
Population
0
5
10
15
20
25
CO rotational angular mometum

Figure 4. The CO product rise curves from the CD_2CO dissociation at 28,900 cm^{-1} ($k \approx 3 \times 10^7$ s^{-1}). (a) the CO rise curve for the Q(6) transition; (b) the CO rise curve for the Q(12) transition; (c) the ratio of the CO rise curves for the Q(6) transition to that for the Q(12) transition. The VUV LIF intensity of the Q(6) transition is about 5 times less than that of the Q(12) transition. The delay time where the rotational relaxation starts is marked as an arrow in (c).

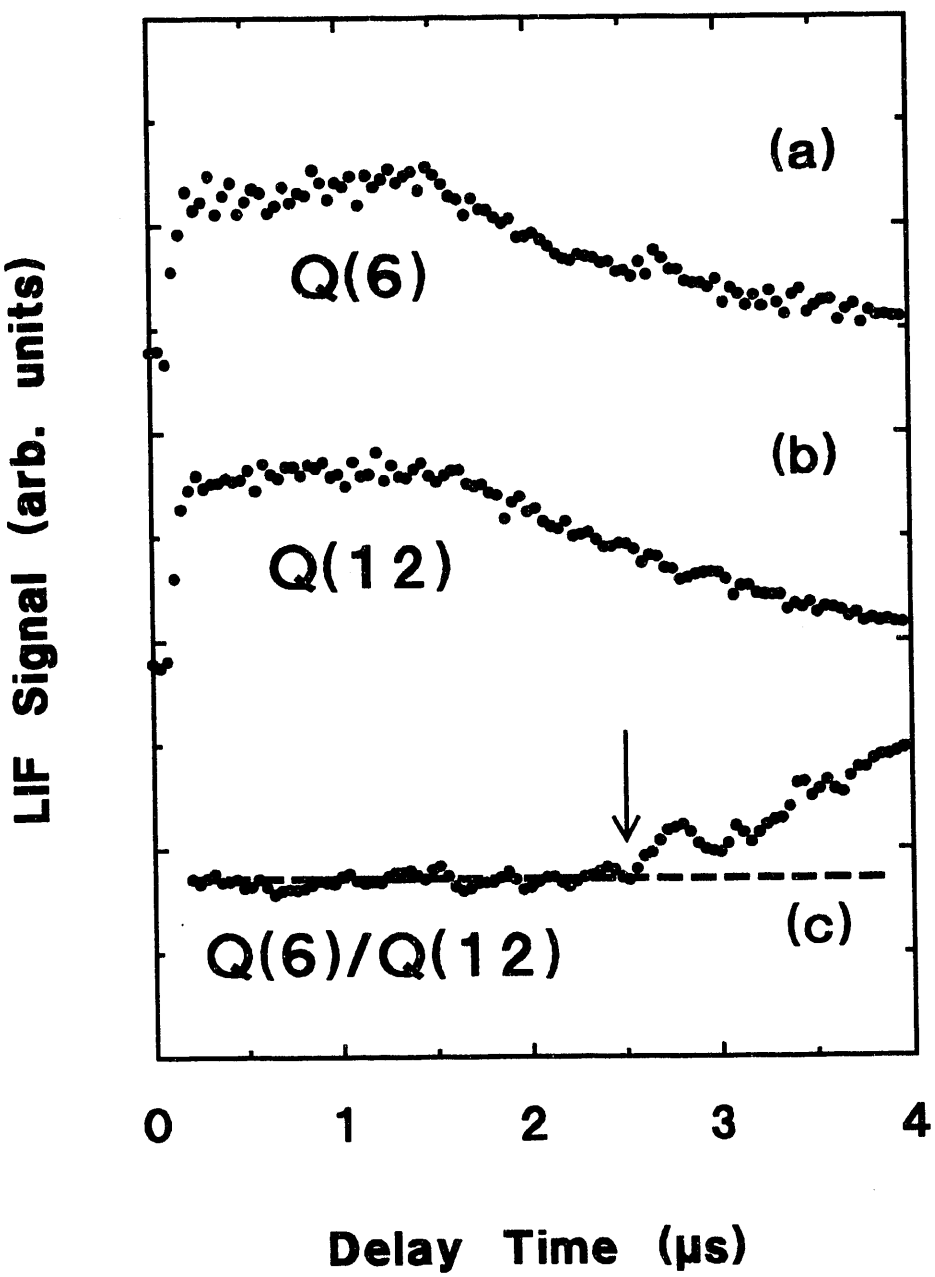
(a)
Q(6)
(b)
Q(12)
(c)
Q(6)/Q(12)
LIF Signal (arb. units)
0
1
2
3
4
Delay Time (μs)

Figure 5. The CO product rise curves for the Q(12) transition of CO products from CH_2CO and CD_2CO dissociations. The single exponential fits are shown as solid lines. (a) CH_2CO at 28,423 cm^{-1}, k = 1.1 x 10^7 s^{-1}; (b) CD_2CO at 28,500 cm^{-1}, k = 3.6 x 10^6 s^{-1}.

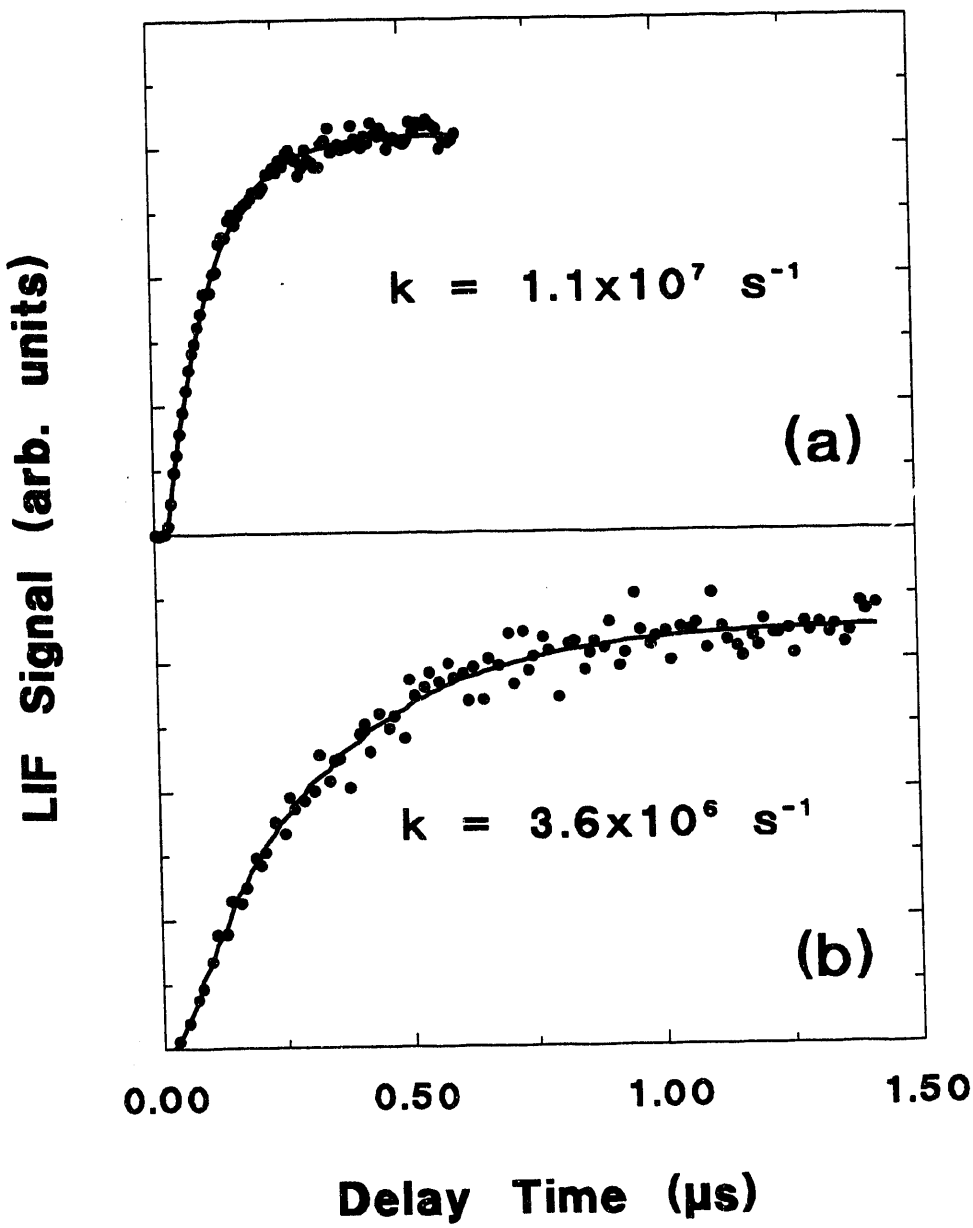
k = 1.1x10⁷ s⁻¹
(a)
k = 3.6x10⁶ s⁻¹
(b)
LIF Signal (arb. units)
0.00
0.50
1.00
1.50
Delay Time (μs)

Figure 6. The rate constants for CH_2CO dissociation as a function of the photolysis energy. The error bars on selected data points represent two times of the standard deviation calculated from three differently measured rate constants at each photolysis energy.

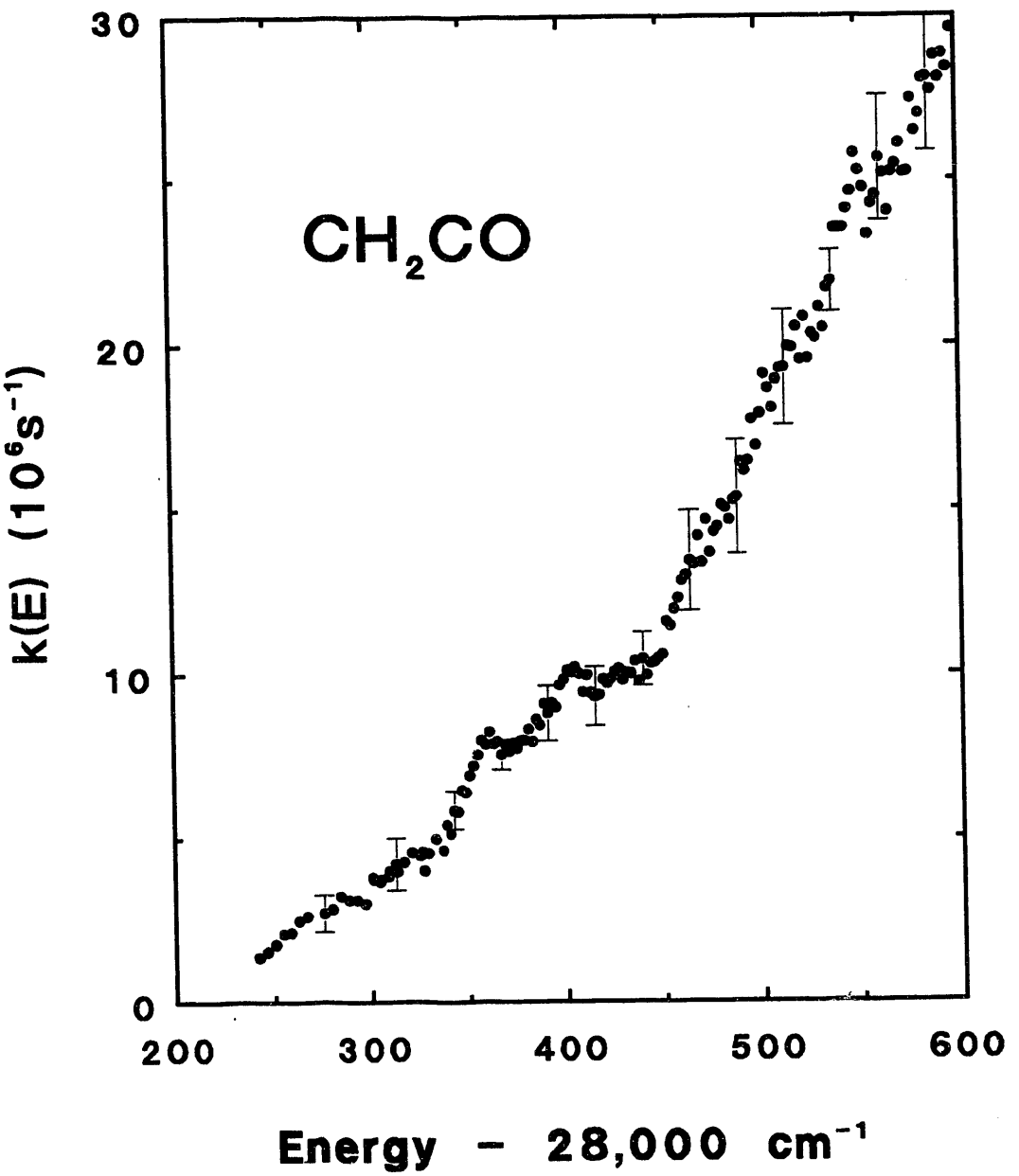
CH2CO
k(E) (10^6 s^-1)
0
10
20
30
200
300
400
500
600
Energy - 28,000 cm^-1

Figure 7. The rate constants of the CD_2CO dissociation as a function of the photolysis energy.

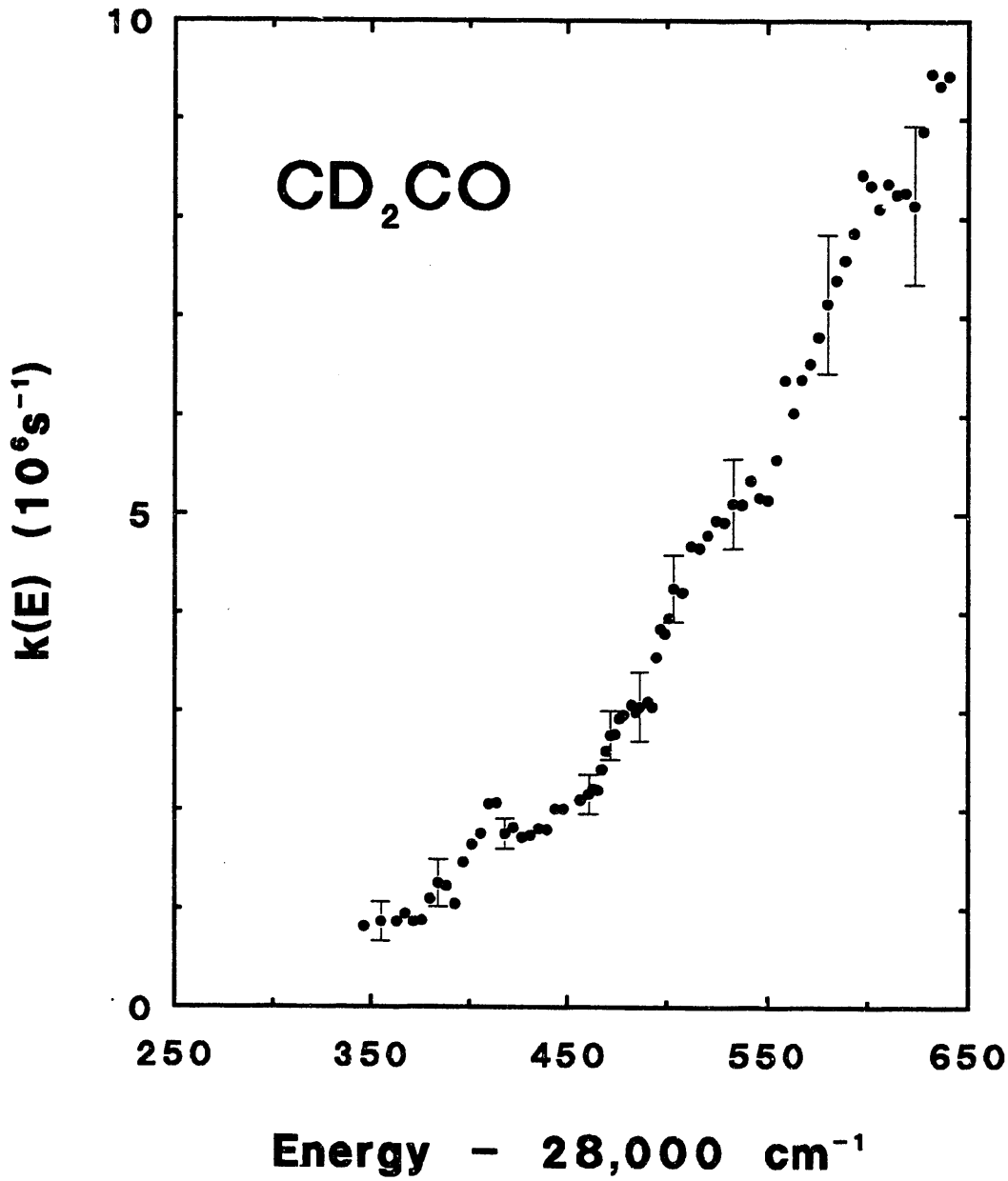
CD2CO
k(E) (10^6 s^-1)
10
5
0
250
350
450
550
650
Energy - 28,000 cm^-1

Figure 8. PHOFEX curves for the Q(12) and Q(2) transitions and the simulated PHOFEX curve from the measured rate constants for the CH_2CO dissociation. (a) The PHOFEX curve for the Q(12) transition of CO, taken at 50 ns; (b) The simulated PHOFEX curve using the measured rate constants, [1-exp(-k(E)*Δt)], where Δt = 50 ns; (c) The PHOFEX curve for the Q(2) transition of CO, taken at 50 ns. The actual ratio of the yields of CO(v=0,J=12) to CO(v=0,J=2) is about 20:1 at 28,500 cm^{-1}. The simulated PHOFEX curve in (b) is scaled to compare the Q(12) PHOFEX curve in (a).

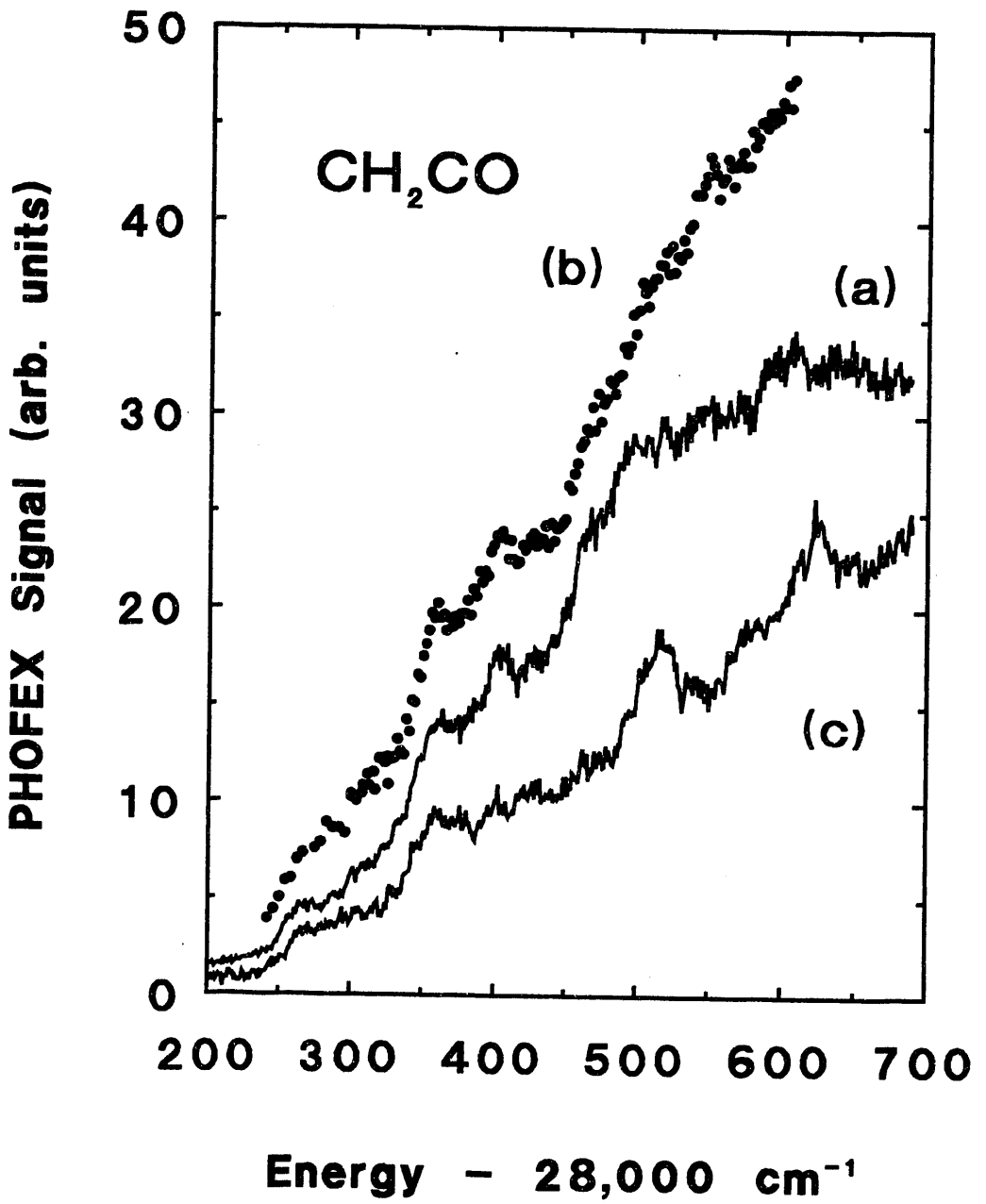
50
40
30
20
10
0
CH2CO
(b)
(a)
(c)
PHOFEX Signal (arb. units)
200 300 400 500 600 700
Energy – 28,000 cm-1

Figure 9. PHOFEX curves for the Q(12) and Q(2) transitions and the simulated PHOFEX curve from the measured rate constants for the CD_2CO dissociation. (a) The PHOFEX curve for the Q(12) transition of CO, taken at 200 ns; (b) The simulated PHOFEX curve using the measured rate constants, $[1-\exp(-k(E)*\Delta t)]$, where Δt = 200 ns; (c) The PHOFEX curve for the Q(2) transition of CO, taken at 150 ns. See the caption for Figure 8.

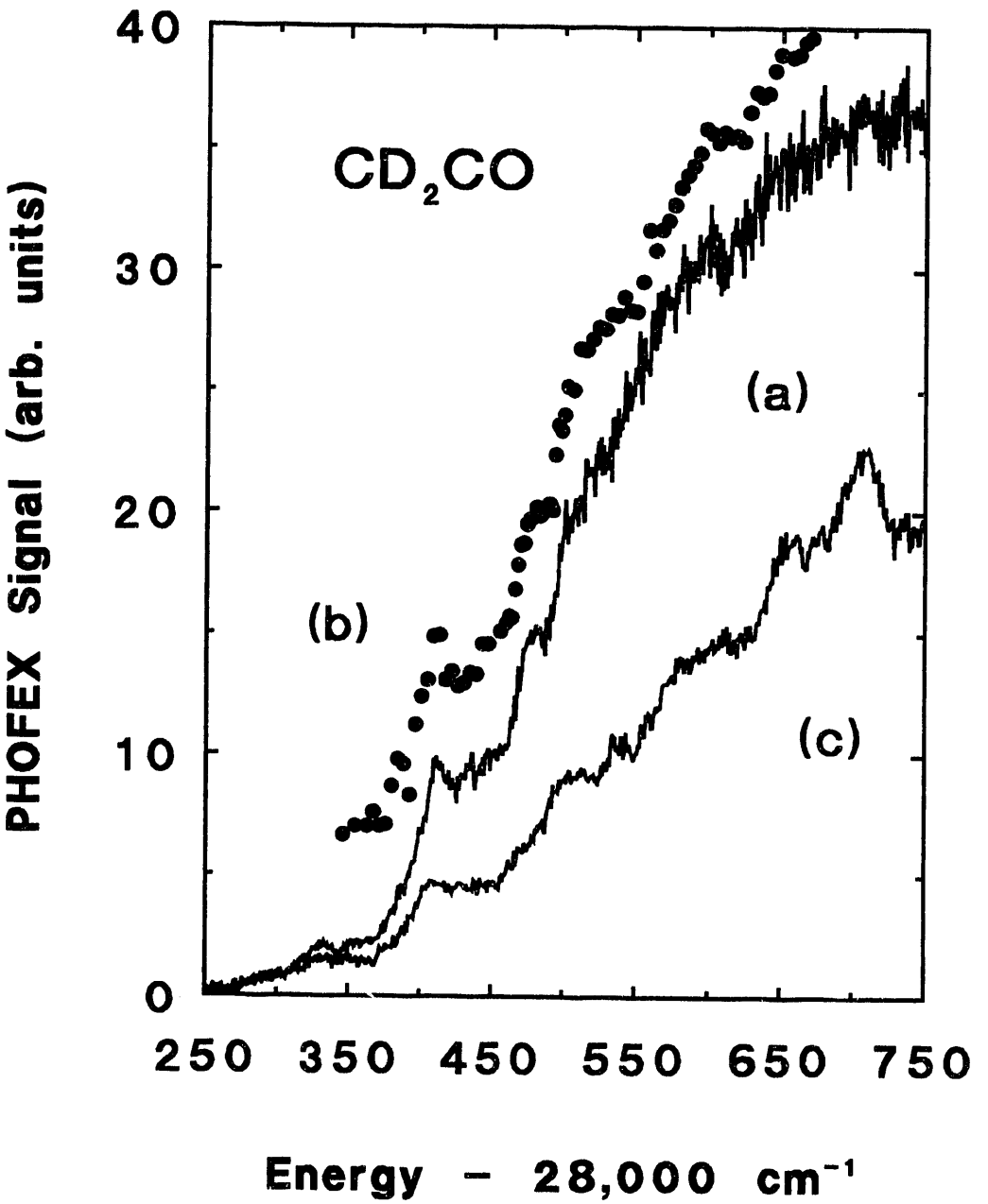
40
30
20
10
0
CD2CO
(a)
(b)
(c)
PHOFEX Signal (arb. units)
250 350 450 550 650 750
Energy – 28,000 cm-1

Figure 10. The geometries of ketene at reactant state, transition state, and product states. For the *ab initio* structures for the C_s^{II} or C_s^{I} transition states of ketene (DZP CISD level calculation), see Ref. 23.

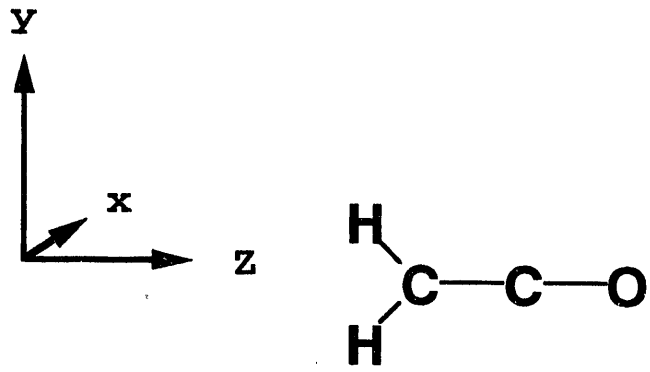

Reactant

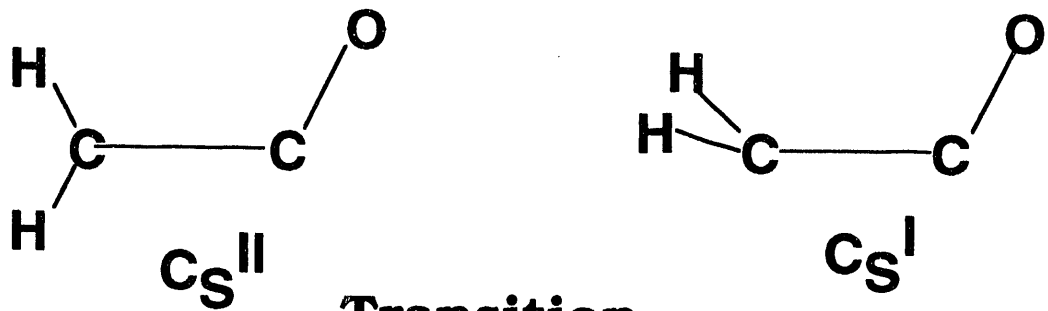

Transition State

Products

Figure 11. The model potential function for the hindered internal rotor, $V = (1/2)*V_0*(1-\cos 2\theta) + (1/2)*V_1*(1-\cos 4\theta)$, where V_0 = 330 cm^{-1} and V_1 = ± 20 cm^{-1}. The effect of the parameter V_1 is shown.

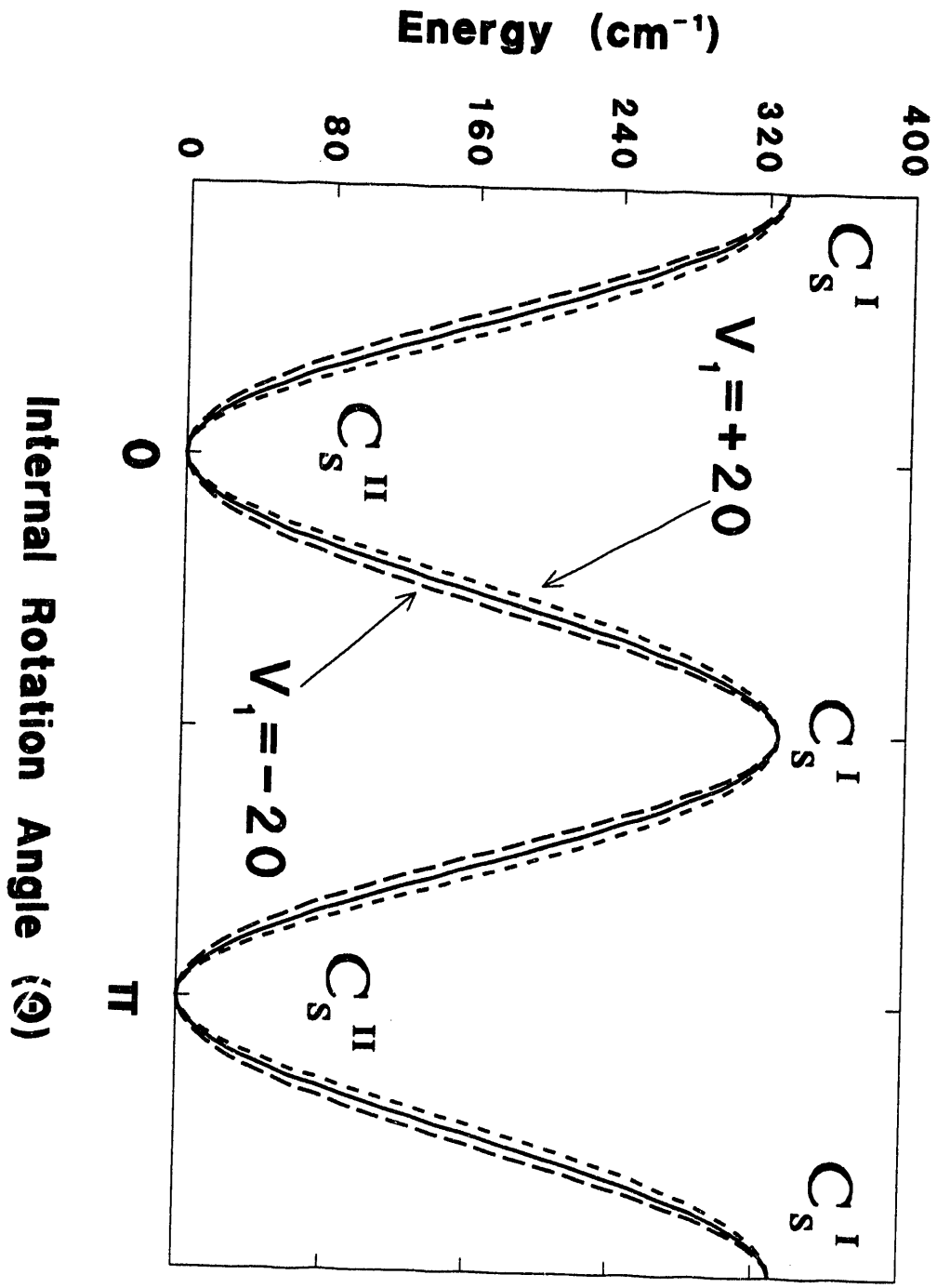
Energy (cm⁻¹)
0
80
160
240
320
400
C_s^I
C_s^{II}
$V_1 = +20$
$V_1 = -20$
0
π
Internal Rotation Angle (Φ)

Figure 12 (a). The RRKM fit for CH_2CO dissociation in the reaction threshold region. The solid line is the RRKM fit when the threshold energy is 28,250 cm^{-1} and ν_i = 100 i cm^{-1}. The RRKM fits for the different imaginary frequencies are shown as the dashed line (ν_i = 60 cm^{-1}) and the dotted line (ν_i = 140 cm^{-1}) at the same threshold energy. The CO(v=0,J=12; 50ns) PHOFEX curve is shown as open circles. Intensity of the PHOFEX curve is scaled for the comparison with rate constants.

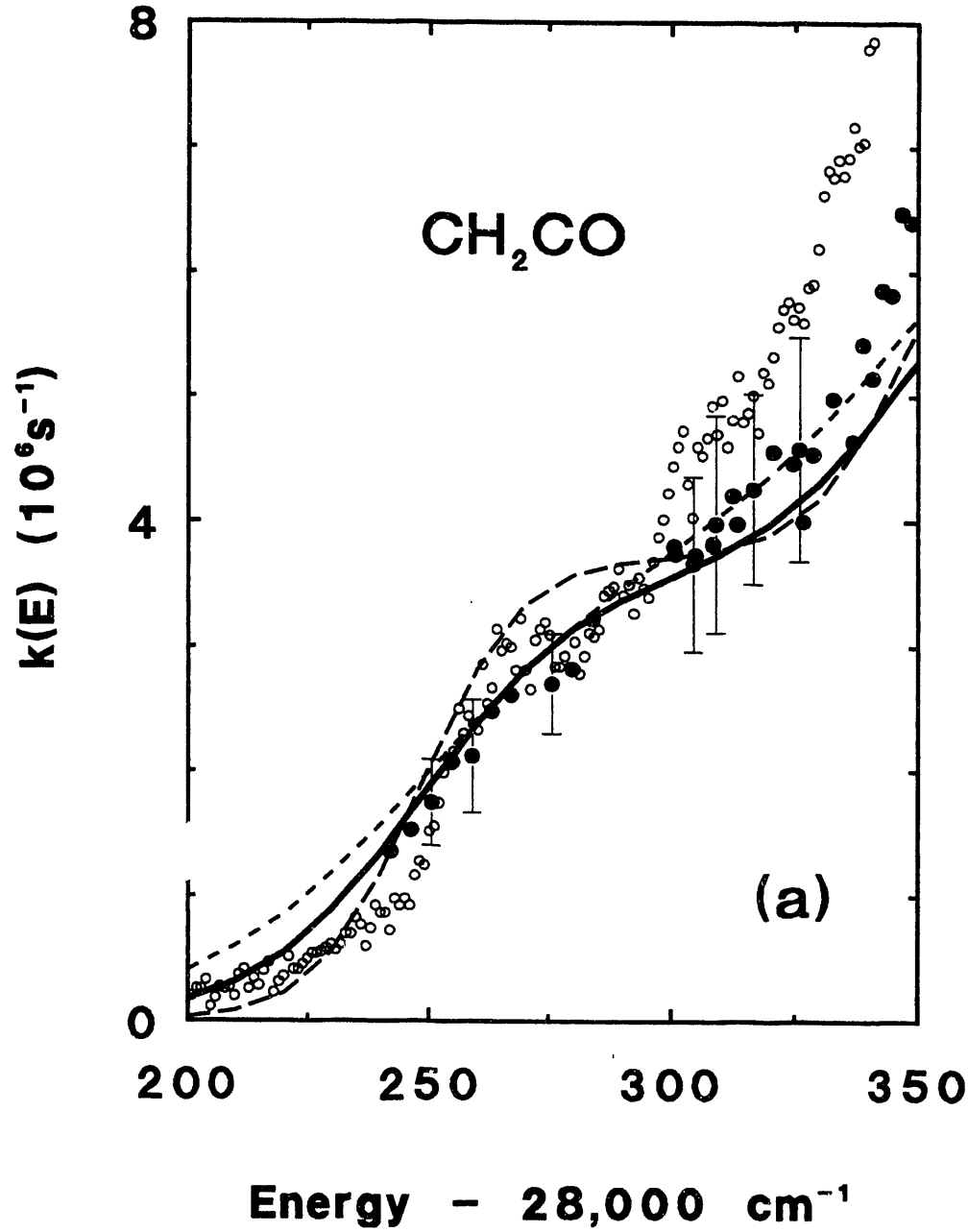
8
4
0
CH_2CO
(a)
k(E) ($10^6 s^{-1}$)
200
250
300
350
Energy – 28,000 cm^{-1}

Figure 12 (b). The RRKM fit for the CD_2CO dissociation in the reaction threshold region. The data points of the Q(12) PHOFEX curve taken at 1.7 μs reaction time are shown as open circles. The solid line is the RRKM fit when the threshold energy is 28,310 cm^{-1}. The dashed line is the RRKM fit when ν_i = 60 i cm^{-1}.

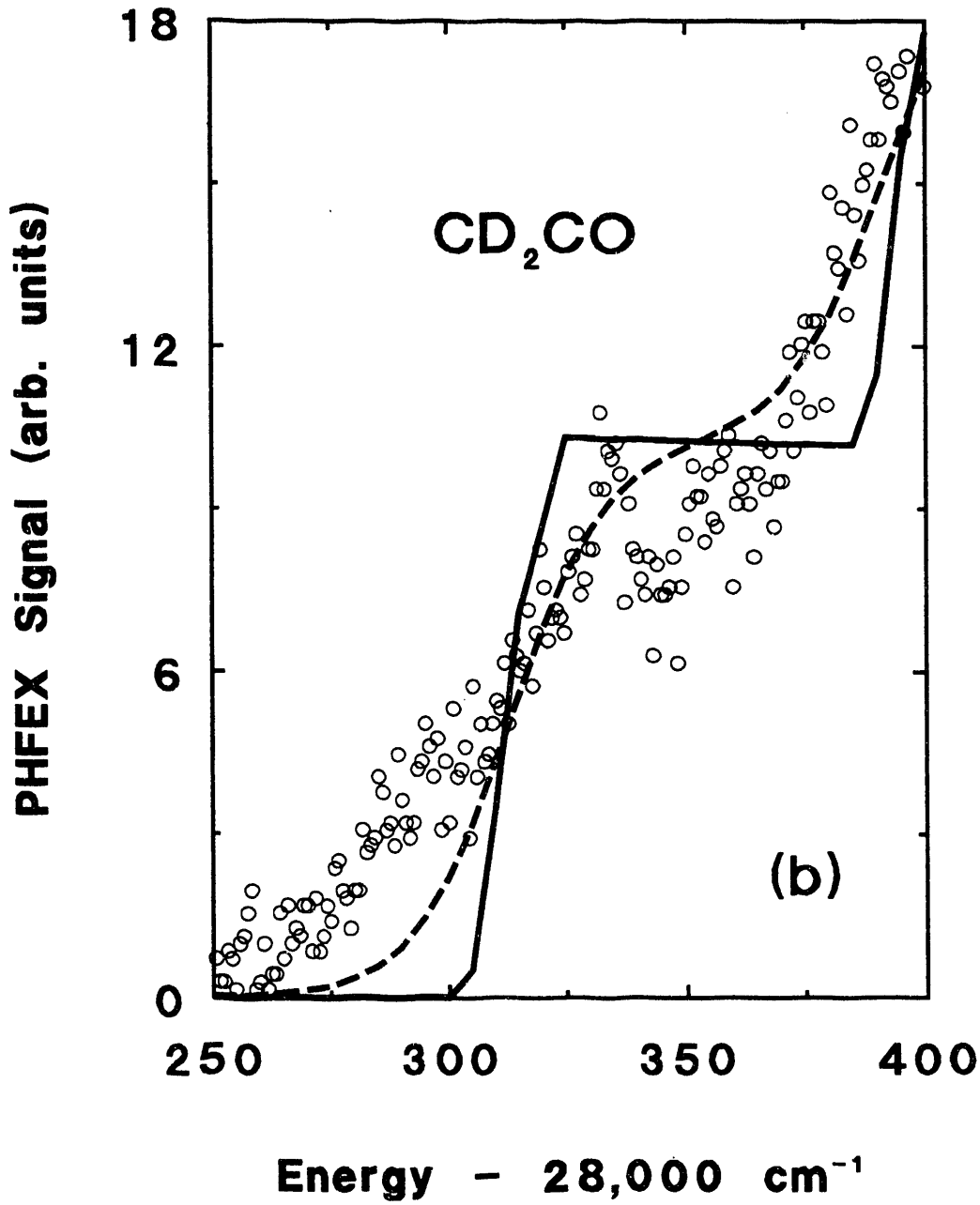
18
12
6
0
PHFEX Signal (arb. units)
CD2CO
(b)
250
300
350
400
Energy - 28,000 cm-1

Figure 13. The energetic diagram for the dissociation of CH_2CO and CD_2CO on the triplet surfaces. The energy differences among the zero-point energy levels are shown. The energies are in cm^{-1}. See the text for the uncertainties of the energy values.

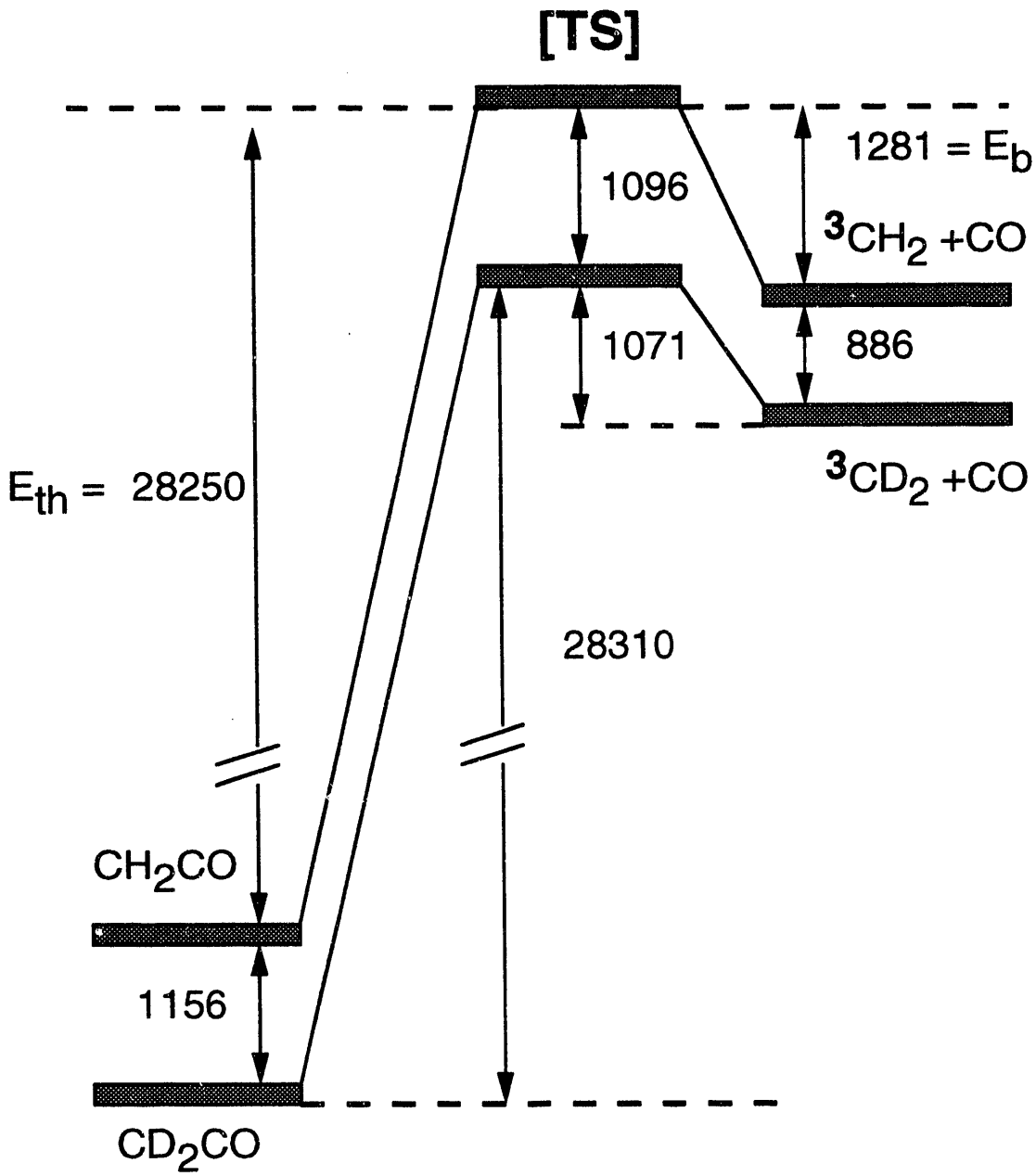
[TS]
1281 = E_b
1096
$^3CH_2$ +CO
1071
886
$^3CD_2$ +CO
E_{th} = 28250
28310
CH_2CO
1156
CD_2CO

Figure 14. (a) The ratio of the Q(2) PHOFEX curve to the Q(12) PHOFEX curve. Both PHOFEX curves are taken at 50 ns of the reaction times. (b) The calculated ratio of the yields of CO(J=2) to CO (J=12) products using the model described in the text when the vibrational frequency for the C-C-O bend is 250 cm^{-1}.

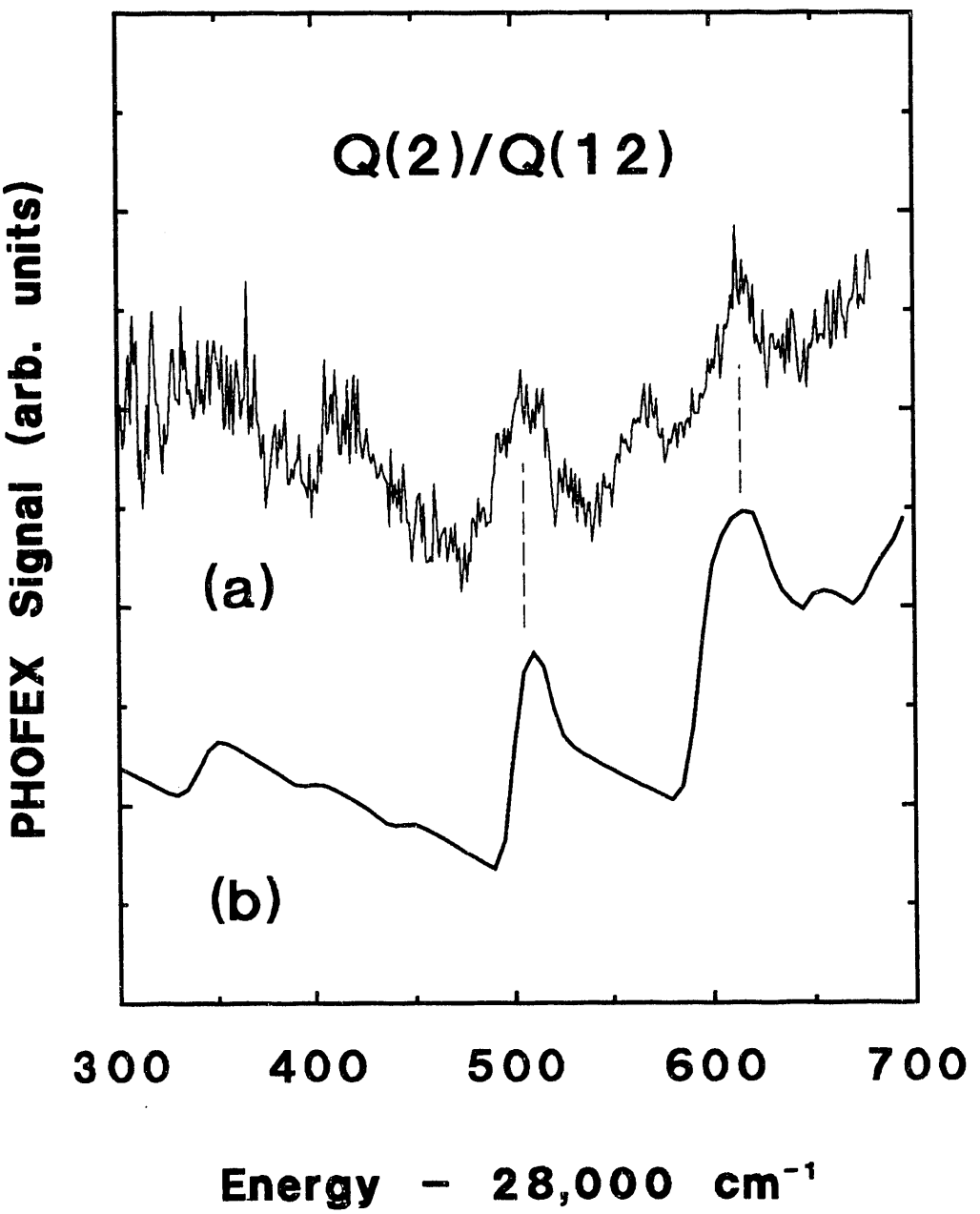
Q(2)/Q(12)
(a)
(b)
PHOFEX Signal (arb. units)
300
400
500
600
700
Energy - 28,000 cm⁻¹

Figure 15 (a). The RRKM fit to rate constants of the CH_2CO dissociation for the case of the complete K-mixing. The open circles are measured rate constants. The solid line is the RRKM fit using a step function for the transmission probability. The dashed line is the RRKM fit including the one-dimensional tunneling with an imaginary frequency of 100 i cm^{-1}. The parameters listed in Table VI are used for the RRKM fit.

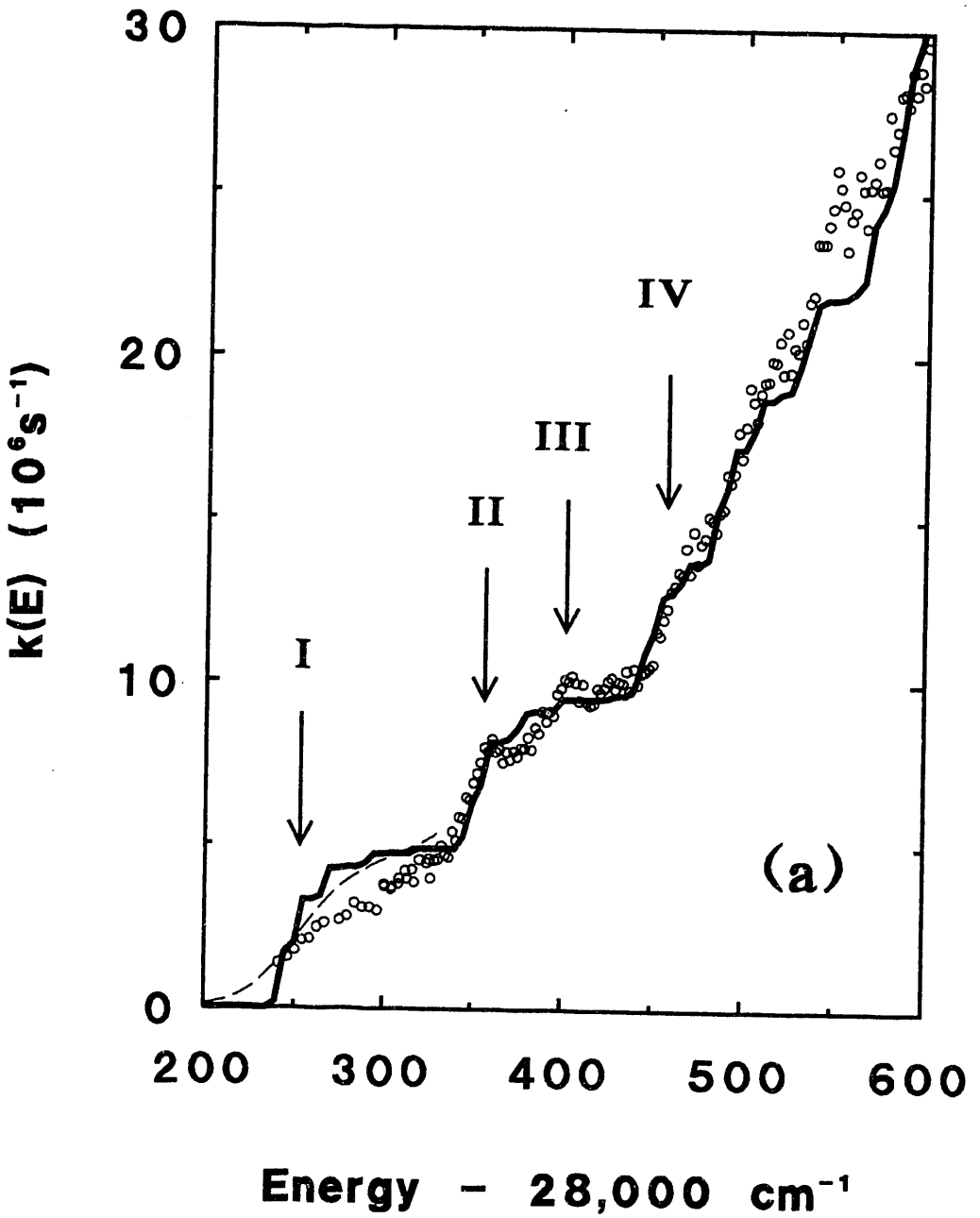
30
20
10
0
k(E) (10⁶s⁻¹)
I
II
III
IV
(a)
200
300
400
500
600
Energy - 28,000 cm⁻¹

Figure 15 (b). The RRKM fit to rate constants of the CH_2CO dissociation for the case of the complete K-mixing. The open circles are measured rate constants. The solid line is the RRKM fit including the one-dimensional tunneling with an imaginary frequency of 40 i cm^{-1}. The RRKM parameters are listed in Table VI. The dotted line is the RRKM fit using a step function.

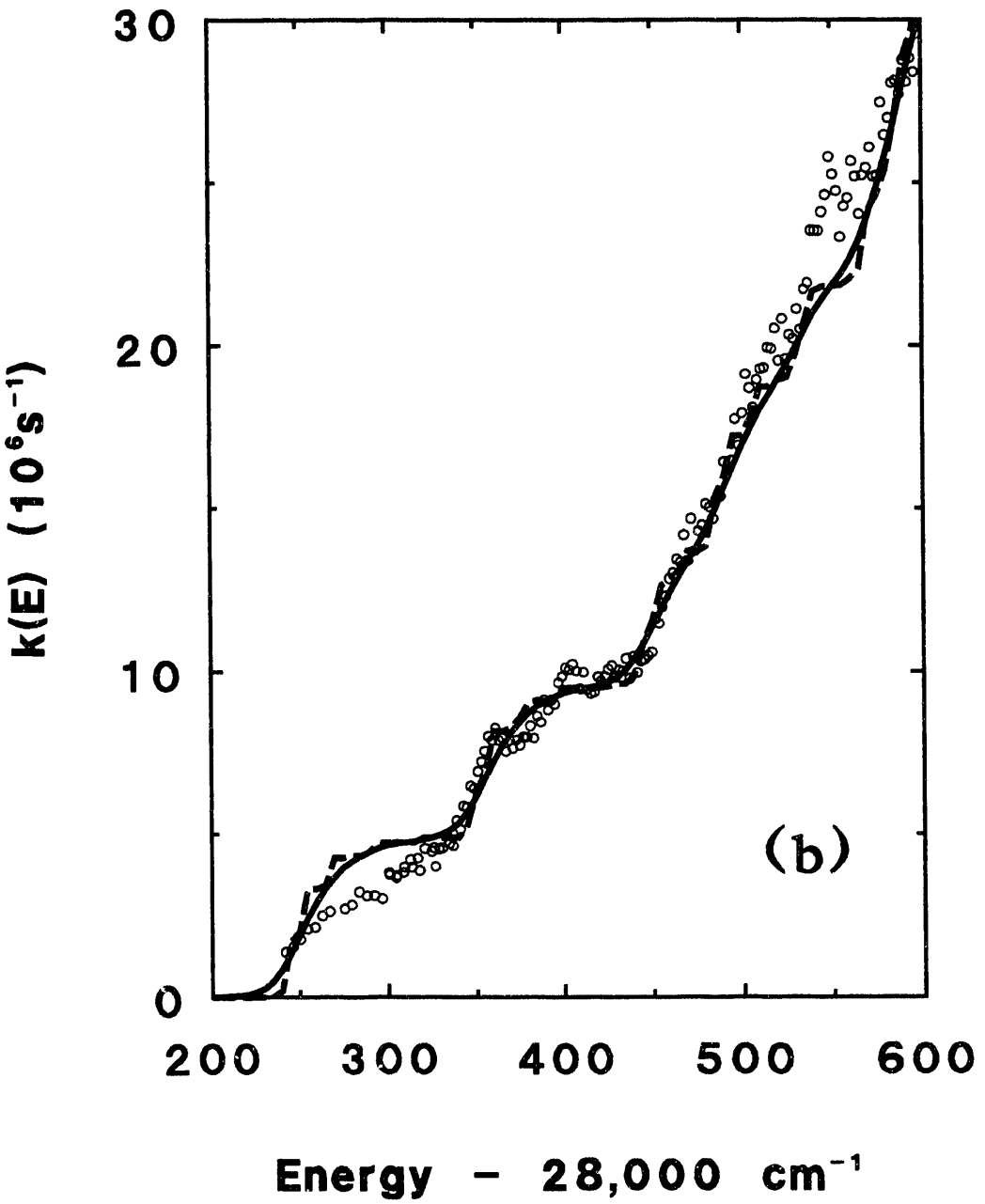
30
20
10
0
k(E) (10⁶s⁻¹)
200
300
400
500
600
Energy - 28,000 cm⁻¹
(b)

Figure 16. The RRKM fit to the rate constants of the CD_2CO dissociation for the case of the complete K-mixing. The step function is used as the transmission probability. The open circles are measured rate constants and the solid line is the RRKM fit. The RRKM parameters listed in Table VI are used.

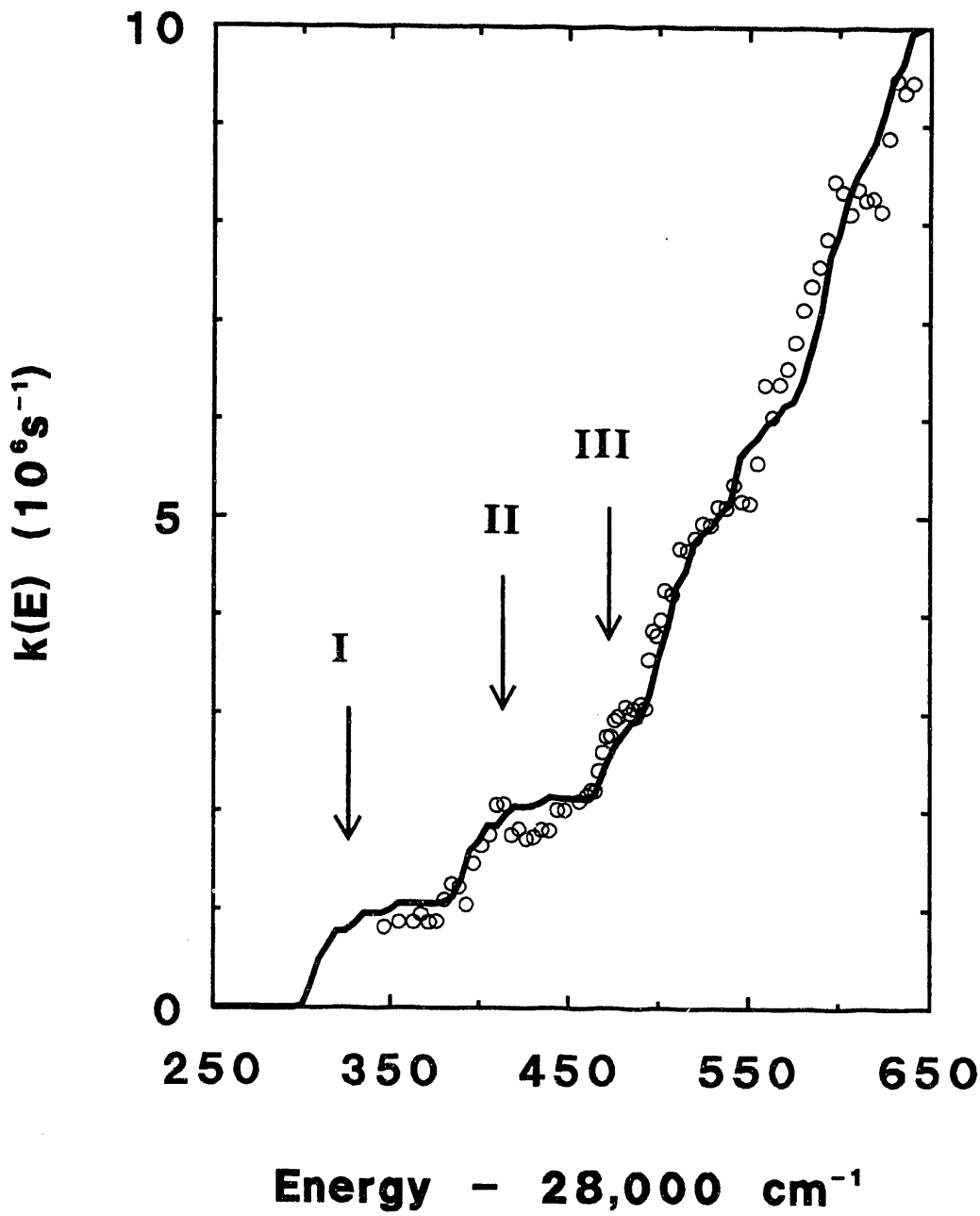
10
5
0
k(E) (10⁶s⁻¹)
I
II
III
250
350
450
550
650
Energy – 28,000 cm⁻¹

Figure 17. The RRKM fit to rate constants of the CH_2CO dissociation for the case of K-conserved. The step function is used as the transmission probability. The RRKM parameters are listed in Table VII.

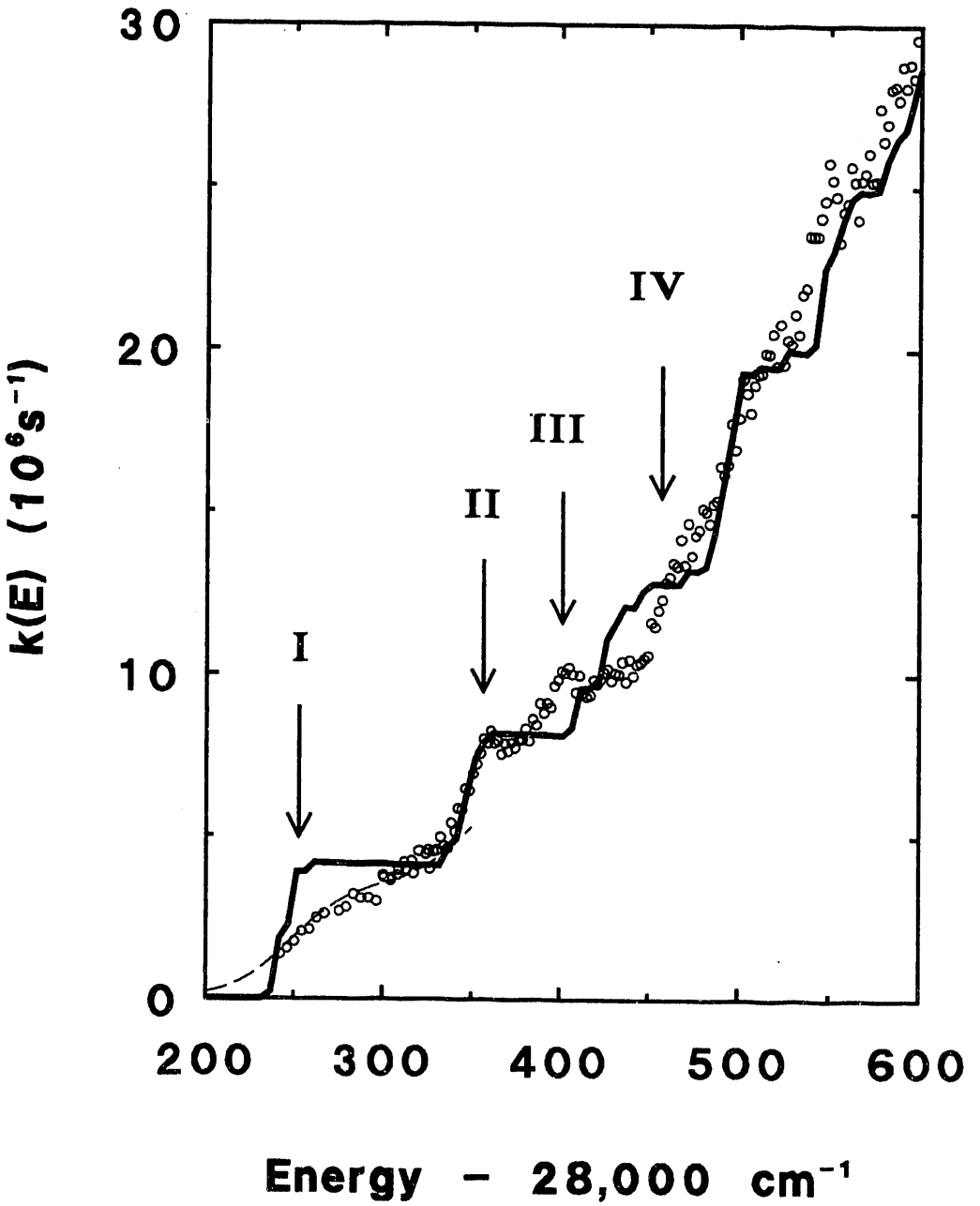
30
20
10
0
200
300
400
500
600
k(E) (10⁶s⁻¹)
Energy - 28,000 cm⁻¹
I
II
III
IV

Figure 18. The RRKM fit to rate constants of the CD_2CO dissociation for the case of K-conserved. The step function is used as the transmission probability. The RRKM parameters are listed in Table VII. The dotted line is the CO(v=0,J=12;200 ns) PHOFEX curve. The intensity of the PHOFEX curve is scaled for the comparison with the RRKM fit.

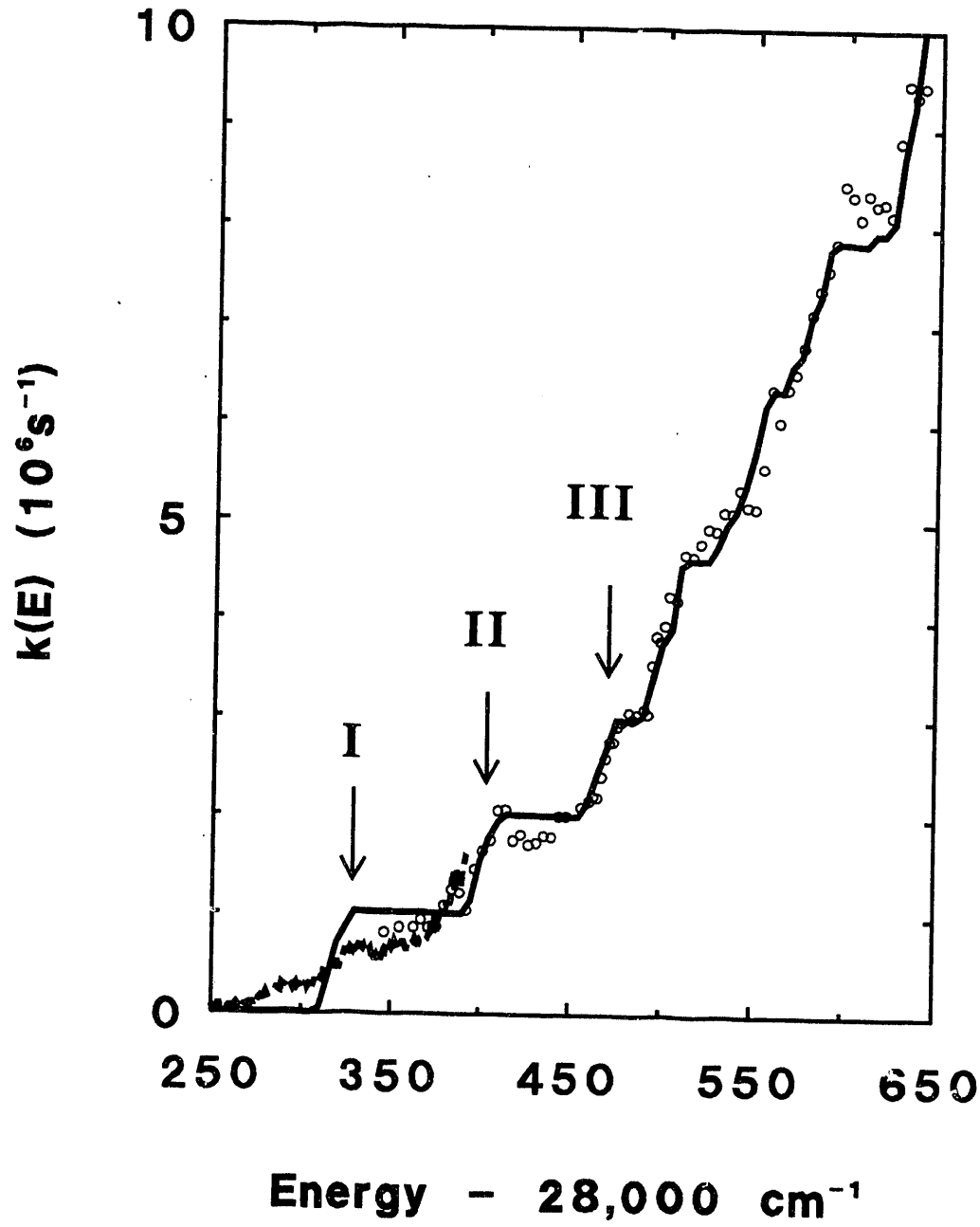
10
5
0
k(E) (10⁶s⁻¹)
I
II
III
250
350
450
550
650
Energy - 28,000 cm⁻¹

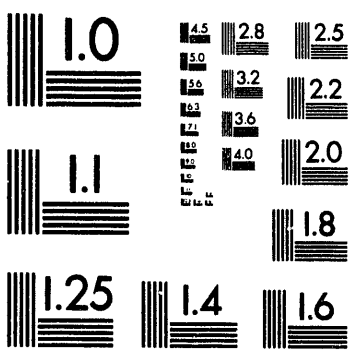
1.0
1.1
1.25
1.4
1.6
1.8
2.0
2.2
2.5
2.8
3.2
3.6
4.0
4.5
5.0
5.6
6.3
7.1
8.0
9.0
10
11
12
13
14
16
18
20
22
25
28
32
36
40
45
50
56
63
71
80
90
100
110
125
140
160
180
200
220
250
280
320
360
400
450
500
560
630
710
800
900
1000

3 of 3

Appendix 1. - rate constants for the CH_2CO and CD_2CO dissociation.

CH_2CO		CD_2CO	
E-28,000 cm^{-1}	k(10^5 s^{-1})	E-28,000 cm^{-1}	k(10^5 s^{-1})
606.3	313.98	670.8	115.50
604.3	291.27	666.4	113.20
602.2	309.31	662.1	108.00
600.2	292.01	657.8	107.20
598.1	296.01	649.2	108.30
596.1	283.99	644.9	102.10
594.1	288.27	640.6	94.40
592.0	281.00	636.3	93.40
590.0	287.67	632.0	94.60
587.9	277.27	627.7	88.80
585.9	281.32	623.4	81.30
583.8	280.67	619.1	82.60
581.8	270.02	614.8	82.40
579.8	264.73	610.5	83.50
577.7	274.73	606.2	81.00
575.7	252.29	601.9	83.30
573.6	252.00	597.6	84.40
571.6	260.98	593.3	78.50
569.6	254.68	589.0	75.70
567.5	252.29	584.7	73.70
565.5	240.33	580.4	71.30
563.4	252.00	576.1	68.00
561.4	256.68	571.8	65.25
559.4	245.30	567.6	63.70
557.3	242.72	563.3	60.30
555.3	233.29	559.0	63.60
553.2	247.51	554.7	55.60
551.2	252.70	550.4	51.50
549.2	257.99	546.1	51.70
547.1	246.32	541.9	53.40
545.1	240.99	537.6	51.00
543.0	235.29	533.3	51.10
541.0	235.29	529.0	49.20
539.0	235.29	524.8	49.40
536.9	219.28	520.5	47.90
534.9	217.32	516.2	46.60
532.9	205.02	512.0	46.80
530.8	211.30	507.7	42.10

528.8	202.02	503.4	42.50
526.8	203.28	501.3	39.50
524.7	195.70	499.2	37.90
522.7	208.31	497.0	38.40
520.7	195.30	494.9	35.50
518.6	205.31	492.7	30.50
516.6	199.02	490.6	31.00
514.6	199.30	486.4	30.50
512.5	193.02	484.3	30.00
510.5	192.71	482.1	30.70
508.5	189.32	477.9	29.70
506.4	180.72	475.8	29.30
504.4	186.68	473.6	27.70
502.4	190.99	471.5	27.60
500.3	179.02	469.3	26.00
498.3	169.32	467.2	24.10
496.3	177.30	465.1	22.00
494.3	164.70	463.0	22.10
492.2	161.70	460.8	21.60
490.2	164.29	456.6	21.00
488.2	153.71	448.1	20.10
486.1	152.69	443.8	20.10
484.1	146.69	439.6	18.00
482.1	150.31	435.3	18.10
480.0	151.29	431.1	17.40
478.0	144.71	426.9	17.20
476.0	142.99	422.6	18.20
474.0	136.71	418.4	17.60
471.9	146.69	414.1	20.70
469.9	133.69	409.9	20.60
467.9	141.71	405.9	17.60
465.9	133.29	401.4	16.50
463.8	134.31	397.2	14.70
461.8	129.99	393.0	10.50
459.8	128.29	388.7	12.30
457.8	123.00	384.5	12.60
455.7	119.70	380.3	11.00
453.7	114.71	376.0	8.80
451.7	116.01	371.8	8.70
449.7	106.00	367.6	9.50
447.6	104.91	363.4	8.70
445.6	103.71	355.1	8.70
443.6	103.20	346.5	8.20
441.6	99.70		
439.6	104.69		
437.5	97.90		
435.5	103.99		
433.5	100.21		
431.5	100.51		
429.4	98.20		
427.4	101.79		
425.4	100.69		

423.4	98.61
421.4	97.10
419.3	98.40
417.3	93.69
415.3	93.20
413.3	94.30
411.3	99.79
409.3	94.60
407.2	100.21
405.2	102.31
403.2	100.60
401.2	101.11
399.2	98.40
397.2	96.61
395.1	89.91
393.1	91.20
391.1	88.10
389.1	91.10
387.1	84.39
385.1	86.20
383.0	79.40
381.0	83.20
379.0	79.80
377.0	79.71
375.0	77.30
373.0	78.90
371.0	76.30
369.0	78.60
366.9	75.41
364.9	79.51
362.9	78.70
360.9	82.51
358.9	78.60
356.9	79.89
354.9	75.41
352.9	72.09
350.9	69.10
348.9	64.00
346.8	64.70
344.8	58.20
342.8	58.60
340.8	51.50
338.8	54.20
336.8	46.40
334.8	47.10
332.8	49.80
330.8	45.80
328.8	45.40
326.8	40.00
326.0	45.80
324.8	44.70
320.7	45.60

317.8	38.80
316.7	42.60
313.6	39.80
312.7	42.10
309.4	39.80
308.7	38.20
305.2	37.30
304.7	36.60
301.0	37.40
300.7	38.00
296.7	30.00
292.5	31.00
288.3	31.00
284.1	32.20
279.9	28.20
275.7	27.00
267.4	26.10
263.2	24.80
259.0	21.20
254.8	20.70
250.6	17.50
246.4	15.30
242.2	13.60

* The rate constant at each energy given here is the average of three differently measured rate constants. Uncertainties of data are approximately 15-20 %.

Appendix 2.- The computer program for the caculation of the CO product rotational distribution from ketene. This program is written by Dr. E. R. Lovejoy.

```
program cojvse;


const
  pi        = 3.141592;
  sqrt_pi   = 1.772453;
  plancks_cst        = 3.336e-11;          {units = cm-1 s}
  prob_limit  = 1.0e-02;
  boltz_cst = 0.6950;            {cm-1 K-1}
  lmax=20;
  np0=(2*lmax+1);
  hbar=5.3089e-12;    {cm-1 s}
  num_hr_evalues=10;
  max_energy=28700;   {cm-1}


type
  thresh_Array   = Array[1..40] of Real;
  quant_Array   = Array[1..40] of integer;

var
  odd_wt,       {nuclear spin weight for the states with K-L=odd}
  even_wt,      {nuclear spin wt for the states with K-l=even}
  A_ts,         {A rotational cst for the transition state}
  B_ts,         {B rotational cst for the transition state}
  v0,           {coeff. for the (1-cos2a)/2 term in the hindered rot. pot.}
  v1,           {coeff. for the (1-cos4a)/2 term in the hindered rot. pot.}
  b_ch2,        {effective rotational cst for ch2 about the K axis}
  b_co,         {effective rotational cst for CO about the K axis}
  temp   : real;  {ketene rotational temperature}
  index1,
  Jq1,Jq2,ilk,
  num_thresholds,
  dummy,hrindx          : Integer;
  jprob_sum1,jprob_sum2,
  threshold_sum,
  pjti1,pjti2,pti,
  E_avail,
  Energy,xx1,xx2        : real;
  zpe_ts,               {energy of the zero point level of the transition
                        state relative to the zero point of grnd st. ketene}
  zpe_prods,           {energy of the ground st. products relative to the}
                      {ground state of ketene (cm-1)}
  E010,                 {energy of the triplet methylene bending motion (cm-1)}
  frac_e_rot,           {fraction of available energy which is channeled into CO rotation}
  jmaxv0_inplane,       {max. classical angular momentum imparted to the CO fragment from
                         in plane vibrations of the trans. st. in their v=0 level}
  jmax_bend,            {max. class. ang. mom. given to CO by the CCO bending vibration}
  freq_bend,            {the frequency of the CCO bending vibration at the transition state
(cm-1)}
  freq_wag             {the frequency of the CH2 wagging vibration at the transition state
(cm-1)}
            :real;
  hr_coeff              {array of the hindered rotor eigenfunctions: [K_ts,L,evalue index]
}
            : array[0..20,1..60,1..20] of real;
  hr_evalue             {array containing hindered rotor eigenvalues: [K_ts,evalue index] }
            : array[0..20,1..20] of real;
  probk                 {array containing the weights for individual K states at the
transition state
                         calculated in the procedure calc_kprob}
            : array[0..50] of real;
  kmax                  {the maximum value of K at the transition state}
            : integer;
  K_ts                  {The K quantum number at the transition state}
            : integer;
  thr_energy            {The threshold energy including vibration and rotation}
            :real;
  thresh_mtx            {Rows contain threshold energy,K_ts,vhrotor,vbend,vwag}
            :array [1..500,1..5] of real;
  amp                   {amplitude for threhold i i.e. weight of threshold i}
            :array [1..500] of real;
```

```
  kd                  {Contains experimental rate constant or phofex data used to
                       calculate the threshold weights. Column1=energy,column2=rate
                       constant or phofex signal}
            :array[1..2,1..1000] of real;
  num_kd              {number of data points in array kd}
            :integer;
  error               {flag for problems inthe interpolation routine rate_cst}
            :boolean;
  title      : string(80);
  out1,
  out2,
  inputfile1,
  inputfile2,
  inputfile3     : text;


procedure read_inputfile;
{This procedure reads the external input data file}

var
  datinfile : text;
  datfilename : string(20);
  file_opt    :string(30);
begin
writeln('enter the input data file name');
readln(datfilename);
file_opt:='NAME='+datfilename;
reset(datinfile,file_opt);
readln(datinfile,temp);
readln(datinfile,frac_e_rot,jmaxv0_inplane,jmax_bend);
readln(datinfile,a_ts,b_ts);
readln(datinfile,zpe_ts,zpe_prods);
readln(datinfile,freq_bend,freq_wag);
readln(datinfile,E010);
readln(datinfile,b_ch2,b_co);
readln(datinfile,v0,v1);
readln(datinfile,odd_wt,even_wt);
odd_wt:=odd_wt/(odd_wt+even_wt);
even_wt:=1-odd_wt;
close(datinfile);
end;


function nuclear_spin_wt(K,hr_index:integer):real;
begin
nuclear_spin_wt:=0;
 if odd(K) then
   if abs(hr_coeff[K,lmax+1,hr_index])<=1.e-6 then nuclear_spin_wt:=even_wt
      else nuclear_spin_wt := odd_wt;
 if not odd(K) then
   if abs(hr_coeff[K,lmax+1,hr_index])<=1.e-6 then nuclear_spin_wt:=odd_wt
      else nuclear_spin_wt := even_wt;
end;


procedure write_params;
var
  outfilename:string(20);
  out_opt    :string(30);
  outfile    :text;
  xx,row,column    : integer;
begin
writeln('Enter the name for the parameter output file');
readln(outfilename);
out_opt:='name='+outfilename;
rewrite(outfile,out_opt);
 writeln(outfile,title);
 writeln(outfile);
 writeln(outfile,outfilename);
 writeln(outfile,'JCO =',jq1:5,'   Ketene rotational temp =',temp:8:3,'K');
 writeln(outfile,'lmax =', lmax:5,'  jmaxv0_inplane =',jmaxv0_inplane:8:3,'   jmax_bend
=',jmax_bend:8:3);
 writeln(outfile,'triplet methylene bending frequency =',E010:8:2);
 writeln(outfile,'hindered rotor rotational csts (CH2 and CO) (cm-1) =', b_ch2:8:2,'
',b_co:8:2);
 writeln(outfile,'trans st rotational constants (cm-1) A=', A_ts:8:2,'  B=',b_ts:8:2);
 writeln(outfile,'trans st frequencies (cm-1) bend=',freq_bend:8:2,'
```

```
wag=',freq_wag:6:2);
 writeln(outfile,'zero point energy (cm-1) of the trans. st. =',zpe_ts:8:2,'   products
=',zpe_prods:8:2);
 writeln(outfile,'hindered rotor potential parameters (cm-1) v0=', v0:8:2,'
v1=',v1:8:2);
 writeln(outfile,'K-L weights:   even=', even_wt:8:4,'   odd=', odd_wt:8:4);
 writeln(outfile);
{  for xx:=0 to kmax do
begin
 writeln(outfile,xx:5,'  ',probk[xx]:8:5);
end;
writeln(outfile);
for row:= 1 to num_thresholds do
 begin
 for column:=1 to 5 do
  write(outfile,round(thresh_mtx[row,column]):10,'   ');
  writeln(outfile);
 end;     }
end;


procedure openoutfile(var outfilex:text);
var
  outname:string(20);
  out_opt    :string(30);
begin
readln(outname);
out_opt:='ddname='+outname;
rewrite(outfilex,out_opt);
writeln('enter the title for the output plot file');
readln(title);
writeln(outfilex,title);
writeln(outfilex,'energy-28000 cm-1');
writeln(outfilex,'population');
writeln(outfilex,'/1');
end;

(*****************************************************************************)


procedure diag_khindrot;

{This procedure diagonalizes the hamiltonian for the rotating hindered rotor
 system using free rotor wavefunctions for the basis set (psi0=exp(ilx)/sqrt(2*pi)).
 The problem is solved for a range of K values from 0 to kmax and the evalues
 and eigenfunctions are stored in hr_evalue and hr_coeff arrays as a function of
 K.  The matrix elements are set up so that the square of the coefficient for
 the basis function exp(ilx) is the probability of the CO fragment having angular
 momentum l (parallel with K ang. mom.) for the specific value of K and the
 particular eigenvalue...}


TYPE

   glnp0 = ARRAY [1..np0] OF real;
   glnpnp0 = ARRAY [1..np0,1..np0] OF real;

var
   hr            :glnpnp0;
   hrdd,hree     :glnp0;
   outfile       :text;
   bindex,vindex,
   ii,i,jj,
   L,num_ef,
   row,
   k_sym_top     :integer;


% include /u/lovejoy/tred20.pas
% include /u/lovejoy/tqli0.pas


function hr_mtx_element(li,lj:integer):real;
var
 element0,
 element1,
 element2    : real;
```

```
begin
element0:=0;
element1:=0;
element2:=0;
if (li=lj) then
  begin
    element0:=(B_co+B_ch2)*sqr(li-(K_sym_top*b_ch2/(b_ch2+b_co)));
    element1:=0.5;
    element2:=0.5;
  end;
if (abs(li-lj)=2) then element1:=-0.25;
if (abs(li-lj)=4) then element2:=-0.25;
hr_mtx_element:=element0 + v0*element1 + v1*element2;
end;          {of function hr_mtx_element}


procedure load_hr_mtx;
var
 row,
 column,
 lrow,
 lcolumn
          : integer;

begin          {of procedure load_hr_mtx}
row:=0;
column:=0;
 for lrow:=-lmax to lmax do
  begin
  row:=row+1;
  column:=0;
   for lcolumn:=-lmax to lmax do
    begin
    column:=column+1;
    hr[row,column]:=hr_mtx_element(lrow,lcolumn);
    end;
  end;
end;         {of procedure load_hr_mtx}


procedure sort_hr_output;
var
  smallest_index,
  index,
  start             : integer;
  smallest,
  first_evalue,
  storage           : real;

begin
start:=0;
Repeat
begin
 start:=start+1;
 smallest_index:=start;
 smallest:=hrdd[smallest_index];
 for index:=start to np0 do
  begin
   if hrdd[index]<=smallest then
    begin
     smallest_index:=index;
     smallest:=hrdd[index];
    end;
  end;
 if start=1 then first_evalue:=smallest;
 storage:=hrdd[start];
 hrdd[start]:=hrdd[smallest_index]-first_evalue;
 hrdd[smallest_index]:=storage;
 for index:=1 to np0 do
  begin
   storage:=hr[index,start];
   hr[index,start]:=hr[index,smallest_index];
   hr[index,smallest_index]:=storage;
  end;
end;
until start=np0;
end;
```

```
begin        {of procedure diag_khindrot}
  for k_sym_top:=0 to kmax do
  begin
   load_hr_mtx;
   tred20(hr,np0,hrdd,hree);
   tqli0(hrdd,hree,np0,hr);
   sort_hr_output;
   for ii:=1 to num_hr_evalues do
   begin
    hr_evalue[K_sym_top,ii]:=hrdd[ii];
   end;
   for ii:=1 to np0 do
   begin
    for jj:=1 to num_hr_evalues do
     begin
      hr_coeff[K_sym_top,ii,jj]:=hr[ii,jj];
     end;
   end;
  end;
end;

(*********************************************************************)


function rate_cst(var ey:real):real;
{Rate_cst returns the value of the data input via the
external file xxxx at energy=ey.  This data is used to calculate the
threshold amplitudes and can be either rate constant data
or Q12 phofex data.  The raw data is stored in the array kd, first
column=energy, second column is data proportional to rate constant.
The value of rate_cst is determined
by linear interpolation of the experimental data.}
var
  energy_found  : boolean;
  ii            : integer;

begin
  energy_found:=false;
  error:=false;
  ii:=0;
  repeat
   ii:=ii+1;
   if((kd[1,ii] >= ey) and (kd[1,ii+1] <= ey)) or
     ((kd[1,ii] <= ey) and (kd[1,ii+1] >= ey)) then
   energy_found:=true;
   if ii >= num_kd then
    begin
    error:=true;
    end;
  until energy_found or error;
  rate_cst:=kd[2,ii]+(ey-kd[1,ii])*(kd[2,ii+1]-kd[2,ii])/(kd[1,ii+1]-kd[1,ii]);
end;


{
procedure calc_amplitude;
var
  last,zz   : integer;
  amp_sum   : real;
begin
reset(inputfile3,'ddname=amp.dat');
num_kd:=0;
while not eof(inputfile3) do
begin
 num_kd:=num_kd+1;
 readln(inputfile3,kd[1,num_kd],kd[2,num_kd]);
 kd[1,num_kd]:=kd[1,num_kd]+28000;
end;
close(inputfile3);
amp_sum:=0;
last:=1;
for zz:=1 to num_thresholds do
begin
 if round(thresh_mtx[zz,2])=0 then
  begin
   amp[zz]:=rate_cst(thresh_mtx[zz,1])-rate_cst(thresh_mtx[last,1]);
```

```
    last:=zz;
   end
  else amp[zz]:=amp[zz-1];
  amp_sum:=amp_sum+abs(amp[zz]);
end;
amp[1]:=amp[2];
amp_sum:=amp_sum+amp[1];
for zz:=1 to num_thresholds do
 begin;
   amp[zz]:=amp[zz]*50/amp_sum;
   writeln(zz:5,'   ',amp[zz]);
 end;
end;
                    }


Function Thresh_prob(thresh_index:integer;En,thr_energy:real):real;

{This function returns the unnormalized threshold tunnelling probability}
{for the transition state threshold designated by thresh_index.}
{Each threshold has a specific amplitude (amp) and barrier imaginary}
{freq. (w). En is the total energy above the zpe of the reactant i.e.}
{the excitation laser energy. Thr_energy is the energy of the vib.}
{threshold plus the rotational energy associated with K_ts.}

var
 E_coord   : real;
 prob_sum  : real;
 exponent  : real;

begin
  E_coord:=En-thr_energy;
  exponent:=-2.0*pi*E_coord/20.;
  if exponent < 30.0 then
    thresh_prob:=1.0/(1.0+exp(exponent))
  else
    thresh_prob:=0.0;
END; {of funtion thresh_prob}



procedure calc_kprob;
var
 J,k,
 K_degen   : integer;
 pksum,
 boltz_factor,
 pk      : real;

begin;
k:=0;
pksum:=0;
repeat
  begin
  pk:=0;
  J:=k;
  repeat
    begin
    if k=0 then K_degen:=1 else K_degen:=2;
    boltz_factor:=K_degen*(2*J+1)*exp(-b_ts*J*(J+1)/boltz_cst/Temp);
    pk:=pk+boltz_factor;
    J:=J+1;
    end;
  until abs(boltz_factor/pk) < 1.e-2;
  if k=0 then kmax:=j;
  probk[k]:=pk;
  pksum:=pksum+pk;
  k:=k+1;
  end;
until k > kmax;
for k:=0 to kmax do
 begin
 probk[k]:=probk[k]/pksum;
 writeln(k,'  ',probk[k]);
 end;
writeln(kmax);
writeln;
end;
```

```
{*****************************************************************************}

function Jprob(J,threshold_index:integer; Ex:real):real;

{This function calculates the probability of producing a given J state of CO
 from a specific quantum state of the transition state of triplet ketene.
 The modified impulsive model
 is employed to predict the most probable J state of the CO fragment.  The shape
 of the J disribution is determined by the vibrational and rotational motion of
 the transition
 state by using a procedure similar to that described by Valentinti and coworkers
 and implemented by TJB and ICC .  In this program, all vibrations are in their
 zero point level except the CCO bend, the CH2 wag, and the HCCO torsion, which
 are allowed to be excited (v<=2).
 All the information about the transition state level is given by the threshold-
 index, which refers to the row of the mtx thresh_mtx.  This mtx contains the
 threshold energy and all the appropriate quantum numbers.  Ex is the energy of
 excited ketene relative to the zero point level of the ground electronic state.}

const
  BCO       = 1.93;  {CO rotational constant (cm-1)}

var

  jimp,           {classical ang. mom. imparted to the fragment perp. to the
                   molecular plane due to impulsive  energy release}
  jprob000,       {prob. of a specific j state of the CO associated with the 3CH2(000)
                   channel}
  jprob010,       {prob. of a specific j state of the CO from the 3CH2(010) channel}
  yld010          {yield of 3CH2(010)}
            :real;


function probv0(jj,jmax_v0: real) : real;
var
  sqr0:real;
begin
 sqr0:=jj*jj/jmax_v0/jmax_v0;
 probv0:=exp(-sqr0)/sqrt_pi/jmax_v0;
end;

function probv1(kk,jmax_v1: real) : real;
var
  sqr1:real;
begin
 sqr1:=kk*kk/jmax_v1/jmax_v1;
 probv1:=2.0*sqr1*exp(-sqr1)/sqrt_pi/jmax_v1;
end;

function probv2(ll,jmax_v2: real) : real;
var
  sqr2:real;
begin
 sqr2:=ll*ll/jmax_v2/jmax_v2;
 probv2:=(2.0*sqr2-1.0)*(2.0*sqr2-1.0)*exp(-sqr2)/2.0/sqrt_pi/jmax_v2;
end;


function probvx(jx,jmaxvxx: real; vxx: integer): real;
begin
if vxx=0 then probvx:=probv0(jx,jmaxvxx);
if vxx=1 then probvx:=probv1(jx,jmaxvxx);
if vxx=2 then probvx:=probv2(jx,jmaxvxx);
end;


function probv0vx(jjj,jmaxv0,jmaxvx:real;vx:integer):real;

{This function integrates the product of two angular momentum distribution
 functions.  The independent variables (jx and kx) of the functions
 are related by jjj = jx + kx.  One function is a gaussian centered at jx=0
 with a width determined by jmaxv0.  This function represents the angular
 momentum of the CO fragment due to the vibrational modes which are in the
 v=0 level.  The other function is the angular mom. distribution function
 for a mode with v=vx.  Both distribution functions are derived from
```

```
 harmonic oscillator wave functions in momentum space.
 Probv0vx convolutes the two distributions to find
 the probability of a resultant rotational angular momentum jjj. The convol-
 ution involves numerical integration of the product of the distribution
 functions over all of jx space with the restriction that kx=jjj-jx.
 Simpson's rule is used to perform the numerical integration.  This function
 is used to find the angular momentum probability distribution function
 for the component of angular momentum perpendicular to the plane containing
 the CCO portion of the ketene molecule.}

const
  limit=1.0e-07;
  stepfactor=10.0;

var
  ii    : integer;
  j1,k1,
  j2,k2,
  j3,k3    : real;
  sum,
  f1,f2,
  f3,step     : real;

begin
if jmaxv0<jmaxvx then step:=jmaxv0/stepfactor
else step:=jmaxvx/stepfactor;

if vx=0 then
begin
sum:=0.0;
j1:=0.0;
k1:=jjj-j1;
f1:=probv0(j1,jmaxv0)*probv0(k1,jmaxvx);
Repeat      {integrate from jx=0 to large positive jx}
 begin
  j2:=j1+step;
  j3:=j2+step;
  k2:=jjj-j2;
  k3:=jjj-j3;
  f2:=probv0(j2,jmaxv0)*probv0(k2,jmaxvx);
  f3:=probv0(j3,jmaxv0)*probv0(k3,jmaxvx);
  sum:=sum+f1/3.0+f2*4.0/3.0+f3/3.0;
  f1:=f3;
  j1:=j3;
 end;
Until (f2/sum < limit);
j1:=0.0;
k1:=jjj-j1;
f1:=probv0(j1,jmaxv0)*probv0(k1,jmaxvx);
Repeat      {integrate from jx=0 to large negative jx}
 begin
  j2:=j1-step;
  j3:=j2-step;
  k2:=jjj-j2;
  k3:=jjj-j3;
  f2:=probv0(j2,jmaxv0)*probv0(k2,jmaxvx);
  f3:=probv0(j3,jmaxv0)*probv0(k3,jmaxvx);
  sum:=sum+f1/3.0+f2*4.0/3.0+f3/3.0;
  f1:=f3;
  j1:=j3;
 end;
Until (f2/sum < limit);
end;

if vx=1 then
begin
sum:=0.0;
j1:=0.0;
k1:=jjj-j1;
f1:=probv0(j1,jmaxv0)*probv1(k1,jmaxvx);
Repeat
 begin
  j2:=j1+step;
  j3:=j2+step;
  k2:=jjj-j2;
  k3:=jjj-j3;
  f2:=probv0(j2,jmaxv0)*probv1(k2,jmaxvx);
  f3:=probv0(j3,jmaxv0)*probv1(k3,jmaxvx);
```

```
  sum:=sum+f1/3.0+f2*4.0/3.0+f3/3.0;
  f1:=f3;
  j1:=j3;
 end;
Until (f2/sum < limit);
j1:=0.0;
k1:=jjj-j1;
f1:=probv0(j1,jmaxv0)*probv1(k1,jmaxvx);
Repeat
 begin
  j2:=j1-step;
  j3:=j2-step;
  k2:=jjj-j2;
  k3:=jjj-j3;
  f2:=probv0(j2,jmaxv0)*probv1(k2,jmaxvx);
  f3:=probv0(j3,jmaxv0)*probv1(k3,jmaxvx);
  sum:=sum+f1/3.0+f2*4.0/3.0+f3/3.0;
  f1:=f3;
  j1:=j3;
 end;
Until (f2/sum < limit);
end;

if vx=2 then
begin
sum:=0.0;
j1:=0.0;
k1:=jjj-j1;
f1:=probv0(j1,jmaxv0)*probv2(k1,jmaxvx);
Repeat
 begin
  j2:=j1+step;
  j3:=j2+step;
  k2:=jjj-j2;
  k3:=jjj-j3;
  f2:=probv0(j2,jmaxv0)*probv2(k2,jmaxvx);
  f3:=probv0(j3,jmaxv0)*probv2(k3,jmaxvx);
  sum:=sum+f1/3.0+f2*4.0/3.0+f3/3.0;
  f1:=f3;
  j1:=j3;
 end;
Until (f2/sum < limit);
j1:=0.0;
k1:=jjj-j1;
f1:=probv0(j1,jmaxv0)*probv2(k1,jmaxvx);
Repeat
 begin
  j2:=j1-step;
  j3:=j2-step;
  k2:=jjj-j2;
  k3:=jjj-j3;
  f2:=probv0(j2,jmaxv0)*probv2(k2,jmaxvx);
  f3:=probv0(j3,jmaxv0)*probv2(k3,jmaxvx);
  sum:=sum+f1/3.0+f2*4.0/3.0+f3/3.0;
  f1:=f3;
  j1:=j3;
 end;
Until (f2/sum < limit);
end;
probv0vx:=sum*step;
end;


function prob_jp(jp:real):real;

{This function calculates the probability of a specific value
 of angular momentum perpendicular to the molecular plane.  The
 function probv0vx is called with the input angular momentum offset
 by the impulsive momentum.}
var
  jperp1    : real;

begin
jperp1:=jp-jimp;
prob_jp:=probv0vx(jperp1,jmaxv0_inplane,jmax_bend,round(thresh_mtx[threshold_index,4]));
{ prob_jp:=probv0vx(jperp1,jmaxv0_inplane,jmax_bend,0); }
end;
```

```
function probjj(jj:real):real;

{This function calculates the net classical angular momentum probability
 distribution by convoluting the distribution functions for the angular
 momenta parallel and perpendicular to the CCO plane.  The convolution
 involves a sum over the product of the individual distributions with
 the restriction that jj=sqrt(jperp**2+jpar**2) where jj is the net
 classical angular momentum of the CO fragment.  The angular momentum in the
 plane (jpar) is determined by the hindered rotor quantum state and the
 value of the rotational quantum number K (K_ts).  The
 jpar probability distribution is given by a sum of delta functions centered
 on the L values which are from the zero order wave functions used to diagonalize
 the hindered rotor problem (psi0 = exp(i*L*theta).  The coefficients in the
 delta function sum are simply the sqrs of the hr wave function coefficients. The
 hindered rotor eigenvalues and eigenfunctions are passed to the program from
 an external file (hr.dat) generated in the program hindrot.pas.}

var
 jjsum,
 jperp,
 jpar        : real;
 jhr_index,
 vx_index,
 jhr         : integer;

begin
probjj:=0;
jjsum:=0;
vx_index:=round(thresh_mtx[threshold_index,3])+1;
for jhr:= -lmax to lmax do
 begin
   jpar:=jhr;
   if sqr(jj) >= sqr(jpar) then
   begin
    jhr_index:=jhr+lmax+1;
    jperp:=sqrt(sqr(jj)-sqr(jpar));
    if abs(hr_coeff[round(thresh_mtx[threshold_index,2]),jhr_index,vx_index]) > 1.0e-06
then

jjsum:=jjsum+(sqr(hr_coeff[round(thresh_mtx[threshold_index,2]),jhr_index,vx_index]))
          *(prob_jp(jperp)+prob_jp(-jperp))/jperp;
   end;
 end;
probjj:=jjsum*jj;
end;


Function Probquant(j_quantum: real):real;

{This function integrates the classical prob. function (Jprob) from
 j_start to j_end
 to determine the probability of a rotational state with quantum number
 j_quantum. n_steps is the number of points/2 evaluated in the
 numerical integration. Simpson's rule is used to carry out the numerical
 integration.}

const
  n_steps   = 3;     {# of steps/2 used in the final numerical integration
                      of the classical ang. mom. distribution function}
var
   j_start,
   j_end,
   step_size,
   integral,
   jj1,jj2,jj3,
   prob1,prob2,prob3          : real;
   ilk : integer;

begin
j_start:=sqrt(j_quantum*(j_quantum+1.0));
j_end:=sqrt((j_quantum+1.0)*(j_quantum+2.0));
step_size:=(j_end-j_start)/n_steps/2.0;
integral:=0;
jj1:=j_start;
prob1:=probjj(jj1);
for ilk:=1 to n_steps do
```

```
begin
 jj2:=jj1+step_size;
 jj3:=jj2+step_size;
 prob2:=probjj(jj2);
 prob3:=probjj(jj3);
 integral:=integral+prob1/3.0+prob2*4.0/3.0+prob3/3.0;
 jj1:=jj3;
 prob1:=prob3;
end;
probquant:=integral*step_size;
end;


begin      {of function Jprob}

E_avail:=(Ex-thresh_mtx[threshold_index,1])+(zpe_ts-zpe_prods);
jimp:=sqrt(E_avail*frac_e_rot/BCO);
jprob000:=probquant(J);
jimp:=sqrt((E_avail-E010)*frac_e_rot/BCO);
jprob010:=probquant(J);
yld010:=ex/6000.0 - 279/60;   {0.1*(1-exp((zpe_prods+E010-ex)/350));}
jprob:=(1.0-yld010)*jprob000+yld010*jprob010;
end;       {of function Jprob}

{*****************************************************************************}


procedure sort_eigensts;
{This procedure calculates the energies for the transition state
 eigen states - including K energy.  The eigenstates are then sorted
 in order of increasing energy.}
var
 k_index,
 smallest_index,
 index,
 start,
 thresh_count,
 column          : integer;
 smallest,
 thr_en,
 storage,
 sqrcoeff_sum      : real;
 row,
 inx1,inx2,
 num_coeffs,
 last_index
                 : integer;

 begin                              {this section assigns each threshold its
                                     quantum numbers...the threshold data is
                                     stored in the array thresh_mtx; each row
                                     contains info for a particular threshold:
                                           column          info
                                             1            energy
                                             2              K
                                             3            vhrotor
                                             4             vbend
                                             5             vwag
                                                                          }
 thresh_count:=0;
 for inx1:=1 to num_hr_evalues do
 begin
   for K_index:=0 to kmax do
   begin
    thr_en:=hr_evalue[K_index,inx1]+zpe_ts+(A_ts-B_ts)*sqr(K_index);
    if thr_en <= max_energy then
    begin
     thresh_count:=thresh_count+1;
     thresh_mtx[thresh_count,1]:=thr_en;
     thresh_mtx[thresh_count,2]:=K_index;
     thresh_mtx[thresh_count,3]:=inx1-1;
     thresh_mtx[thresh_count,4]:=0;
     thresh_mtx[thresh_count,5]:=0;
    end;
    thr_en:=hr_evalue[K_index,inx1]+freq_bend+zpe_ts+(A_ts-B_ts)*sqr(K_index);
    if thr_en <= max_energy then
    begin
```

```
    thresh_count:=thresh_count+1;
    thresh_mtx[thresh_count,1]:=thr_en;
    thresh_mtx[thresh_count,2]:=K_index;
    thresh_mtx[thresh_count,3]:=inx1-1;
    thresh_mtx[thresh_count,4]:=1;
    thresh_mtx[thresh_count,5]:=0;
   end;
   thr_en:=hr_evalue[K_index,inx1]+freq_wag+zpe_ts+(A_ts-B_ts)*sqr(K_index);
   if thr_en <= max_energy then
   begin
    thresh_count:=thresh_count+1;
    thresh_mtx[thresh_count,1]:=thr_en;
    thresh_mtx[thresh_count,2]:=K_index;
    thresh_mtx[thresh_count,3]:=inx1-1;
    thresh_mtx[thresh_count,4]:=0;
    thresh_mtx[thresh_count,5]:=1;
   end;
  end;
num_thresholds:=thresh_count;
end;

start:=0;                    {this section sorts the hr/K/bend/wag states in order of
                              increasing energy}
last_index:=thresh_count;
Repeat
begin
 start:=start+1;
 smallest_index:=start;
 smallest:=thresh_mtx[smallest_index,1];
 for index:=start to last_index do
  begin
   if thresh_mtx[index,1]<=smallest then
    begin
     smallest_index:=index;
     smallest:=thresh_mtx[index,1];
    end;
  end;
 for column:=1 to 5 do
 begin
  storage:=thresh_mtx[start,column];
  thresh_mtx[start,column]:=thresh_mtx[smallest_index,column];
  thresh_mtx[smallest_index,column]:=storage;
 end;
end;
until start=last_index;
end;

procedure write_variables;
var
 row,column    : integer;
begin
for row:= 1 to num_thresholds do
 begin
 for column:=1 to 5 do
  write(out1,round(thresh_mtx[row,column]):10,'    ');
 writeln(out1,amp[row]:8);
 end;
end;


procedure openoutfile1(var outfile:text);
var
  outfilename:string(20);
  out_opt     :string(30);
  title       :string(80);
begin
readln(outfilename);
out_opt:='ddname='+outfilename;
rewrite(outfile,out_opt);
writeln('enter the title for the output plot file');
readln(title);
writeln(outfile,title);
writeln(outfile,'energy-28000 cm-1');
writeln(outfile,'population');
writeln(outfile,'/L');
end;
```

```
begin                    {of program cojvse}
read_inputfile;
calc_kprob;
diag_khindrot;
sort_eigensts;
writeln('enter the J value');
readln(jq1);
writeln('Enter the name of the P(J) data file');
openoutfile(out2);
energy:=zpe_ts-50.0;
write_params;

for index1:=1 to 100 do
begin
threshold_sum:=0.0;
for ilk:=1 to num_thresholds do
  begin
   thr_energy:=thresh_mtx[ilk,1];
   K_ts:=round(thresh_mtx[ilk,2]);
   hrindx:=round(thresh_mtx[ilk,3])+1;
   threshold_sum:=threshold_sum+thresh_prob(ilk,energy,thr_energy)
                  *probk[K_ts]*nuclear_spin_wt(K_ts,hrindx);
  end;
Jprob_sum1:=0.0;
 for ilk:=1 to num_thresholds do
 begin
   if threshold_sum > 0 then
   begin
    thr_energy:=thresh_mtx[ilk,1];
    K_ts:=round(thresh_mtx[ilk,2]);
    hrindx:=round(thresh_mtx[ilk,3])+1;
    pti:=thresh_prob(ilk,energy,thr_energy)*probk[K_ts]*nuclear_spin_wt(K_ts,hrindx)
         /threshold_sum;
    if pti > prob_limit then
     begin
      pjti1:=Jprob(Jq1,ilk,energy);
      jprob_sum1:=jprob_sum1+pti*pjti1;
     end;
   end;
 end;
if jprob_sum1 > 0.0 then
begin
 writeln(energy,'    ',jprob_sum1);
 xx1:=energy-28000.0;
 writeln(out2,xx1,'    ',jprob_sum1);
end;
energy:=energy+5.0;
end;
close(out1);
close(out2);
end.                          {of program cojvse}
```

Appendix 3. The computer program for RRKM calculation for CH_2CO dissociation for the case of K-mixed. For the application to CD_2CO rate constants, the RRKM parameters should be changed in a proper way.

```
Program RRKM;
{RRKM calculation for the triplet ketene dissociation using ab initio}
{calculated values from Shaffer's paper.  you can vary imaginary frequency}
{to fit the rate measurement data.  }


{$I c:\turbo\paslib\outfile.pro}

Type
   QuantumVector_ts = array[1..8] of integer;


VAR

 t,alpha,eph,ratio:real;
 j,i,ju,jco:integer;{ju is J' of the excited state of ketene}
 p1,p2: real;
 pop: array[0..60,0..1] of real;
 hpop:array[0..30,0..30,0..1] of real;
 hpoph:array[0..30,0..30,0..1] of real;
 total:real;
 infile,outfile:text;
 x1:real;
 i1:integer;
 Etunn:real;{tunneling Energy which is E-V0-Evib-Erot}
 hsum:real;
 hsumh:real;
 V0,V1:real;{eckart ptl shape}
 A_ts,B_ts,C_ts:real;
 wb:real;{imaginary frequency}
 Wts:array[1..8] of real;
 HSrot:array[0..40] of real;
 hsrot1,hsrot2,hsrot3,hsrot4,hsrot5:array[0..15] of real;
 ohsrot, ohsrot1,ohsrot2,ohsrot3,ohsrot4:array[0..15] of real;
 Total_density:real;
 density_factor:real;{multiplication to wr}
 ku:integer;{K quantum number of the upper state}
 Total_prob:real;
 Q_C:quantumvector_ts;
 threshold_factor:real;
 Ebarr:real;
 ZPE_ts:real;{zero point energy of transition state}
 Prob_sum_p,prob_sum_h,density_sum_p, density_sum_h:real;
 E_rotational:real;
 ns:integer;
 jg:integer;
 k:integer;
 Ed:real;
 rate_p:array[0..30,0..30,0..1] of real;

 average_rate:real;
 E:real;
 h:real;
 E_start:real;
 E_increment:real;
 E_final:real;
 perp,hori:real;

procedure thermal;{initial distribution of ketene at temperature}

VAR
 Ins,          {nuclear spin Ins=0 para, Ins=1 ortho}
 J,            {J quantum number of sym. top Ketene }
 Ka:integer;  {only consider Ka=0,1 this is good approximation for T<10K }
 B,A :real;
               {Rotation constant for sym. top appr. Ketene}
 {POP: array[0..60,0..1] of real;}
```

```
              {relative population of initial quantum states of ketene}
Erot :real;  {rotational energy of ketene}
sump1,sump2 :real;  {sum for populaton}

begin

  B:=0.3370525;
  A:=9.37;

  sump1:=0.;
  sump2:=0.;
  ratio:=0.;

  for Ka:=0 to 1 do
  begin;
  for j:=0 to 30 do
  begin;
  pop[j,Ka]:=0.000000000;
  end;
  end;


    For Ka:=0 to 1 do
    begin;
      For j:=0 to 30 do {jmax for ketene is set at 30 at this line}
        begin;
          if (ka =1) and (j=0) then j:=j+1;
          Erot:=B*J*(J+1)+(A-B)*Ka*Ka;
          pop[j,Ka]:=(2*J+1)*exp(-Erot/(0.6954*t));
          if Ka=0 then sump1:=sump1+pop[J,0];
          if Ka=1 then sump2:=sump2+pop[J,1];
        end;{of J }
    end;{of Ka}

       sump1:=sump1+sump2;
    for J:=0 to 30 do
    begin;
    pop[j,0]:=pop[j,0]/sump1;
    pop[j,1]:=pop[j,1]/sump1;
    end;

end;{of procedure thermal}

function Eckart(ec:real) :real;

Var
  a,b,c:real;
 dummy,pn,pd:real;

   begin

{  dummy:=1/( (1/sqrt(v0)) + (1/sqrt(v1)) );
   a:=((4*pi)/wb)*dummy*sqrt(ec+v0);
   if (ec+v1) <0 then b:=0.00
   else
   b:=((4*pi)/wb)*dummy*sqrt(ec+v1);
   c:=2*pi*sqrt( (v0*v1)/(wb*wb)  - (1/16) );
   pn:=exp(a+b) - exp(a-b)-exp(b-a)+exp(-a-b);
   pd:=exp(a+b) + exp(-a-b)+exp(2*c)+exp(-2*c);
   Eckart:=(pn/pd);}

   if wb <> 0 then begin
   pn:=(2*pi*ec)/wb;
   if pn>1.E+002 then pd:=0;
   if pn<-1.E+002 then pd:=1.E+100 ;
   if (pn<1.E+002) and (pn>-1.E+002) then pd:=exp(-pn);
   Eckart:=1/(1+pd); {Parabolic barrier}
   end;
   end;

function direct(ecc:real) :real;

   begin
   if ecc<0 then direct:=0.000
   else
   direct:=1.000;
   end;
```

```
Function tunnel_prob(E:real; J,K:integer; Q_C:quantumvector_ts):real;

var
i:integer;
rot_E,vib_E,Tunnel_E:real;

begin

Rot_E:=0.5*(b_TS+c_ts)*(j*(j+1)-K*K) + a_ts*K*K;
Vib_E:=0.000;
for i:=2 to 8 do
begin
 Vib_E:=vib_E+wts[i]*(Q_C[i]+0.5);
 end;
 if (abs(K)=0) and (ns=0) then
       vib_E:=vib_E+hsrot[Q_C[1]]+77.0;
 if (abs(K)=1) and (ns=0) then
       vib_E:=vib_E+hsrot1[Q_C[1]]+77.0;
 if (abs(K)=2) and (ns=0) then
       vib_E:=vib_E+hsrot2[Q_C[1]]+77.0;
 if (abs(K)=3) and (ns=0) then
       vib_E:=vib_E+hsrot3[Q_C[1]]+77.0;
 if (abs(K)=4) and (ns=0) then
       vib_E:=vib_E+hsrot4[Q_C[1]]+77.0;
 if (abs(K)>3) and (ns=0) then
       vib_E:=vib_E+hsrot3[Q_C[1]]+77.0;
 if (abs(K)=0) and (ns=1)  then
       vib_E:=vib_E+ohsrot[Q_C[1]]+77.0;
 if (abs(K)=1) and (ns=1)  then
       vib_E:=vib_E+ohsrot1[Q_C[1]]+77.0;
 if (abs(K)=2) and (ns=1)  then
       vib_E:=vib_E+ohsrot2[Q_C[1]]+77.0;
 if (abs(K)=3) and (ns=1)  then
       vib_E:=vib_E+ohsrot3[Q_C[1]]+77.0;
 if (abs(K)=4) and (ns=1)  then
       vib_E:=vib_E+ohsrot4[Q_C[1]]+77.0;
 if (abs(K)>3) and (ns=1)  then
       vib_E:=vib_E+ohsrot3[Q_C[1]]+77.0;

Tunnel_E:=E-V0-ROt_E-Vib_E;
if wb = 0 then tunnel_prob:=direct(Tunnel_E);
if wb <> 0 then tunnel_prob:=Eckart(Tunnel_E);
end;

Procedure Explicit_Summation;{Will Polik's Algorithm}

label

   Main_loop,No_more;

var
   i:integer;
   probability:real;
   threshold:real;

begin

for i := 1 to 8 do       {initialize vibration quantum counter}
  Q_C[i] := 0;
Total_Prob := 0;                          {initialize summed probability}
Threshold := Threshold_Factor * Tunnel_Prob(E,J,K,Q_C);
if wb =0 then threshold:=1.0;
Main_Loop:;                          {main loop through all possible vib states}
Probability := Tunnel_Prob(E,J,K,Q_C); {calculate tunnelling Prob}

if Probability < Threshold               {is it less than the threshold?}
then
  begin                                  {yes...}
  i := 1;                                {start with first normal mode}
    repeat
    Q_C[i] := 0;             {increment Quantum_Counter - part 1}
    if i < 8
    then Q_C[i+1] := Q_C[i+1] + 1         { - part 2}
    else goto No_More;                   {no more vib states; exit main loop}
    i := i+1;                            {move to next normal mode}
    Probability := Tunnel_Prob(E,j,k,Q_C);  {Re-calculate}
    until Probability >= Threshold; {repeat if Probability is still too small}
  end;
```

```
Total_Prob := Total_Prob + Probability;  {bin the now valid vib energy}
Q_C[1] := Q_C[1] + 1;   {increment first normal mode}
goto Main_Loop;                          {end of main loop}
No_More:;                                {label for exit from main loop}
end; {of procedure Explicit_Summation}


function SDensity(Ee:real):real;{density of states using exp. value for ketene S0}
   begin
   Sdensity:=(exp(8*ln(Ee+6712.5)))/(40320.*4.3096E+27);
   end;

function Tdensity(Ef:real):real;{density of states using ab initio values for T1}
   begin
   tdensity:=(exp(8*ln(Ef+6457.5)))/(40320.*2.8924E+27);
   end;

begin {main}

A_ts:=3.35;
B_ts:=0.268;
C_ts:=0.242;

h:=3.33565E-11;

wts[2]:=240;
wts[3]:=326.0;
wts[4]:=472.0;
wts[5]:=1183.0;
wts[6]:=2029.0;
wts[7]:=2997.0;
wts[8]:=3178.0;

Hsrot[0]:=0.00;     {V0=330,V1=-20, K=0}
ohsrot[0]:=0.00;
ohsrot[1]:=104;
hsrot[1]:=105;
hsrot[2]:=196;
ohsrot[2]:=206;
ohsrot[3]:=263;
hsrot[3]:=305;
hsrot[4]:=325;
ohsrot[4]:=415;
ohsrot[5]:=418;
hsrot[5]:=546;
hsrot[6]:=546;

oHsrot1[0]:=0.00;     {K=1}
hsrot1[0]:=0.30;
hsrot1[1]:=105;
ohsrot1[1]:=106;
ohsrot1[2]:=197;
hsrot1[2]:=204;
hsrot1[3]:=267;
ohsrot1[3]:=292;
ohsrot1[4]:=341;
hsrot1[4]:=387;
hsrot1[5]:=448;
ohsrot1[5]:=509;
ohsrot1[6]:=584;

Hsrot2[0]:=0.00;     {K=2}
ohsrot2[0]:=0.00;
ohsrot2[1]:=105;
hsrot2[1]:=105;
hsrot2[2]:=200;
ohsrot2[2]:=200;
ohsrot2[3]:=276;
hsrot2[3]:=280;
hsrot2[4]:=360;
ohsrot2[4]:=366;
ohsrot2[5]:=474;
hsrot2[5]:=482;
hsrot2[6]:=616;

oHsrot3[0]:=0.00;     {K=3}
hsrot3[0]:=0.10;
hsrot3[1]:=105;
```

```
ohsrot3[1]:=106;
ohsrot3[2]:=197;
hsrot3[2]:=205;
hsrot3[3]:=265;
ohsrot3[3]:=296;
ohsrot3[4]:=336;
hsrot3[4]:=393;
hsrot3[5]:=441;
ohsrot3[5]:=517;
ohsrot3[6]:=576;

Hsrot4[0]:=0.00;     {K=4}
ohsrot4[0]:=0.10;
ohsrot4[1]:=99;
hsrot4[1]:=102;
hsrot4[2]:=175;
ohsrot4[2]:=192;
ohsrot4[3]:=227;
hsrot4[3]:=281;
hsrot4[4]:=295;
ohsrot4[4]:=385;
ohsrot4[5]:=399;
hsrot4[5]:=514;
hsrot4[6]:=514;

zpe_ts:=0.000;

for i:=2 to 8 do
zpe_ts:=zpe_ts+wts[i]*0.5;
zpe_ts:=zpe_ts+77.0;{77 is half of 154 cm-1 which is a torsional motion}

writeln('input imaginary frequency(W_tsi)');
readln(wb);

writeln('Temperature(K) ?');
readln(t);
writeln('input Enery Barrier you wish in cm-1 ');
writeln('this barrier energy is above the threshold which is 26969.0(5) cm-1');
writeln('therefore thousand 28 *** plus 31 cm-1');
readln(Ebarr);
writeln('input the lower limit of the calculation (0.01 - 0.0001)');
readln(threshold_factor);
writeln('input starting energy, increment, final energy eg 28000 10 28100');

readln(E_start, E_increment, E_final);
writeln('input the scale factor for ρ(E)');
readln(density_factor);
perp:=1;
writeln('name the outfile for the rate vs. photolysis energy - 28000 cm-1');

openoutfile(outfile);
writeln(outfile,'Ebarrier=',Ebarr:5:1,' ','imaginary frequency=',wb:5:2);
writeln(outfile,'Photolysis Energy - 28000 cm-1');
writeln(outfile,'thermal averaged rate constant');
writeln(outfile,'/l');

v0:=Ebarr+26969.0-ZPE_TS;
v1:=Ebarr;

thermal;

for ju:=0 to 30 do
begin;
for j:=0 to 30 do
begin;
HPOP[Ju,j,0]:=0.000000;
HPOP[Ju,j,1]:=0.000000;
end;
end;
hsum:=0.000;
hsumh:=0.000;
{ In this program, Honl London factors for only perpendicular transitions}
{ are used.}
for j:=0 to 30 do
begin
 if pop[j,0] >1.E-002 then begin
   if j=0 then begin
       Hpop[1,j,0]:=4*pop[j,0];
```

```
        hpoph[1,j,0]:=pop[j,0];
        hpoph[0,j,0]:=0.0;
        Hpop[0,j,0]:=pop[j,0];
        end;
    if j <> 0 then begin
        Hpop[j+1,j,0]:=pop[j,0]*2*((j+2)/(2*j+1));
        Hpop[j  ,j,0]:=pop[j,0]*1;
        Hpop[j-1,j,0]:=pop[j,0]*((j-1)/(2*j+1));
        Hpoph[j+1,j,0]:=pop[j,0]*(j+1)/(2*j+1);
        hpoph[j,j,0]:=0.0;
        hpoph[j-1,j,0]:=pop[j,0]*j/(2*j+1);
        end;
 end;
end;

for j:=0 to 30 do
begin
 if pop[j,1] > 1.E-002 then begin
    Hpop[j+1,j,1]:=pop[j,1]*((j+3)*(J+2)+(j+1)*j)/((j+1)*(2*j+1));
    Hpop[j,j,1]  :=pop[j,1]*(j*(j+1)+(j+2)*(j-1))/(j*(j+1));
    Hpop[j-1,j,1]:=pop[j,1]*((j-2)*(j-1)+(j+1)*j)/(j*(2*j+1));
    hpoph[j+1,j,1]:=pop[j,1]*j*(j+2)/((j+1)*(2*j+1));
    hpoph[j,j,1]:=pop[j,1]/(j*(j+1));
    hpoph[j-1,j,1]:=pop[j,1]*(J*J-1)/((2*j+1)*j);
 end;
 end;

 for ju:=0 to 30 do
 begin
 for j:=0 to 30 do
 begin
 hsum:=hsum+hpop[ju,j,0];{+hpoph[ju,j,0];}
 hsumh:=hsumh+hpop[ju,j,1];{+hpoph[ju,j,1];}
 end;
 end;

for ju:=0 to 30 do
begin
for j:=0 to 30 do
begin
hpop[ju,j,0]:=(1/4)*hpop[ju,j,0]/hsum; {Here, the nuclear spin is not }
hpop[ju,j,1]:=(3/4)*hpop[ju,j,1]/hsumh; {cooled down}

rate_p[ju,j,0]:=0.000;
rate_p[ju,j,1]:=0.000;
end;
end;

 average_rate:=0.000;

 Eph:=E_start;

REPEAT
 average_rate:=0.000;

for ns:=0 to 1 do
begin
for jg:=0 to 30 do
begin
E:=Eph+0.3370525*jg*(jg+1)+9.0329*ns*ns;

for j:=0 to 30 do
begin
   prob_sum_p:=0.000;
   density_sum_p:=0.000;
   if (hpop[j,jg,ns] <> 0) then
     begin
       for k:=-j-1 to j+1   do  {J=N+S should be conserved; K-mixed}
         begin
         Explicit_Summation;
         prob_sum_p:=Prob_sum_p+total_prob;
         Ed:= E-0.33705*j*(J+1)-9.0329*K*K; {true only when j=0}
         density_sum_p:=density_sum_p+ sdensity(Ed);
       end;{of K summation}
     if density_sum_p <> 0 then begin
     rate_p[j,jg,ns]:=prob_sum_p/(h*density_sum_p*density_factor);
     end;
     average_rate:=average_rate+rate_p[j,jg,ns]*3*
```

```
    hpop[j,jg,ns];   {electron spin degeneracy is multiplied here.}

   end;{of if}
 end;{of j summation}
 end;{of Jground summation}
 end;{of nuclear spin}

writeln('Eph=',Eph:8:2,' ','rate/1e5=',(average_rate/1.E+005):10:5);
writeln(outfile,(Eph-28000.00):8:2,' ',(average_rate/1.E+005):10:5);
Eph:=Eph+E_increment;
UNTIL Eph>E_final;

close(outfile);
end. {of RRKM calculation program}
```

DATE FILMED

10 / 7 / 93

END